

Diss. ETH Nr. 13875

**SPIN FLUCTUATIONS
IN SELECTED
MAGNETICALLY ORDERED SYSTEMS**

Submitted to the
Swiss Federal Institute of Technology (ETH)
for the degree of
Doctor of Natural Sciences

presented by

Fabrizio Semadeni
Dipl. Ing. Phys. EPFL
born October 24, 1972
from St-Maurice
Canton du Valais

accepted on the recommendation of

Prof. Dr. A. Furrer, examiner
Prof. Dr. G. Kostorz, co-examiner
Prof. Dr. P. Böni, co-examiner

2000

Contents

Table of Contents	iii
Abstract	vi
Résumé	viii
1 Introduction	1
2 Neutron Scattering	5
2.1 Introduction	5
2.2 Neutron-matter interaction	5
2.2.1 Nuclear scattering	6
2.2.2 Magnetic scattering	8
2.2.3 Generalised susceptibility	9
2.3 Instrumentation	10
2.3.1 Three-axis spectrometer	10
2.3.2 Small angle neutron scattering	11
3 Muon Spin Rotation Spectroscopy	13
3.1 Introduction	13
3.2 μ SR technique	13
3.3 Zero field μ SR	15
3.4 Transverse field μ SR	15
3.5 Instrumentation	16
4 Theory of the spin dynamics in magnetically ordered systems	17
4.1 Introduction	17
4.2 Static properties	18
4.3 Dynamic Properties	21
4.3.1 Scaling theory	21
4.3.2 Dipolar interactions	22
4.3.3 Spin dynamics	24
4.4 Theory of itinerant magnetism	25
4.4.1 Stoner theory	25
4.4.2 Mean field RPA	26

4.4.3	SCR-RPA	27
5	Itinerant Spin Systems	30
5.1	Ni ₃ Al	30
5.1.1	Introduction	30
5.1.2	Experimental procedure	31
5.1.3	Experimental results	32
5.1.4	Discussion	36
5.1.5	Intermediate conclusion	39
5.2	Ni	41
5.2.1	Introduction	41
5.2.2	Magnetic scattering with SANS	41
5.2.3	Experiment and data analysis	43
5.2.4	Intermediate conclusion	46
6	Localised Spin Systems	48
6.1	Paramagnetic scattering in EuS at very high temperature	48
6.1.1	Introduction	48
6.1.2	Results	50
6.1.3	Intermediate conclusion	52
6.2	The inorganic spin-Peierls compound CuGeO ₃	55
6.2.1	Introduction	55
6.2.2	Overview on pure and doped CuGeO ₃	56
6.2.3	Experimental details	60
6.2.4	Results	62
6.2.5	Discussion	70
6.2.6	Intermediate conclusion	72
7	Concluding Remarks	73
	Bibliography	75
	Acknowledgments	79
	Curriculum Vitae	80

Abstract

The work presented in this thesis is devoted to the study of magnetically ordered compounds by means of neutron and muon spectroscopy. We have selected four compounds that belong to specific classes of magnetic systems: The intermetallic compound Ni_3Al was chosen as the paradigm of the weak itinerant ferromagnets; The itinerant ferromagnet Ni was taken as a promising candidate for the study of longitudinal fluctuations in its magnetically ordered phase; For the study of the paramagnetic scattering in localised systems we have selected the cubic Heisenberg system EuS . The last compound on which we focus our attention is the low dimensional spin system $\text{CuGe}_{1-x}\text{Si}_x\text{O}_3$ which exhibits an astonishing characteristic: an antiferromagnetic ground state that is observed to coexists with a non-magnetic singlet spin state, although these two ground states are expected to be mutually exclusive.

After the introducing part, an overview of neutron scattering is presented in Chapter 2. The underlying theory and the experimental method are outlined within the framework of linear response theory. After this, Chapter 3 gives a short introduction to the muon spin rotation (μSR) technique.

Chapter 4 is focused on the theoretical description of the static and dynamical properties in magnetically ordered systems. As a first step, the basic principles of critical phenomena and scaling theory are reviewed. The second part of the Chapter presents step by step the theoretical background for localised spin systems and for itinerant systems.

In the first part of Chapter 5, we report on the study of critical fluctuations in the weak itinerant ferromagnet Ni_3Al . We have measured the magnetic excitations in the ordered phase as well as in the paramagnetic phase by means of inelastic neutron scattering. **The linewidth of the spin-waves is observed to decrease with decreasing temperature, although the theory for itinerant spin systems predicts the opposite situation.** The magnetic excitations have been interpreted within the framework **mode-mode coupling theory (MMT) for an isotropic ferromagnet.** In this model, the scaling behaviour for the spin fluctuations is expected to behave in a similar way than what was observed in Ni_3Al . In addition, the parametrisation of the linewidth for the critical scattering shows that the dynamical critical exponent $z \simeq 2.5 \pm 0.2$ is close to the value expected for an isotropic Heisenberg model, **proving that critical fluctuations are also important in**

weak-itinerant ferromagnets. Moreover, the temperature dependence of the spin waves compares well with the predictions of MMT. The correlation length in weak itinerant magnets is very large leading to pronounced short range order and to critical fluctuations far away from the ordering temperature T_C . **Our results show that it is necessary to include critical fluctuations in the theory for itinerant magnetism.**

In the second part of Chapter 5, the critical scattering of the itinerant magnet Ni is studied by means of small angle neutron scattering. The predicted $1/Q$ divergence in the longitudinal static susceptibility cannot be observed and tentative explanations are proposed. However, the effect of dipolar forces is clearly seen in the anisotropy of the scattering.

In the first part of Chapter 6 we present an investigation of the high temperature paramagnetic scattering in the localised spin compound EuS. We show that, near the zone boundary, **the linewidth of the spin fluctuations remains finite well above the ordering temperature**, as predicted by the theory based on a Heisenberg model, in strong contradiction to an ideal paramagnet where the scattering is purely incoherent and elastic. **Our results show that the correlations between neighbouring spins persist far away from the ordering temperature.**

Finally, we present a study of the static and dynamical properties of the Si-doped spin-Peierls compound CuGeO_3 . **The basic idea is to understand why two magnetic ground states that are supposed to be mutually exclusive can coexist in the doped compounds.** As a first step, the temperature-concentration phase diagram of the Si-doped compound is investigated by means of neutron scattering and μSR spectroscopy, in order to determine the microscopic distribution of the magnetic and lattice dimerised regions as a function of doping. The analysis of the zero-field muon spectra confirms the spatial inhomogeneity of the staggered magnetisation that characterises the antiferromagnetic superlattice peaks observed with neutrons. In addition, the variation of the macroscopic order parameter with doping can be understood by considering the evolution of the local magnetic moment as well as of the magnetic regions contributing to the muon signal.

As a second step, we present, for selected doped samples, the dispersion of the antiferromagnetic excitations along three symmetry directions. Two important results can be deduced from the analysis of the spin dynamics: the spin gap arising from spatial anisotropy is independent on the doping concentration; moreover the exchange interaction parameters that are extracted from the dispersion curves exhibits values that do not significantly differ from the values of the undoped compound.

The cumulative information given by neutron scattering and μSR have provided an insight on the effect of bond doping in CuGeO_3 . **The introduction of impurities destroys locally the spin-Peierls phase, where the antiferromagnetic (AF) phase sets in. Moreover, the volume fraction of both spin-Peierls and AF phases is observed to vary with doping, whereas the physical properties of the AF phase remain almost unchanged.**

Résumé

Ce travail de thèse est consacré à l'étude des matériaux magnétiques par spectroscopie de neutrons et de muons. Nous avons choisi quatre composés, chacun appartenant à une classe particulière. Le composé intermétallique Ni_3Al a été sélectionné en tant que paradigme des matériaux ferromagnétiques de type itinérant à faible magnétisation. Le Ni était présupposé comme candidat pour l'étude des fluctuations longitudinales dans un métal ferromagnétique. Le composé EuS , ferroaimant de type Heisenberg, a permis l'étude de la diffusion paramagnétique dans un système de spins localisés. Le dernier composé magnétique sur lequel nous avons retenu notre attention est le système à basse dimension $\text{CuGe}_{1-x}\text{Si}_x\text{O}_3$, dont les propriétés magnétiques sont pour le moins inhabituelles. En effet, en-dessous d'un certain seuil de dopage, une coexistence apparaît entre un état fondamental antiferromagnétique et un état singulet non magnétique, bien que ces deux états fondamentaux sont supposés s'exclure mutuellement.

Après une introduction sur le magnétisme, le Chapitre 2 propose une vue d'ensemble de la diffraction de neutrons. L'accent est mis sur les fondements de la théorie ainsi que sur la méthode expérimentale, en relation avec la physique du solide et sur la base de la théorie de réponse linéaire. La partie préliminaire de ce travail se prolonge par le Chapitre 3, qui donne une brève introduction à la spectroscopie de muons.

Le Chapitre 4 est axé sur la description théorique des propriétés statiques et dynamiques dans les matériaux magnétiques ordonnés. Dans un premier temps, les phénomènes critiques ainsi que les bases de la théorie d'échelle (scaling theory) sont succinctement présentés. La seconde partie du Chapitre 4 décrit successivement les fondements théoriques propres aux systèmes de spins localisés, puis ceux spécifiques aux systèmes de spins itinérants.

La première partie du Chapitre 5 est dédiée à l'étude des fluctuations critiques dans le composé Ni_3Al , un système de spins itinérants à faible aimantation. Nous avons mesuré les fluctuations de spin dans la phase ordonnée ainsi que dans la phase paramagnétique par diffusion inélastique de neutrons. Ces excitations ont été interprétées en parallèle, sur la base de la théorie des spins itinérants ainsi que par la théorie de "mode-mode coupling" (MMT), dans l'hypothèse d'un matériau ferromagnétique isotrope. L'analyse de la largeur de ligne des fluctuations à la température de transition fournit un exposant critique dynamique $z \simeq 2.45 \pm 0.2$ proche de la valeur prévue par le modèle isotrope de Heisenberg, montrant par-là que

les fluctuations critiques sont aussi importantes dans les systèmes de spins itinérants à faible aimantation. En outre, la dépendance en température des ondes de spin s'accorde avec les prédictions de la MMT. De plus, nous observons que la longueur de corrélation dans les composés itinérants à faible aimantation est importante. Ceci implique un ordre magnétique accentué à courte distance, ainsi que la présence de fluctuations critiques bien au-delà de la température de transition magnétique T_C . Ces résultats expérimentaux indiquent par conséquent qu'il est nécessaire d'inclure des fluctuations critiques dans la théorie du magnétisme itinérant.

Dans la seconde partie du Chapitre 5, les fluctuations critiques dans le Ni sont étudiées par diffusion de neutrons à petits angles. La divergence en $1/Q$ de la susceptibilité longitudinale prévue par la théorie n'a pu être observée, et quelques explications sont proposées. Cependant, l'effet de l'interaction dipolaire a été mis en évidence dans l'anisotropie des spectres de neutrons.

Dans la première partie du Chapitre 6 nous présentons une étude de la diffusion paramagnétique à haute température dans le composé EuS, dont les spins sont localisés sur les ions Eu^{2+} . Proche du bord de la zone de Brillouin, la largeur de ligne des fluctuations de spin reste finie bien au-delà de la température de transition, comme prévu par le modèle théorique fondé sur un système magnétique de type Heisenberg. Ce résultat est en opposition avec le cas d'un matériau paramagnétique idéal, où l'on s'attend à un signal de type purement incohérent et élastique.

Pour terminer le Chapitre sur les systèmes de spins localisés, nous présentons une étude des propriétés statiques puis dynamiques du composé spin-Peierls CuGeO_3 dopé au silicium. Dans un premier temps, les mesures complémentaires de diffraction neutronique et de spectroscopie de muons permettent de constituer le diagramme de phase température-concentration du composé dopé au silicium; le but étant de déterminer la distribution microscopique des zones magnétiques ainsi que celles des zones dimérisées en fonction du dopage.

L'analyse des spectres de muons en champ nul confirme l'inhomogénéité spatiale de la magnétisation dans la phase antiferromagnétique; celle-ci a été au préalable caractérisée via les pics antiferromagnétiques de surstructure observés par neutrons. D'autre part, la variation du paramètre d'ordre macroscopique en fonction du dopage peut s'expliquer par l'évolution du moment magnétique local ainsi que par les volumes des différentes zones qui contribuent au signal du muon. Dans un deuxième temps, nous avons sélectionné quelques échantillons dans lesquels nous avons mesuré la dispersion des excitations antiferromagnétiques, le long de trois directions de symétrie. L'analyse de la dynamique de spins dans les composés dopés fournit deux résultats majeurs: le gap de spin est indépendant de la concentration du dopage, du moins dans l'intervalle expérimental, et s'explique par l'anisotropie des intégrales d'échange entre les ions de Cu^{2+} . En outre, les paramètres d'échange qui sont extraits des courbes de dispersion présentent des valeurs comparables à celles du composé non dopé.

Chapter 1

Introduction

*The important thing in science is not so much to obtain new facts
as to discover new ways of thinking about them.*

Sir William Bragg

Magnetic materials provide an extensive variety of systems for the investigation of electronic interactions in solid state physics. The character of the interaction between the magnetic moments allows to classify magnetic systems into various groups that are mutually non exclusive. Most of the magnetic materials undergo a phase transition to an ordered phase at a finite temperature. The type of spin arrangement that takes place allows to define several classes of spin configurations like ferromagnets, antiferromagnets, ferrimagnets, incommensurate structures and spin glasses. Depending on the geometric arrangement of the magnetic moments, one can distinguish between one (e.g. KCuF_3 , Sr_2CuO_3 , Ca_2CuO_3) two (e.g. $\text{Rb}_2\text{Co}_{0.6}\text{Mg}_{0.4}\text{F}_4$, $\text{SrCr}_{9p}\text{Ga}_{12-9p}\text{O}_{19}$ ($p=0.92$), K_2CuF_4) and three dimensional (e.g. Fe, Ni, Co, etc.) spin systems. A additional distinction can be made in relation with the dimensionality of the order parameter that describes uniaxial (Ising like), easy-plane (XY-model) and isotropic (Heisenberg) magnets.

Generally, three physical parameters are necessary for the characterisation of a magnetically ordered compound: the ordering temperature T_C , the magnetic moments $p(T)$ and the spin correlation length $\xi(T)$ that depends on the temperature. p plays the role of the order parameter that is non-zero below T_C , and $\xi(T)$ is a measure of the distance over which the spins are correlated: at T_C , ξ becomes infinite. The ordering originates from long range correlations arising between electrons below T_C , when the energy of the electrostatic interactions exceeds the kinetic energy of the fluctuations.

Experimentally, the magnetic moment p of the ions is determined above T_C via the magnetic susceptibility of the bulk material that is given by the Curie-Weiss law

$$\chi(T) = (g\mu_B)^2 S(S+1) \frac{1}{3k_B} \frac{1}{(T - T_C)}. \quad (1.1)$$

One obtains an effective moment per ion $p_{eff} = \sqrt{(g\mu_B)^2 S(S+1)}$, where g is the

gyromagnetic factor, S the spin quantum number of the ion, μ_B the Bohr magneton and k_B the Boltzmann constant. Below T_C , the moment at saturation p_s is determined via the measurement of the bulk magnetisation, that is extrapolated to $T=0$.

Experiments on many materials have shown that the values obtained by both methods can differ significantly. The Rhodes-Wohlfarth plot [1] shows the ratio p_{eff}/p_s versus T_C for various ferromagnets (see Fig 1.1). On the basis of the experimental data reported in the plot, a distinction can be made between two classes of materials. The insulators, where the electrons are localised at the magnetic ions, exhibit a value of p_{eff}/p_s that is close to one. In contrast, the metals where the electrons are delocalised display a ratio that can be much larger than unity.

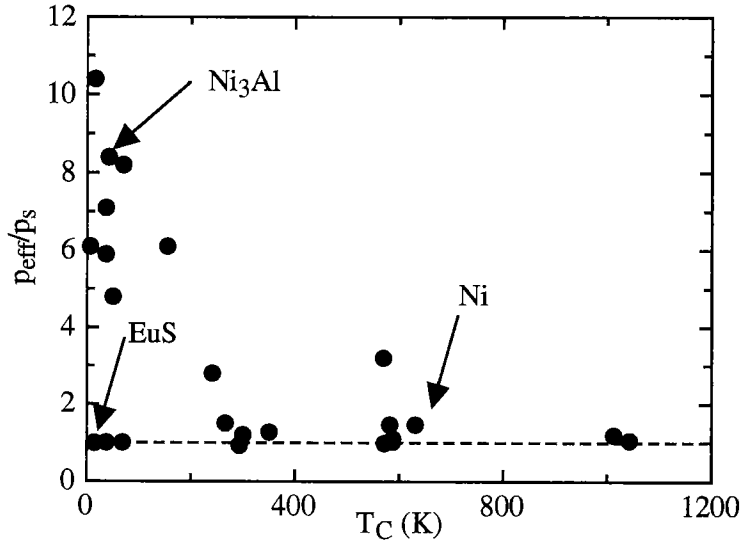


Figure 1.1: Rhodes-Wohlfarth plot for crystalline and amorphous ferromagnetic alloys. It shows the ratio p_{eff}/p_s as a function of the ordering temperature T_C , where p_{eff} is the effective magnetic moment in the paramagnetic phase, and p_s the saturation moment in the ordered phase. The values are taken from Ref. [1]. The dashed line represents the case of a perfect localised system, where $p_{eff} = p_s$.

In the case of electrons localised on the sites of a lattice, the Hamiltonian is based on the Heisenberg model

$$\mathcal{H}_{Heis} = - \sum_{i,j} J_{ij} \mathbf{S}_i \cdot \mathbf{S}_j, \quad (1.2)$$

that involves pair interaction between spins, coupled by the exchange integral J_{ij} . For itinerant electrons, a more appropriate model is the Hubbard Hamiltonian that accounts for a band electron approach

$$\mathcal{H}_{Hub} = -t \sum_{i,j} \sum_{\sigma} (c_{i\sigma}^{\dagger} c_{j\sigma} + c_{i\sigma} c_{j\sigma}^{\dagger}) + U \sum_j n_{j\uparrow} n_{j\downarrow}, \quad (1.3)$$

where the first term represents the kinetic energy t of the electrons (hopping integral) and the second term is the electrostatic repulsion U for electrons in the same orbital. In the limit of large Coulomb interactions ($U \gg t$) and at half-filling Eq. 1.3 reduces to Eq. 1.2 with J given by $J = 4t^2/U$ (see Ref. [2]).

The physical properties of a magnetic system are related to the temporal and spatial spin correlation function $G(\mathbf{r}, t)$, which is the Fourier transform of the dynamical susceptibility $\chi(\mathbf{q}, \omega)$ that is derived from the selected model Hamiltonian. $\chi(\mathbf{q}, \omega)$ describes the static (with $\omega=0$) and dynamical properties of a magnetic material, where \mathbf{q} and ω represent the wave vector and the energy of the magnetic fluctuations, respectively.

For a given system, $\chi(\mathbf{q}, \omega)$ will have different \mathbf{q} , energy and temperature behaviour depending on the degree of localisation of the electrons. For itinerant systems, the long wavelength and low energy fluctuations are responsible for most of the thermodynamic properties of the compounds. In contrast, for the localised spin systems, the information is distributed over a wide range of $q = |\mathbf{q}|$ and energy. The limit in q is given by the wavevector at the zone boundary q_{ZB} , that defines a minimal wavelength λ_{min} for the spin fluctuations via the relation $q_{ZB} = \frac{2\pi}{\lambda_{min}}$. This consideration is of course not relevant for itinerant systems where the electrons are delocalised. Furthermore, the spin correlation length is larger in metals than in insulators. The temperature evolution of the fluctuation spectrum is hence expected to be different for both types of systems.

An extensive review of the status of the knowledge on magnetic materials can be found in the books of Borovik-Romanov and Sinha [3] and Moriya [4].

In this work, we present investigations that were performed on various magnetic systems, each of which belongs to a specific class of materials that were listed above. On the basis of the current knowledge on localised spin systems, **the question arises if the universality of critical phenomena**, i.e. the fluctuations responsible for the phase transition, **can also embrace the itinerant magnets**. It is indeed believed according to dynamical scaling theory on Heisenberg systems that the decisive parameters are the long wavelength magnetic fluctuations, i.e. the one that are predominant in the itinerant systems. In order to answer this question, we study the dynamical magnetic spectrum of two metals, Ni_3Al and Ni , by means of the neutron scattering technique.

In addition, the discovery of magnetic systems with new properties like heavy fermion systems and non Fermi liquids has opened new fields of investigation, both experimentally and theoretically. It is known that **the spin channel dominates in the thermodynamic properties of such compounds**, and that **their magnetic spectrum is similar to the one of weak itinerant ferromagnets**. A detailed knowledge of spin dynamics in these latter compounds can therefore be a fruitful starting point for understanding the physics of these new materials.

In localised systems one would expect intuitively that the lifetime of the magnetic

fluctuations becomes vanishingly small when the kinetic energy is infinite. Surprisingly, theoretical investigations on a Heisenberg system predict that **spin fluctuations can persist near the zone boundary with a finite lifetime, even in the limit of infinite temperature** [5]. It is therefore of interest to test this astonishing prediction in EuS, which is a well known localised spin system.

Finally, the discovery of high-temperature superconductors has generated a renewed interest in the experimental investigation of low dimensional spin systems, as the 2D CuO_2 planes are believed to play an essential role in the transport properties of these compounds. The research in low dimensional spin systems has also been stimulated by the Haldane conjecture [6] that predicts gapless excitations for half integer-spin chains, whereas integer-spin chains are expected to exhibit a gap. Furthermore, the study of spin-lattice interaction has been promoted by the discovery of a spin-Peierls transition in organic compounds [7], where an antiferromagnetic chain becomes dimerised at a certain temperature, and a non magnetic ground state is generated. CuGeO_3 is a specimen which holds several of these attractive physical properties. The pure compound exhibits indeed a spin-Peierls transition at low temperature. On the other hand, **the introduction of doping elements, which is easier to perform than in organic compounds, can progressively release the spin-lattice coupling and generate a magnetic phase that is close to a low-dimensional spin system.** An investigation of the static and dynamic properties of CuGeO_3 with various doping concentration is expected to provide an insight into the interplay between the magnetic ground state and the lattice dimerisation.

Chapter 2

Neutron Scattering

*The fundamental principle of science, the definition almost, is this:
the sole test of the validity of any idea is experiment.*

Richard P. Feynman

2.1 Introduction

The intrinsic properties of the neutron make it an ideal probe for investigating the physics of condensed matter. As one of the advantages, its large penetration depth due to the absence of an electrical charge allows to probe materials of macroscopic size. The neutron interacts with matter via two types of processes. The nuclear interaction with the nuclei provides information about structural properties as well as lattice dynamics. The interaction of the neutron spin with the electronic and nuclear spins of the system allows the investigation of the static and dynamical magnetic properties of a compound.

The current neutron sources are able to produce neutron beams in an energy range that covers the basic excitation energies which are relevant for the understanding of the physics in solids and liquids. In addition, the corresponding wavelength range of the neutrons is similar to interatomic distances. The excitations can be therefore investigated over the whole Brillouin zone, which is not the case with any other spectroscopic technique. A restriction is however given by the limited flux of the neutron sources when compared for instance with synchrotron sources.

In this Chapter we present an overview of the principles of neutron scattering and introduce some concepts and formulae that are relevant for the present work. We refer to the text books of Lovesey [8] and Squires [9] for the detailed derivation of the theory.

2.2 Neutron-matter interaction

The interaction of the neutrons with matter is described by the quantum theory of scattering. In a neutron experiment, the measured quantity is the number of

neutrons scattered in a solid angle $d\Omega$ with an energy between E_f and $E_f + dE_f$. This quantity can be expressed as follows:

$$\left(\frac{d\sigma^2}{d\Omega dE_f}\right)_{\mathbf{k}_i\sigma_i\lambda_i\rightarrow\mathbf{k}_f\sigma_f\lambda_f} = \frac{1}{\Phi} \frac{1}{d\Omega} \sum_{\mathbf{k}_f\in d\Omega} W_{\mathbf{k}_i\sigma_i\lambda_i\rightarrow\mathbf{k}_f\sigma_f\lambda_f} \delta(\hbar\omega + E_{\lambda_i} - E_{\lambda_f}) \quad (2.1)$$

where Φ is the neutron flux, $d\Omega$ the solid angle in the scattered direction that is considered, and $W_{\mathbf{k}_i\sigma_i\lambda_i\rightarrow\mathbf{k}_f\sigma_f\lambda_f}$ the transition probability between an initial state $|\mathbf{k}_i\sigma_i\lambda_i\rangle$ and a final state $|\mathbf{k}_f\sigma_f\lambda_f\rangle$. The delta function guarantees the conservation of the total energy. The state of the total system *neutron+sample* is represented by $|\mathbf{k}\sigma\lambda\rangle$ where \mathbf{k} , σ and λ account for the neutron wavevector, the neutron spin state and the quantum state of the sample, respectively.

The scattering rate $W_{\mathbf{k}_i\sigma_i\lambda_i\rightarrow\mathbf{k}_f\sigma_f\lambda_f}$ can be calculated by using the *Golden Rule* of Fermi:

$$\sum_{\mathbf{k}_f\in d\Omega} W_{\mathbf{k}_i\sigma_i\lambda_i\rightarrow\mathbf{k}_f\sigma_f\lambda_f} = \frac{2\pi}{\hbar} \rho_{k_f} \left| \langle \mathbf{k}_f\sigma_f\lambda_f | \hat{V} | \mathbf{k}_i\sigma_i\lambda_i \rangle \right|^2 \quad (2.2)$$

where ρ_{k_f} is the density of states for k_f , and \hat{V} is the operator that represents the interaction between the neutron and the sample.

If the initial and final beams are not polarised, the neutron scattering cross-section is given by the following relation:

$$\left(\frac{d\sigma^2}{d\Omega dE_f}\right)_{\lambda_i\rightarrow\lambda_f} = \frac{k_f}{k_i} \left(\frac{m_n}{2\pi\hbar^2}\right)^2 \sum_{\lambda_i,\lambda_f,\sigma_i,\sigma_f} p_{\lambda_i} \left| \langle k_f\sigma_f\lambda_f | \hat{V} | k_i\sigma_i\lambda_i \rangle \right|^2 \delta(\hbar\omega + E_{\lambda_i} - E_{\lambda_f}) \quad (2.3)$$

where m_n the mass of the neutron and p_{λ_i} is the probability that the sample is in the initial state $|\lambda_i\rangle$.

In a scattering process, the usual convention is to define the energy and momentum transfer conservation laws of the total system as follows:

$$\hbar\omega = E_i - E_f = \frac{\hbar^2}{2m_n} (k_i^2 - k_f^2) \quad (2.4)$$

$$\hbar\mathbf{Q} = \hbar(\mathbf{k}_i - \mathbf{k}_f) \quad (2.5)$$

where $\hbar\omega$ is the energy transfer and $\hbar\mathbf{Q}$ momentum transfer. \mathbf{Q} is defined as the scattering vector. E_i and E_f are the initial and final energy of the neutron, respectively.

2.2.1 Nuclear scattering

The nuclear forces between the neutron and a nucleus are of very short range (of the order of 1 fm) when compared with the typical interatomic spacing. The Fermi

pseudopotential can therefore be used as a reasonable approximation of the neutron-nucleus interaction:

$$\hat{V}(\mathbf{r}) = \sum_j \frac{2\pi\hbar^2}{m_n} b_j \delta(\mathbf{r} - \mathbf{R}_j), \quad (2.6)$$

where b_j is the scattering length of the nucleus of type j and \mathbf{R}_j is its position in the sample.

After introducing the Fermi pseudopotential in Eq. 2.3, the thermal average and the sum over all the scattering elements yield (see for example Ref. [9]):

$$\begin{aligned} \left(\frac{d\sigma^2}{d\Omega dE_f} \right) &= \left(\frac{d\sigma^2}{d\Omega dE_f} \right)_{coh} + \left(\frac{d\sigma^2}{d\Omega dE_f} \right)_{inc} \\ &= \frac{\sigma_{coh} k_f}{4\pi k_i} N S_{coh}(\mathbf{Q}, \omega) + \frac{\sigma_{inc} k_f}{4\pi k_i} N S_{inc}(\mathbf{Q}, \omega) \end{aligned} \quad (2.7)$$

The scattering function $S(\mathbf{Q}, \omega)$ is the Fourier transform in space and time of the pair-correlation function $G(\mathbf{r}, t)$ of the system:

$$S(\mathbf{Q}, \omega) = \frac{1}{2\pi\hbar} \int G(\mathbf{r}, t) e^{i(\mathbf{Q}\cdot\mathbf{r} - \omega t)} d\mathbf{r} dt \quad (2.8)$$

In Eq. 2.7, S_{coh} represents the coherent scattering of elements that are correlated in space and time, whereas S_{inc} gives only the space correlation of the same nucleus at different times. The coherent scattering can thus give rise to interference effects which provide information about the collective excitations of the material.

The quantities σ_{coh} and σ_{inc} in Eq. 2.7 are defined as follows:

$$\sigma_{coh} = 4\pi(\bar{b})^2, \quad \text{and} \quad \sigma_{inc} = 4\pi\{\bar{b}^2 - (\bar{b})^2\} \quad (2.9)$$

These latter quantities have the dimension of a surface and can be interpreted as the area of the nucleus that the neutron sees.

Using Eq. 2.6, the nuclear coherent elastic ($E_i = E_f$) cross-section for an ordered crystal can be expressed as:

$$\left(\frac{d\sigma}{d\Omega} \right)_{coh.el.} = N \frac{(2\pi)^3}{v_o} \sum_{\boldsymbol{\tau}} \delta(\mathbf{Q} - \boldsymbol{\tau}) |F_N(\boldsymbol{\tau})|^2, \quad (2.10)$$

N is the number of unit cells in the sample, $\boldsymbol{\tau}$ is a reciprocal lattice vector and v_o is the volume of the unit cell.

$$F_N(\boldsymbol{\tau}) = \sum_d \bar{b}_d e^{i\boldsymbol{\tau}\cdot\mathbf{d}} e^{-W_d} \quad (2.11)$$

is the nuclear structure factor. \sum_d extends over all the atoms of the unit cell, \bar{b}_d is the coherent scattering length and e^{-W_d} the Debye-Waller factor of the atom at the site d .

In contrast, the incoherent elastic nuclear cross-section is given by the following relation:

$$\left(\frac{d\sigma}{d\Omega}\right)_{inc.el.} = N \sum_d (\bar{b}_d^2 - (\bar{b}_d)^2) e^{-2W_d} \quad (2.12)$$

This expression does not yield any information about the lattice properties, as this process describes uncorrelated movements of nuclei.

2.2.2 Magnetic scattering

The interaction between the magnetic moment of the neutron μ_n and the magnetic field generated by the unpaired electrons of an atom makes neutron scattering a powerful tool for the investigation of the magnetic properties of condensed matter. For an unpaired electron, the corresponding magnetic interaction operator is:

$$\hat{V}_m(\mathbf{r}) = -\boldsymbol{\mu} \cdot \mathbf{B} = -\gamma \mu_N \boldsymbol{\sigma} \cdot \mathbf{B}(\mathbf{r}) \quad (2.13)$$

where $\gamma = -1.913$ is the gyromagnetic ratio of the neutron; μ_N the nuclear magneton; $\boldsymbol{\sigma}$ the Pauli spin operator. $\mathbf{B}(\mathbf{r})$ is the magnetic field induced at the position \mathbf{r} by a single unpaired electron:

$$\mathbf{B}(\mathbf{r}) = \nabla \times \left\{ \frac{\boldsymbol{\mu}_e \times \mathbf{r}}{|\mathbf{r}|^3} \right\} + \frac{(-e) \mathbf{v}_e \times \mathbf{r}}{c |\mathbf{r}|^3}. \quad (2.14)$$

The first term in Eq. 2.14 is the field generated by the magnetic moment of the electron ($\boldsymbol{\mu}_e = -2\mu_B \mathbf{S}$). The second term is related to the electronic orbital motion, where \mathbf{v}_e is the velocity of the electron, e its charge and c is the velocity of light. The magnetic cross-section for a crystal is obtained by evaluating the matrix elements $\langle k_f \sigma_f \lambda_f | \hat{V}_m | k_i \sigma_i \lambda_i \rangle$. For an unpolarised neutron beam, by using Eq. 2.13 and Eq. 2.14, one obtains:

$$\begin{aligned} \left(\frac{d\sigma^2}{d\Omega dE_f}\right) &= \frac{(\gamma r_0)^2 k_f}{2\pi \hbar k_i} \sum_{\alpha\beta} (\delta_{\alpha\beta} - \hat{Q}_\alpha \hat{Q}_\beta) \sum_{j'j} \frac{1}{4} g_{j'} g_j F_{j'}^*(\mathbf{Q}) F_j(\mathbf{Q}) \quad (2.15) \\ &\times \int_{-\infty}^{+\infty} \langle e^{-i\mathbf{Q} \cdot \mathbf{R}_{j'}(0)} e^{i\mathbf{Q} \cdot \mathbf{R}_j(t)} \rangle \langle S_{j'}^\alpha(0) S_j^\beta(t) \rangle e^{-i\omega t} dt \end{aligned}$$

In the latter equation, r_0 is the classical radius of the electron. The term $(\delta_{\alpha\beta} - \hat{Q}_\alpha \hat{Q}_\beta)$ is the polarisation factor, where $\alpha, \beta = x, y, z$. It accounts for the fact that the components of the spin operator $\mathbf{S}(t)$ that are parallel to the scattering vector \mathbf{Q} cannot be observed in a neutron scattering process. g_j and $F_j(\mathbf{Q})$ correspond, respectively, to the Landé factor and the Fourier transform (magnetic form factor) of the spin density of the magnetic ion j . $\mathbf{R}_j(t)$ gives the position of the ion j at time t . Finally, $\langle S_{j'}^\alpha(0) S_j^\beta(t) \rangle$ is the spin correlation function. If one considers now all the magnetic ions to be identical, Eq. 2.15 is expressed as follows:

$$\left(\frac{d\sigma^2}{d\Omega dE_f}\right) = \frac{k_f}{k_i} (\gamma r_o \frac{1}{2} g F_j(\mathbf{Q}))^2 \sum_{\alpha\beta} (\delta_{\alpha\beta} - \hat{Q}_\alpha \hat{Q}_\beta) S^{\alpha\beta}(\mathbf{Q}, \omega) \quad (2.16)$$

where the magnetic scattering function $S^{\alpha\beta}(\mathbf{Q}, \omega)$ is introduced:

$$S^{\alpha\beta}(\mathbf{Q}, \omega) = \frac{1}{2\pi\hbar} \int_{-\infty}^{+\infty} \sum_{j,j'} \langle e^{-i\mathbf{Q}\cdot\mathbf{R}_{j'}(0)} e^{i\mathbf{Q}\cdot\mathbf{R}_j(t)} \rangle \langle S_{j'}^\alpha(0) S_j^\beta(t) \rangle e^{-i\omega t} dt \quad (2.17)$$

The magnetic scattering function is the Fourier transform in space and time of the magnetic pair correlation function. It gives the probability for the system to have a magnetic moment at a position $R_j(t)$ with a component $S_j^\beta(t)$ and a magnetic moment at a position $R_{j'}(0)$ with a component $S_{j'}^\alpha(0)$.

2.2.3 Generalised susceptibility

In a sample, the magnetic moment of the neutron can be seen as an external perturbing magnetic field $\mathbf{H}(\mathbf{Q}, \omega)$. The response of the sample can be monitored with the dynamical magnetisation $\mathbf{M}(\mathbf{Q}, \omega)$:

$$\mathbf{M}^\alpha(\mathbf{Q}, \omega) = \sum_{\beta} \chi^{\alpha\beta}(\mathbf{Q}, \omega) \mathbf{H}_\beta(\mathbf{Q}, \omega) \quad (2.18)$$

where the generalised dynamical susceptibility tensor $\chi^{\alpha\beta}(\mathbf{Q}, \omega)$ mirrors the spatial and dynamical magnetic properties of the sample.

The magnetic scattering function $S^{\alpha\beta}(\mathbf{Q}, \omega)$ (see Eq. 2.17) can be related to the imaginary part of the dynamical susceptibility $\chi^{\alpha\beta}(\mathbf{Q}, \omega)$ via the fluctuation-dissipation theorem [10]:

$$S^{\alpha\beta}(\mathbf{Q}, \omega) = \frac{\hbar}{\pi} \frac{1}{1 - e^{-\hbar\omega/k_B T}} \Im \chi^{\alpha\beta}(\mathbf{Q}, \omega) \quad (2.19)$$

The magnetic neutron cross-section can therefore directly probe the magnetic response function of a system.

Finally, by using linear response theory, the magnetic neutron cross-section can be rewritten as:

$$\begin{aligned} \left(\frac{d\sigma^2}{d\Omega dE_f}\right) &= \frac{k_f}{k_i} (\gamma r_o \frac{1}{2} g F_j(\mathbf{Q}))^2 \exp\{-2W(\mathbf{Q})\} \frac{\omega}{1 - e^{-\beta\omega}} \\ &\times \frac{N}{(g\mu_B)^2} \sum_{\alpha\beta} (\delta_{\alpha\beta} - \hat{Q}_\alpha \hat{Q}_\beta) \chi^{\alpha\beta}(\mathbf{Q}) F^{\alpha\beta}(\mathbf{Q}, -\omega) \end{aligned} \quad (2.20)$$

where $F^{\alpha\beta}(\mathbf{Q}, \omega)$ is a normalised spectral weight function and μ_B the Bohr magneton.

2.3 Instrumentation

2.3.1 Three-axis spectrometer

The three-axis spectrometer is an instrument that allows to measure the intensity of scattered neutrons for a particular momentum transfer \mathbf{Q} and energy transfer $\hbar\omega$. This feature is particularly useful for a measurement of inelastic scattering from single crystals.

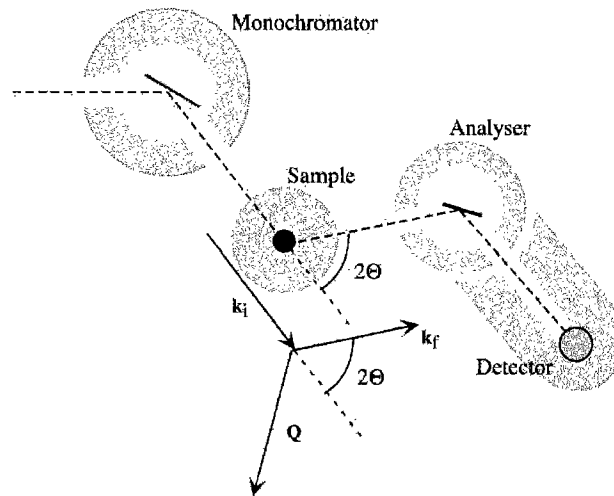


Figure 2.1: Layout of a three-axis spectrometer. The three axes consist of (i) monochromator (ii) sample and (iii) analyser. Θ is the scattering angle. The corresponding scattering geometry in the reciprocal space is also shown.

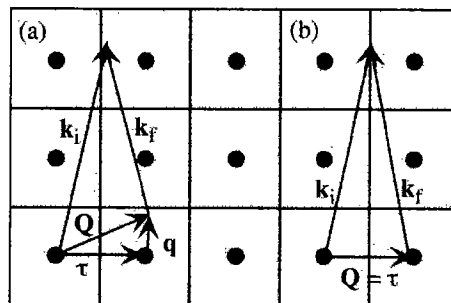


Figure 2.2: (a) Scheme of an inelastic scattering process, $|\mathbf{k}_f| \neq |\mathbf{k}_i|$. The scattering vector \mathbf{Q} is decomposed into a reciprocal lattice vector $\boldsymbol{\tau}$ and the wavevector \mathbf{q} of the excitation that is analysed. (b) If \mathbf{Q} coincides with $\boldsymbol{\tau}$ and $|\mathbf{k}_f| = |\mathbf{k}_i|$, the process describes Bragg scattering.

The instrument is composed of three main parts (see Fig. 2.1). The incident neutron wavevector \mathbf{k}_i is selected out of the white neutron beam via a Bragg reflection from a monochromator (first axis) consisting of aligned single crystal blades (usually pyrolytic graphite or copper). The monochromatic beam is scattered from the sample (second axis) with a selected scattering angle Θ . The scattered beam is analysed via a second Bragg reflection from an analyser (third axis), which defines the final

wavevector of the neutron \mathbf{k}_f . The simultaneous selection of \mathbf{k}_i , \mathbf{k}_f and Θ hence allows to measure the scattering function of the sample at a given momentum and energy transfer. For the study of an excitation (magnetic or nuclear), a single crystal can be oriented such that the scattering vector \mathbf{Q} coincides with $\boldsymbol{\tau} + \mathbf{q}$, where $\boldsymbol{\tau}$ is a vector of the reciprocal lattice and \mathbf{q} is the wavevector of the excitation (see Fig 2.2 (a)). For the particular case of $\mathbf{q} = 0$ and $|\mathbf{k}_i| = |\mathbf{k}_f|$, the so-called scattering triangle reduces to Bragg scattering, as shown in Fig 2.2 (b).

The inelastic neutron experiments presented in this work were performed on the three-axis spectrometers for cold neutrons FLEX (HMI, Berlin) and TASP (SINQ, PSI-Villigen).

2.3.2 Small angle neutron scattering

Small angle neutron scattering (SANS) is a diffraction technique for investigating large scale (small scattering vectors \mathbf{Q}) properties in condensed matter. The technique consists of illuminating a sample with a monochromatic neutron beam, and collecting the scattering intensity on a position sensitive two-dimensional detector. The typical sample-detector distance is usually between 2 and 20 m (see Fig. 2.3).

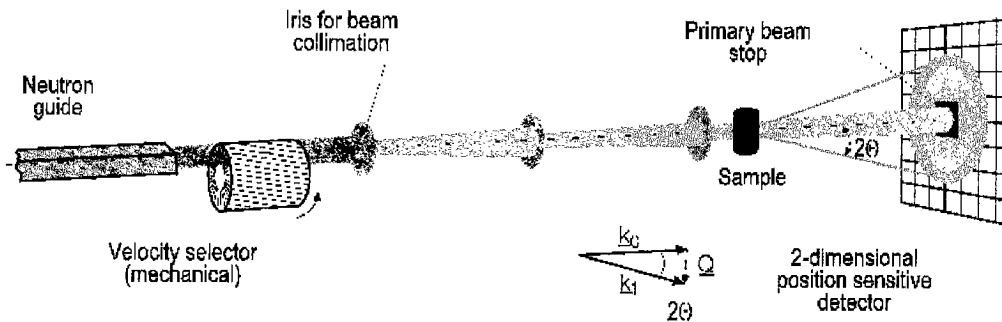


Figure 2.3: Layout of a small angle neutron scattering diffractometer.

In a SANS experiment, the measured quantity is $I(\mathbf{Q})$, where \mathbf{Q} is the scattering vector. The SANS experiments that we have performed in the present work are restricted to scattering processes in the forward direction, i.e. where $\boldsymbol{\tau} = 0$, and therefore \mathbf{Q} is equivalent to \mathbf{q} . Generally, the entire neutron-sample interaction is dominated by elastic scattering and can be described by the single parameter \mathbf{Q} . If in addition the interaction is isotropic, $I(\mathbf{Q}) = I(Q)$.

Ideally, $I(\mathbf{Q})$ is proportional to $S(\mathbf{Q}) = \int S(\mathbf{Q}, \omega) d\omega$. In practice, for a given scattering geometry, i.e. for a given pixel X on the detector (see Fig. 2.4), one measures the integral along a constant scattering angle curve and not along a constant scattering vector curve:

$$I(\mathbf{Q}_0) = \int S(\mathbf{Q}(\omega, 2\theta), \omega) d\omega \quad (2.21)$$

where \mathbf{Q}_0 is the elastic scattering vector for a given scattering angle 2θ . The integral is taken over the energy transfer, i.e. over k_f , and the scattering vector $\mathbf{Q}(\omega, 2\theta)$

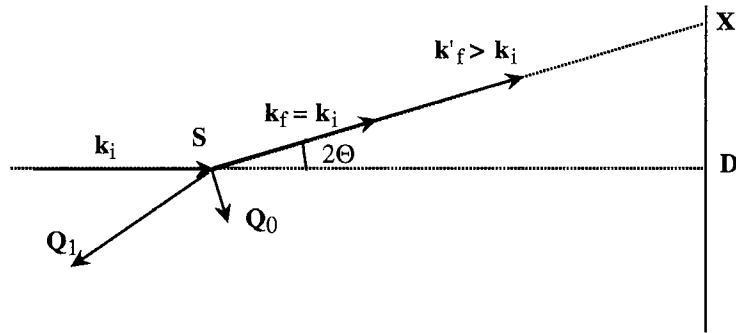


Figure 2.4: Scattering geometry on SANS. \mathbf{k}_i is the incident wavevector of the neutron. D and X are the detector and a single pixel of the detector, respectively. 2Θ is the scattering angle corresponding to the position X . For elastic scattering $|\mathbf{k}_f| = |\mathbf{k}_i|$ and the elastic scattering vector is \mathbf{Q}_0 . Another possible scattering process is also shown, with $|\mathbf{k}'_f| > |\mathbf{k}_i|$, that may also contribute to the intensity in the detector for the same scattering angle. In this case, the corresponding scattering vector is \mathbf{Q}_1 , different from \mathbf{Q}_0 .

is modified according to the kinematical relations (Eq. 2.4 and Eq. 2.5) along the integral path.

The small angle neutron experiments presented in this work were performed on the small angle scattering instrument SANS (SINQ, PSI-Villigen) and on D11 (ILL, Grenoble).

Chapter 3

Muon Spin Rotation Spectroscopy

*I do not see why the men who believe in electrons are regarded
as less credulous than men who believe in angels.*

George Bernard Shaw

3.1 Introduction

In contrast to the neutron scattering technique where the information is averaged over the whole volume of the sample, Muon Spin Rotation (μ SR) spectroscopy is an ideal probe to characterise the local magnetic properties of a system. The two techniques are therefore expected to provide a complementary approach for the investigation of magnetism in solid state physics. In this Chapter, a brief overview of the technique is presented. For a comprehensive review of μ SR history, technique and applications we refer to the book of A. Schenck [11].

3.2 μ SR technique

The muon is generated by the decay of a pion via the following reaction:



with a lifetime τ_π of about 26 ns. According to the conservation of the total momentum-energy, the muon beam is 100% polarised antiparallel to its flight path in the rest frame of the pion. This excellent polarisation is conserved in the laboratory frame for the so-called surface muons that arise from π^+ decaying at rest near the surface of the production target. At the muon facility at PSI, the pions are produced by a high energy proton beam directed on a graphite target, via the following reaction:



In the sample, the muons are implanted at particular crystallographic sites and interact with the local electromagnetic field via hyperfine interaction and possibly

undergo a depolarisation. The muon subsequently decays with a mean lifetime of $\tau_\mu = 2.2 \mu\text{s}$ via the process:



The positrons e^+ are preferentially emitted along the muon spin direction, due to the parity violation of this decay. The signal is recorded by a positron detector which is set up in a particular direction, with a given solid angle of acceptance. Each muon that is implanted in the sample starts a clock that is stopped when the corresponding positron is detected. The resolution of the measurement depends hence on various parameters like the time accuracy of the clock and the ability of distinguishing correlated events. Eventually, a muon decay histogram is recorded, collecting typically 10^7 to 10^8 events, which provide the positron depolarisation $N_{e^+}(t)$ as a function of time:

$$N_{e^+}(\theta, t) = \frac{N_0}{\tau_\mu} \exp\left(-\frac{t}{\tau_\mu}\right) [1 + AG(t)] + B \quad (3.4)$$

and $G(t) = \frac{|\mathbf{P}_\mu(t)|}{|\mathbf{P}_\mu(0)|} \cos \theta.$

N_0 is a normalisation constant; B is a time-independent background; $A \approx 0.3$ is the asymmetry factor for the muon decay and $G(t)$ is the time-normalised polarisation of the muon. θ defines the angle between the μ^+ spin and the positron trajectory, i.e. the direction of the detector. $G(t)$ reflects the normalised μ^+ spin autocorrelation function and is a the signature of the magnetic interaction between the muon and the crystal. The product $AG(t)$ is often referred as the muon signal.

In the case of static local magnetic fields (\mathbf{B}_μ) at the muon site, the depolarisation function $G(t)$ is given by:

$$G(t) = \int f(\mathbf{B}_\mu) [\cos^2 \theta + \sin^2 \theta \cos(\gamma_\mu B_\mu t)] d\mathbf{B}_\mu, \quad (3.5)$$

where $f(\mathbf{B}_\mu)$ is the magnetic field distribution function, θ is the angle between the local field and the initial muon polarisation $|\mathbf{P}_\mu(0)|$ and $\gamma_\mu/(2\pi) = 13.553\,879$ kHz/G is the gyromagnetic ratio of the muon. For a particular structure the possible presence of different μ^+ stopping sites with different magnetic environments will be identified by a μ SR signal with different components $G_i(t)$.

μ SR is essentially performed with μ^+ particles. The μ^- are indeed captured into atomic orbitals of the target, which eventually reduces considerably their polarisation. In addition, the probability of nuclear capture in the target sample is important and leads to a shortening of the μ^- lifetime. These two drawbacks render the μ^- SR signal much more difficult to observe than the one of μ^+ SR. The μ SR experiments that are presented in Chapter 6 were performed with the μ^+ SR technique.

3.3 Zero field μ SR

Zero field μ SR refers to the experimental situation where no external magnetic field is applied to the sample. In the case of a well defined magnetic field \mathbf{B}_μ at the muon site, the magnetic moment of the muon will precess with a Larmor frequency ω_μ . From Eq. 3.5, the time-normalised polarisation is given by:

$$G(t) = \cos^2 \theta + \sin^2 \theta \cos(\omega_\mu t + \phi) \quad (3.6)$$

ϕ is the angle between the direction of the detector and the initial muon polarisation $\mathbf{P}_\mu(0)$, and $\omega_\mu = \gamma_\mu |\mathbf{B}_\mu|$.

In a more realistic picture, one can assume a local gaussian distribution of the field components at the muon site. It essentially originates from the nuclear dipole moments that are static within the μ SR time window. An average over all directions yields the Kubo-Toyabe function [12]:

$$G(t) = \frac{1}{3} + \frac{2}{3}(1 - \gamma_\mu^2 \Delta^2 t^2) \exp\left(-\frac{1}{2} \gamma_\mu^2 \Delta^2 t^2\right) \quad (3.7)$$

where Δ is the width of the local field distribution. The first part of Eq. 3.7 corresponds to the fraction of muons that do not precess since on average $\frac{1}{3}$ of the field distribution is parallel to the initial muon polarisation.

The case of fluctuating magnetic fields leads to a relaxation of the non-precessing as well as of the precessing muons:

$$G(t) = \frac{1}{3} \exp(-\lambda_1 t) + \frac{2}{3} \exp(-\lambda_2 t) (1 - \gamma_\mu^2 \Delta^2 t^2) \exp\left(-\frac{1}{2} \gamma_\mu^2 \Delta^2 t^2\right) \quad (3.8)$$

where λ_1 and λ_2 are relaxation rates. The time fluctuation of the field distribution can be caused by spin-lattice or spin-spin coupling.

The advantage of the zero-field μ SR technique is the possibility of investigating magnetic properties in a non-perturbative environment. This technique is for example very valuable for detecting spontaneous μ^+ Larmor frequencies in magnetically ordered phases.

3.4 Transverse field μ SR

In transverse field μ SR, a static external magnetic field \mathbf{H}_{ext} is applied perpendicular to the initial muon polarisation. The muon spin precesses around the total field \mathbf{B}_μ at the muon site, which results from the sum of the local internal field and the applied field.

In an inhomogeneous field distribution, the μ^+ implanted at different sites will feel slightly different fields. In transverse fields experiments H_{ext} is usually larger than the internal fields and only the field inhomogeneity along the direction of \mathbf{H}_{ext} (taken as the z direction) has to be considered. Noting that $\theta = 90^\circ$, Eq. 3.6 becomes:

$$G(t) = g_{TF}(t) \cos(\gamma_\mu \langle B_\mu^z \rangle t). \quad (3.9)$$

B_μ^z is the average of the component along \mathbf{H}_{ext} of the total field at the muon site. $g_{TF}(t)$ is the depolarisation function and depends on the type of field distribution in the sample.

3.5 Instrumentation

The μ SR spectra presented in Chapter 6 were measured on the spectrometers GPS and LTF at the muon facility of PSI.

The General Purpose Spectrometer (GPS) is equipped with a “top loading” continuous-flow ^4He evaporation cryostat, that operates between 2K and 300K. The external magnetic fields can be generated by two separate pairs of Helmholtz coils, allowing to achieve up to 0.6 T parallel to the muon polarisation and up to 10 mT transverse to it. Five positron detectors are located in the up, down, backward, forward and right direction with respect to the incoming muon beam. A special additional detector setup, the so-called veto, acts as a discriminator for ensuring the correlation between an incoming muon and an emitted positron.

The Low Temperature Facility (LTF) is equipped with a ^3He - ^4He -dilution refrigerator which operates in the temperature range of 25 mK up to 20 K. As in GPS a set of two separate Helmholtz coils can generate a longitudinal field (up to 3 T) and a transverse field (up to 10 mT). The positrons are detected by 4 detectors, forward, backward, right and left with respect to the incoming muon momentum. Since no veto system is installed, the background due to non correlated events is higher than in GPS.

Chapter 4

Theory of the spin dynamics in magnetically ordered systems

I'm astounded by people who want to 'know' the universe when it's hard enough to find your way around Chinatown.

Woody Allen

4.1 Introduction

In this Chapter we present some theoretical models which describe the static and dynamical properties of magnetic systems.

The fundamental model that depicts a collection of interacting spins in a system with localised electrons is the Heisenberg Hamiltonian,

$$\mathcal{H}_{ex} = - \sum_{i,j} J_{ij} \mathbf{S}_i \cdot \mathbf{S}_j, \quad (4.1)$$

where J_{ij} is the exchange integral between two spins at the sites i and j ($J_{ii} = 0$). This latter interaction accounts for the Coulomb repulsion between electrons as well as for the Pauli exclusion principle. If one considers the dipolar forces between spins, an additional interaction term can be introduced, which is purely of magnetic origin. The exchange Hamiltonian (Eq. 4.1) is then modified as follows:

$$\mathcal{H}_{dip} = - \sum_{i,j} \sum_{\alpha,\beta} U_{ij}^{\alpha\beta} S_i^\alpha S_j^\beta \quad (4.2)$$

where $U_{ij}^{\alpha\beta} = J_{ij} \delta^{\alpha\beta} + g (\delta^{\alpha\beta}/r_{ij}^3 - 3 r_{ij}^\alpha r_{ij}^\beta / r_{ij}^5)$, g denotes the strength of the dipolar interaction that are long range and anisotropic and r_{ij} is the distance between the spins i and j .

For the description of phase transitions and critical phenomena two different sets of thermodynamical variables have to be distinguished: the intrinsic properties of the system that are extensive (internal energy U , free energy F , entropy \mathcal{S} , magnetisation M), and the applied fields (temperature T , pressure p , external magnetic field

h) [13]. In the case of a magnetic system, the magnetisation M plays the role of the order parameter. This latter quantity is the total magnetisation for a ferromagnet (FM), or the staggered magnetisation for an antiferromagnet (AF). M is zero in the disordered phase and takes a finite value when the system orders. M as well as the other thermodynamic equilibrium properties, like the susceptibility χ and the specific heat C_p (Eq. 4.3 to 4.5) can be derived from the free energy $F = U - T\mathcal{S}$, which accounts for the balance between internal energy U and entropy \mathcal{S} in the system.

$$M(T) = -\left.\frac{\partial F}{\partial h}\right|_T \quad (4.3)$$

$$\chi(T) = \left.\frac{\partial M}{\partial h}\right|_T \quad (4.4)$$

$$C_p(T) = -T\left.\frac{\partial^2 F}{\partial T^2}\right|_h \quad (4.5)$$

F is related to the partition function Z , which is determined via the eigenvalues of the Hamiltonian:

$$F = k_B T \ln Z \quad (4.6)$$

$$Z = \text{Tr} e^{-\mathcal{H}/k_B T} \quad (4.7)$$

The knowledge of the Hamiltonian is therefore the fundamental starting point for describing and understanding the physical properties of a system.

4.2 Static properties

The temperature, T_C (FM) or T_N (AF), at which the magnetisation becomes zero (for $h=0$) is called the critical point. Below this temperature the magnetic moments are ordered, whereas above it they are randomly oriented and the long range magnetic order is lost.

In a second order phase transition, the equilibrium variables are observed to diverge at the transition temperature T_C . Near the critical point, these quantities can be expressed in terms of power laws of the reduced temperature $\tau = T/T_C - 1$:

$$M(T) = M_0 |\tau|^\beta \quad (4.8)$$

$$\chi(T) = \chi_0 |\tau|^{-\gamma} \quad (4.9)$$

$$\xi(T) = \xi_0 |\tau|^{-\nu} \quad (4.10)$$

$$C_p|_{h=0} = C_0 |\tau|^{-\alpha} \quad (4.11)$$

where β , γ , ν and α are the critical exponents. The variable ξ is the correlation length: an estimation of the distance over which the magnetic moments perceive each other.

Table (4.1) gives a list of the calculated critical exponents which were obtained within the framework of different standard models.

	d	n	α	β	γ	ν
Mean Field			0	0.5	1	
Ising	2	1	0	0.125	1.75	1
Ising	3	1	0.013(1)	0.312(3)	1.250(2)	0.638(2)
XY	3	2	-0.02(3)		1.318(10)	0.670(6)
Heisenberg	3	3	-0.14(6)	0.38(3)	1.375(2)	0.703(10)
Dipolar	3	3	$-\frac{1}{34}\epsilon +$	$\frac{1}{2} - \frac{2}{17}\epsilon$	$1 + \frac{9}{34}\epsilon$	$\frac{1}{2}/(1 - \frac{9}{34}\epsilon)$

Table 4.1: Critical exponents calculated for several standard models that involve only exchange interactions [13]. d corresponds to the dimensionality of the system, whereas n represents the dimension of the order parameter. The last line corresponds to a Heisenberg model including dipolar interaction [21] (see Section 4.3.2). The variable ϵ is introduced from renormalisation group theory which can be solved for $d = 4$ and is then extended to $d = 4 - \epsilon$. All the values are correct to the order of $O(\epsilon^2)$.

In the sixties, Kadanoff [14] has proposed a scaling conjecture in order to explain the critical behaviour of a spin system near T_C . The basic idea of this hypothesis is that the long range correlation of spin fluctuations near T_C is responsible for the phase transition, namely for all singular behaviour. This statement is related to the existence of a characteristic length ξ , the above mentioned spin correlation length (Eq. 4.10), which is infinite at the ordering temperature. In other words the scaling conjecture states that all physical quantities scale with the spin correlation length. Under this assumption, the critical exponents are expected to be universal, according to the fact that for a given class of systems (e.g. Heisenberg ferromagnets) they do not depend upon the type of compound or the local details of the system, but rather on global properties like the dimensionality of the system d and the dimension of the order parameter n (see Table 4.1). Thus two important consequences can be inferred from the scaling hypothesis: the critical exponents are related via scaling laws, and the spin correlation function as well as the temperature range of the fluctuations scale with the correlation length of the system.

In the ordered phase of a single domain isotropic ferromagnet, the direction of the magnetisation defines three natural directions linked with three diagonal components of the susceptibility tensor, one along M ($\chi_{\parallel}(\mathbf{q})$) and two transverse to it ($\chi_{\perp 1,2}(\mathbf{q})$) which are degenerate. In a mean field theory, the static susceptibilities for an isotropic ferromagnet are expressed as follows:

$$\chi_{\perp 1,2}(\mathbf{q}) \propto 1/q^2 \quad (4.12)$$

$$\chi_{\parallel}(\mathbf{q}) \propto 1/(q^2 + \kappa_-^2) \quad (4.13)$$

where \mathbf{q} is the reduced scattering vector and κ_- is the inverse correlation length below T_C . In the disordered phase, the order parameter becomes zero and the susceptibility is isotropic:

$$\chi_p(\mathbf{q}) \propto 1/(q^2 + \kappa_+^2) \quad (4.14)$$

The correlation length in the paramagnetic phase, κ_+ , has the same temperature dependence as the one below T_C , but the prefactor κ_0 ($= \xi_0^{-1}$ of Eq. 4.10) may be different.

In the vicinity of T_C and for large scales (i.e. small wavevectors q), the mean field approximation fails to describe the actual behaviour of magnets, because the fluctuations are neglected. The theory of critical scattering predicts hence asymptotic forms for the spin correlation functions, based on the static scaling hypothesis. The static susceptibility that is connected with the spin correlation function via the fluctuation-dissipation theorem (See Eq. 2.19) can be expressed as follows [15]:

$$\chi(q, \kappa) = q^{\eta-2} f_x(x), \quad (4.15)$$

where x is a scaling parameter defined as κ/q . The correction term to the mean field approximation is the ‘Fisher’ exponent η , the value of which is 0.042 ± 0.014 [16]. This relation means that the spin correlation function at any temperature and q near the phase transition is determined by the static properties at T_C , via the scaling function $f_x(x)$.

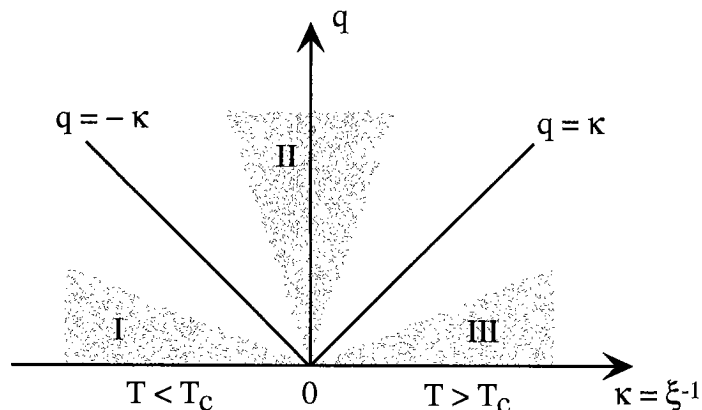


Figure 4.1: Diagram for the static susceptibility as a function of wave number q and inverse correlation length κ . Three asymptotic regions can be defined: (I) Hydrodynamic region in the ordered phase [$x = \kappa/q \gg 1$, $T < T_C$], (II) Critical region [$x = \kappa/q \ll 1$], (III) Hydrodynamic region in the disordered phase [$x = \kappa/q \gg 1$, $T > T_C$].

The significance of the role played by the correlation length ξ in the spin correlation function is illustrated in Fig. 4.1, according to the work of Halperin and Hohenberg [15, 17]. In the (q, κ) -plane, three regions can be distinguished, in which the spin correlation function has different asymptotic behaviours. The shaded region (I), where $x = \kappa/q \gg 1$ and $T < T_C$, corresponds to the situation where the wavelength of the spin fluctuations λ is much larger than the correlation length ξ of the spins. This latter region is called hydrodynamic, since the dynamics of the system can be described by macroscopic equation of motion for spin densities. Similarly, the region (III) is related to a macroscopic regime, but in the paramagnetic phase.

The region (II), on the other hand, corresponds to the case of phenomena occurring on a small scale when compared to ξ (with $x = \kappa_{\pm}/q \ll 1$) and the hydrodynamic description of the system is not valid anymore. The values of the spin correlation functions for the different regions are assumed to merge at the lines $\kappa_{\pm} = \pm q$, which give the separation between the hydrodynamic and the critical regime.

In an isotropic ferromagnet, the Hamiltonian is invariant under rotation. A spontaneous symmetry breaking appears in the ordered phase, as the magnetisation generates a preferred direction. Moreover, it can be shown that an infinitesimal rotation of the magnetisation vector costs no energy. This physical effect is responsible for the divergence of the transverse susceptibility at any temperature below T_C [18]. However, in the mean field approximation the longitudinal susceptibility does not diverge for small q -values below T_C .

Beyond mean field approximation, the spin dynamics of an isotropic ferromagnet can be modeled within the framework of mode coupling theory. It has been shown that the transverse modes influence the longitudinal susceptibility [19]. $\chi_{\parallel}(\mathbf{q})$ is modified as follows:

$$\begin{aligned} \chi_{\parallel}^{-1}(\mathbf{q}) &= 1 + \frac{29x^2}{18 + 4x} - \frac{9x^2}{11} \\ &\times \left[1 + \sqrt{1 + 4x^2} \ln \left(\frac{\sqrt{1 + 4x^2} - 1}{2x} \right) \right] + \dots \end{aligned} \quad (4.16)$$

This latter expression can be simplified for the two asymptotic regimes. In the critical region, one obtains the Lorentzian behaviour from Eq. 4.13 but in the hydrodynamic regime the parallel susceptibility takes the following form:

$$\chi_{\parallel}(\mathbf{q}) \propto 1/(q\kappa_-) \quad \text{for } x \gg 1 \quad (4.17)$$

The longitudinal susceptibility is therefore predicted to diverge at any temperature below T_C in the limit $q \rightarrow 0$.

So far the crossover between the two regimes could not be observed experimentally, since the x -range needed is rather difficult to achieve.

4.3 Dynamic Properties

4.3.1 Scaling theory

Similarly to the static case, the dynamical scaling hypothesis states that the spin fluctuations at any temperature are related to the fluctuations at T_C via the scaling relation:

$$\omega_c(\mathbf{q}, \xi) = Aq^z f_i(x) \quad (4.18)$$

where A is a non-universal scaling parameter, the subscript i stands for the type of fluctuation that is considered, and z is the dynamical critical exponent ($z =$

$\frac{1}{2}(d+2-\eta) \approx 2.5$, for $d=3$). The characteristic frequency of the system, $\omega_c(\mathbf{q}, \xi)$, is defined via the spectral weight function of the fluctuations $F(\mathbf{q}, \omega)$:

$$\int_{-\infty}^{+\infty} F(\mathbf{q}, \omega) d\omega = 2 \int_{-\omega_c}^{+\omega_c} F(\mathbf{q}, \omega) d\omega \quad (4.19)$$

The dynamical scaling functions $f_i(x)$ are homogeneous functions of $x = \kappa/q$, and have the following asymptotic behaviours:

$$\begin{aligned} f(x) &\rightarrow 1, & \text{when } x \rightarrow 0; \\ f(x) &\propto x^{1/2}, & \text{when } x \rightarrow \infty. \end{aligned} \quad (4.20)$$

The scaling function $f(x)$ has been calculated numerically by Résibois and Piette [20]. The results show that $f(x)$ has a minimum for $x \simeq 1$, which is consistent with neutron experiments performed on Fe, Co and Ni. This feature can be interpreted as follows. The dynamical scaling function represents the ratio of the linewidth at any temperature divided by the linewidth at T_C . Therefore in the critical regime, typically when $x < 4.5$, the lifetime of the spin fluctuations is larger than the one at T_C , whereas the opposite occurs in the hydrodynamic regime.

4.3.2 Dipolar interactions

According to the scaling hypothesis, the critical region is approached for $q \rightarrow 0$ and $E \rightarrow 0$. Because the dipolar forces are long range, they are expected to be of primary importance in the critical properties of the magnetic systems. Aharony and Fisher have shown by means of renormalisation group calculations that dipolar interactions modify the critical exponents [21] (see Table 4.1).

The introduction of dipolar interaction between magnetic moments leads to consider an additional length scale in the system q_D^{-1} , where q_D is the dipolar wave vector defined as follows:

$$g\mu_B\mu_0 M(T, H) = Dq_D^2 \quad (4.21)$$

The left side of Eq. 4.21 corresponds to the dipolar energy of the system that is equated to the spin-wave energy with $q = q_D$. Above T_C , the dipolar wave vector q_d is linked with the inverse correlation length κ_+ via the bulk static susceptibility $\chi(q=0, T)$:

$$q_d^2 = \kappa_+^2 \chi(0, T) \quad (4.22)$$

In addition to x , a second scaling variable $y = q_D/q$ is introduced, which delimits the boundary between the dipolar regime ($q_D \gg q$) and the isotropic regime ($q_D \ll q$). In an ordered system, the introduction of dipolar forces in the Hamiltonian leads to an anisotropy that lifts the degeneracy of the two transverse modes. The susceptibility depends therefore not only on the direction of the magnetisation but also on the relative orientation of the reduced momentum transfer \mathbf{q} to \mathbf{M} .

The critical dynamics of dipolar magnets can be derived from mode coupling theory [22, 23]. In this latter model, the scaling variables ($x = \kappa/q$ and $y = q_D/q$) are introduced.

The static susceptibilities for each mode are given via the eigenvalues l_i and the eigenvectors \mathbf{v}_i of the static susceptibility tensor $\chi(\mathbf{q})$:

$$\chi(\mathbf{q})\mathbf{v}_i = \frac{1}{2Jq^2l_i}\mathbf{v}_i \quad (4.23)$$

where

$$l_1(R, \phi, \vartheta) = 1 \quad \text{and} \quad l_{2/3}(R, \phi, \vartheta) = 1 + R^2 \hat{F}_{-/ +}(\phi, \vartheta) \quad (4.24)$$

and

$$\hat{F}_{\pm}(\phi, \vartheta) = \frac{1}{2} \{1 \pm \sqrt{1 - \sin^2(2\phi) \cos^2 \vartheta}\} \quad (4.25)$$

$$R = \sqrt{\hat{r}^2(x, y) + y^2}, \quad \tan \phi = \frac{y}{\hat{r}^2(x, y)} \quad (4.26)$$

ϑ is the angle between \mathbf{q} and the plane perpendicular to the magnetisation \mathbf{M} . Finally, $\hat{r}(x, y)$ is expressed as follows:

$$\begin{aligned} \hat{r}^2(x, y) &= \frac{29x^2}{18 + 2x[1 + (1 + y^2)^{-1/2}]} - \frac{9x^2}{11} \\ &\times \left[1 + \sqrt{1 + 4x^2} \ln \left(\frac{\sqrt{1 + 4x^2} - 1}{2x} \right) \right] + \dots \end{aligned} \quad (4.27)$$

This latter expression is related to the longitudinal susceptibility $\chi_{||}(\mathbf{q})$ in the isotropic case ($y = 0$) (see Eq. 4.16). Figure 4.2 presents a schematic view of a scattering process in the dipolar case. The eigenvectors of $\chi(\mathbf{q})$ are also shown. The vector \mathbf{v}_1 is perpendicular to the plane defined by \mathbf{M} and \mathbf{q} , and its eigenvalue is not affected by the dipolar forces.

The rotation of the eigenvectors \mathbf{v}_2 and \mathbf{v}_3 , with respect to \mathbf{M} , represented by φ_3 , is an effect of the dipolar interactions:

$$\varphi_3 = \frac{1}{2} \arccos f(\vartheta, R, \phi) \in [0, \pi/2] \quad (4.28)$$

$$f(\vartheta, R, \phi) = \frac{\sin^2(2\phi) \cos(2\vartheta) - \cos^2 \phi}{\sqrt{1 - \sin^2(2\phi) \cos^2 \vartheta}} \quad (4.29)$$

One can observe in Eq. 4.29 that in absence of dipolar forces ($y = 0 \iff \tan \phi = 0$) the rotation of the $(\mathbf{v}_2, \mathbf{v}_3)$ -plane does not occur, namely $\varphi_3 = \pi/2$.

The spin fluctuations are also influenced by the dipolar interactions, via the dynamical scaling functions which are no longer isotropic, but depend on the dipolar angle ϑ (See Ref. [24] for comprehensive description of the different regimes of the dynamical susceptibility).

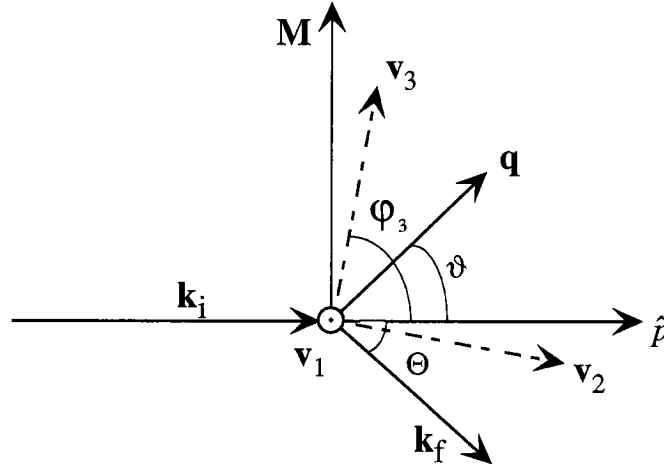


Figure 4.2: Scattering layout for a single domain ferromagnet with magnetisation \mathbf{M} . $\hat{\mathbf{p}}$ is the projection of the scattering vector, $\mathbf{q} = \mathbf{k}_i - \mathbf{k}_f$, onto the plane perpendicular to \mathbf{M} , thus defining the angle ϑ . The \mathbf{v}_i are the eigenvectors of the static susceptibility tensor $\chi(\mathbf{q})$. Θ is the scattering angle, φ_3 the rotation angle due to dipolar effects. \mathbf{v}_1 is perpendicular to the plane, all other vectors lie in the plane defined by \mathbf{M} and \mathbf{q} .

To summarise, the introduction of dipolar forces in the Heisenberg Hamiltonian leads to the following consequences: First of all, the dipolar anisotropy generates a complicated tensorial structure for the dynamical susceptibility. The scaling functions thus depend on the relative orientation of \mathbf{q} with respect to \mathbf{M} . Secondly, the transverse scaling function may exhibit a minimum in the dipolar case, whereas it is monotonically decreasing in the isotropic case. It can be shown that in the case of dipolar interactions the magnetisation is no longer conserved, and therefore the damping of the fluctuations can be increased for large x -values, namely when the wavelength of the fluctuations is larger than the spin correlation length and the long range interaction begins to influence the lifetime.

4.3.3 Spin dynamics

In a magnetically ordered system two types of modes contribute to the magnetic excitation spectrum: the fluctuations along, $\delta\mathbf{S}_{\parallel}(\mathbf{q}, \omega)$, and transverse, $\delta\mathbf{S}_{\perp}(\mathbf{q}, \omega)$, to the magnetisation direction. $\delta\mathbf{S}_{\parallel}(\mathbf{q}, \omega)$ is quasielastic and its static susceptibility is given by Eq. 4.16. The two $\delta\mathbf{S}_{\perp}(\mathbf{q}, \omega)$ modes (called spin-wave modes) are dispersive, and in the isotropic case their susceptibility is degenerate (see Eq. 4.12).

If dipolar forces are included in the model, the spin-wave dispersion near the magnetic zone center can be expressed as follows:

$$\hbar\omega = \left[(Dq^2 + g\mu_B\mu_0 H_{eff})(Dq^2 + g\mu_B\mu_0 H_{eff} + Dq_D^2 \cos^2 \vartheta) \right]^{1/2} \quad (4.30)$$

where D is the spin-wave stiffness, $H_{eff} = H_{ext} - N \cdot M$ the effective field in the sample, H_{ext} the external applied field, N the demagnetisation factor and ϑ the angle between \mathbf{q} and the plane perpendicular to \mathbf{M} (see Fig. 4.2). This general

result has been obtained in the forties by Holstein and Primakoff [25], who studied the dynamics of ferromagnets by means of linear spin-wave theory. The dispersion at small q for an isotropic magnet is simply deduced from Eq. 4.30 if one sets q_D to 0.

The term $Dq_D^2 \cos^2 \vartheta$ represents the dipolar pseudo-gap that can be observed if the scattering vector is not parallel to the magnetisation. It reaches its maximum for $q \parallel \mathbf{M}$.

4.4 Theory of itinerant magnetism

The transition elements exhibit magnetic properties that cannot be explained by a Heisenberg model based on magnetic moments that are located at the sites of a lattice. Many unusual features are indeed observed experimentally: the saturation moment per atom is a non integral number of a Bohr magneton (Ni: $p_s = 0.6 \mu_B$, Co: $p_s = 1.7 \mu_B$, Fe: $p_s = 2.22 \mu_B$); the Curie constant derived from magnetic susceptibility data does not give half-integral values of the quantum number S , and there is no correlation between the paramagnetic moment and the saturation moment in the ordered phase. Finally, the magnetic entropy \mathcal{S}_m does not follow the Heisenberg model: $\mathcal{S}_m = k \ln(2S + 1)$.

Weakly ferromagnetic metals turn out to be a special case of such magnets. They are characterised by a small saturated magnetic moment and a low Curie temperature. However, the susceptibility follows the Curie-Weiss law in the paramagnetic phase, as it is the case for a system of localised spins.

4.4.1 Stoner theory

The electrons responsible for the magnetism of the $3d$ metals are situated in the incomplete d -shells of the atoms. The physical properties of such elements can be described on the basis of a band model.

In the thirties, Stoner has developed a first theory for itinerant magnets, by considering a gas of interacting electrons, and using a single band model within a Hartree-Fock approximation [26]. The Hamiltonian of the system, similar to a Hubbard Hamiltonian, is consequently given by:

$$\mathcal{H} = \sum_k \sum_\sigma \epsilon(\mathbf{k}) a_{k\sigma}^\dagger a_{k\sigma} + \frac{U}{N} \sum_q \sum_k \sum_{k'} a_{k+q\uparrow}^\dagger a_{k'-q\downarrow}^\dagger a_{k'\downarrow} a_{k\uparrow} \quad (4.31)$$

where N is the total number of spins, U the exchange interaction between electrons, \mathbf{k} the wave vector of the electron, σ the spin state (\uparrow or \downarrow), $a_{k\sigma}^\dagger$ and $a_{k\sigma}$ the creation and annihilation operators of an electron in the quantum state $|k\sigma\rangle$, respectively. On a thermodynamic point of view, the Hartree-Fock free energy is given by:

$$F_{HF}(M, T) = F_0(M, T) - IM^2 - hM \quad (4.32)$$

where $F_0(M, T)$ stands for the non interacting system, IM^2 results from the interaction between electrons, and the third term is the Zeeman energy coming from an external applied field h . The condition of thermal equilibrium for the free energy leads to the following magnetic equation of state:

$$\partial F_{HF}(M, T)/\partial M = \partial F_0(M, T)/\partial M - 2IM - h = 0 \quad (4.33)$$

The magnetic susceptibility of the interacting system can be obtained by determining the total magnetisation of the system and using Eq. 4.4:

$$\chi_{Stoner} = \frac{g^2 \mu_B^2}{2} \rho(\epsilon_F) \frac{1}{1 - U\rho(\epsilon_F)} \quad (4.34)$$

$\rho(\epsilon_F)$ is the electron density of states at the Fermi energy and $g^2 \mu_B^2 \rho(\epsilon_F)/2$ is the Pauli paramagnetic susceptibility. The magnetic susceptibility of an interacting system is enhanced by the Stoner factor $1/[1 - U\rho(\epsilon_F)]$ when compared with the free electron susceptibility. This factor is also related to the criteria for having a ferromagnetic stability: $\alpha_0 = U\rho(\epsilon_F) > 1$.

The Stoner approach is however restricted to the very low temperature regime, where the spin fluctuations can be neglected. Indeed, the temperature dependence of the magnetisation is expressed as follows:

$$M(T) = M(0)(1 - (T/T_C)^2)^{1/2} \quad (4.35)$$

This formula is observed to fit the actual behaviour of itinerant magnets only near $T = 0$. The effect of spin-waves and critical fluctuations is expected to modify significantly the magnetic equation of state at finite temperatures. In addition, the Stoner model does not predict a T-dependence for $\chi(T)$ that is in accordance with the experimental Curie-Weiss law. The Hartree-Fock result provides indeed a quadratic temperature dependence for the magnetic susceptibility:

$$1/\chi(T) \simeq \frac{\pi^2}{3\alpha_0} IR(T^2 - T_C^2), \quad (4.36)$$

where R is a function of the derivatives of the electron density of states at the Fermi level.

Finally, the Stoner approach predicts a critical temperature T_C that can be one order of magnitude larger than the experimental one. Some modifications are therefore necessary to overcome these failures, and it will be discussed in the next two paragraphs.

4.4.2 Mean field RPA

The dynamical susceptibility of an itinerant spin system can be calculated via the Heisenberg equation of motion for spin densities, that are solved within a random phase approximation (RPA).

At finite temperature two main contributions are expected to occur. On the one hand, the theory predicts single particle spin-flip excitations, the so-called Stoner excitations that build a continuous spectrum. In addition, the existence of collective spin excitations (spin-waves) is predicted at long wavelengths. These do not extend to the zone boundary since for high q -values the energy of the spin-waves would exceed the energy for the creation of a spin-flip excitation. Therefore the spin-waves merge into the Stoner continuum at a q -value that is smaller than q_{ZB} .

As a starting point for RPA calculations, the Heisenberg equation of motion for non interacting spins provides the following magnetic susceptibility [4]:

$$\chi_{\Delta 0}^{+-}(q, \omega) = \sum_k \frac{f(\epsilon_{k+q} - \Delta) - f(\epsilon_k + \Delta)}{\epsilon_k - \epsilon_{k+q} + 2\Delta - \omega} \quad (4.37)$$

2Δ is the energy gap between the spin-up and spin-down electron band and $f(\epsilon)$ the Fermi-Dirac distribution function.

The standard RPA approximation, introducing an effective interaction $I = U/N$ between the electrons delivers the following modification:

$$\chi_{RPA}^{+-}(q, \omega) = \frac{\chi_{\Delta 0}^{+-}(q, \omega)}{1 - I\chi_{\Delta 0}^{+-}(q, \omega)} \quad (4.38)$$

The mean field RPA model is a step forward in the description of itinerant magnets. However the inconsistencies between theoretical predictions and the actual physical behaviour are still not resolved. As an example the behaviour at finite temperature still deviates significantly from experiment.

4.4.3 SCR-RPA

In the seventies, Moriya and Kawabata postulated that the inconsistencies presented in the two preceding paragraphs can be explained by the fact that the RPA dynamical susceptibility does not agree with the one calculated from the renormalised free energy [27]. ‘‘Renormalised’’ means that the free energy is determined with inclusion of spin fluctuations. They have therefore proposed a self-consistent renormalisation theory (SCR) based on the following statement: $\chi(q, \omega)$ and F must be calculated at the same time, so that the static as well as long wavelength limit of the dynamical susceptibility agrees with that calculated from the renormalised free energy, in accordance with Eq. 4.4 [4].

An additional term to the Hartree-Fock free energy is therefore introduced, $\Delta F(M, T)$, that accounts for the thermally excited spin fluctuations (see Eq. 4.39). The SCR magnetic equation of state is hence obtained by minimising the free energy with respect to the applied field (Eq. 4.40).

$$F_{SCR}(M, T) = F_{HF}(M, T) + \Delta F(M, T) \quad (4.39)$$

$$\partial F_{SCR}(M, T)/\partial M = \partial F_{HF}(M, T)/\partial M + \partial \Delta F(M, T)/\partial M = 0 \quad (4.40)$$

The RPA dynamical susceptibility is accordingly modified as follows:

$$\chi_{MI}^{+-}(q, \omega) = \frac{\chi_{M0}^{+-}(q, \omega)}{1 - I\chi_{M0}^{+-}(q, \omega) + \lambda_{MI}(q, \omega)} \quad (4.41)$$

The additional term $\lambda_{MI}(q, \omega)$ is then determined by means of the magnetic equation of state for the free energy (Eq. 4.40), via the condition given by Eq. 4.4.

The effects of the SCR model are seen to be very fruitful. The calculated T_C is closer to the experimentally determined ordering temperature and generally much lower than the Stoner value. On the other hand, the temperature dependence of the magnetisation below T_C is now modified as follows:

$$M(T) = M(0)(1 - (T/T_C)^{4/3})^{1/2} \quad (4.42)$$

Finally, the magnetic susceptibility above T_C follows a CW law. However this feature has to be named a “new CW law” because the physics underlying this feature is different from the law derived for local moments. In contrast to localised systems where the magnetic moment per ion is constant, the mean square local spin amplitude $\langle S_L^2 \rangle$ is temperature dependent for itinerant magnets. Figure 4.3 shows the comparison between localised systems and weakly ferromagnetic metals. For the localised moment case, the magnetic moment is always constant. For the itinerant electron case, $\langle S_L^2 \rangle$ follows the T dependence of the magnetisation in the ordered phase (see Eq. 4.42); at T_C it reaches its minimum (non-zero) of $3/5$ of the saturation value; above T_C , it then increases linearly with temperature, because of the thermally excited spin fluctuations. As a consequence, the paramagnetic susceptibility which is proportional to $1/T^2$ in the HF-RPA model is now modified by the linear term given by the magnetic moment.

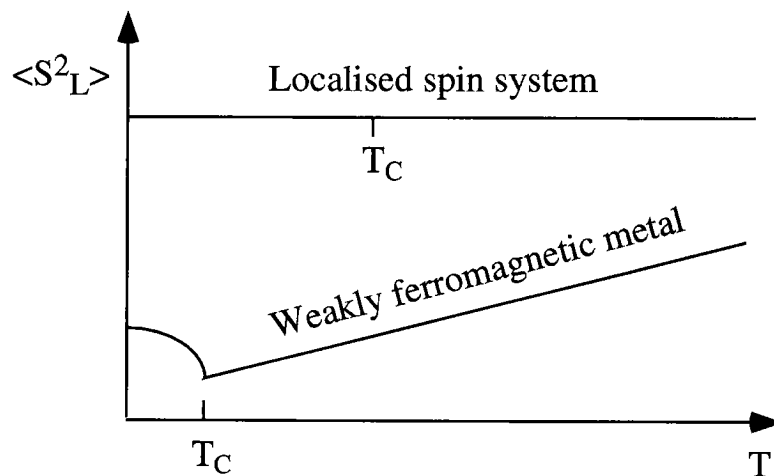


Figure 4.3: Comparison for the temperature dependence of the mean square amplitude of the spin density $\langle S_L^2 \rangle$ for a localised spin system and for an itinerant weak ferromagnet [after Ref. [4]].

As a next step, we mention the phenomenological approach by Lonzarich and Taillefer [28], which is closely connected to the SCR-RPA theory. The main difference

is that the longitudinal spin fluctuations are also taken into account in the theory, which is based on a self-consistent Ginzburg-Landau model.

The magnetic equation of state is again an extension of Stoner's theory, with correcting terms arising from the enhanced magnetic fluctuations of long wavelength and low frequencies. In the paramagnetic state the calculated dynamical susceptibility is given by:

$$\chi^{-1}(q, \omega) = \chi^{-1}(q)[1 - i\omega/\Gamma(q)] \quad (4.43)$$

$$\chi^{-1}(q) = \chi^{-1} + cq^2 + \dots \quad (4.44)$$

$$\Gamma(q) = \gamma q \chi^{-1}(q) \quad (4.45)$$

The parameters γ and c can be derived from the band structure, and compared with the results of neutron scattering. In the ferromagnetic phase, the model is an extension from the latter case:

$$\chi_\nu^{-1}(q, \omega) = \chi_\nu^{-1}(q)[1 - i\omega/\Gamma_\nu(q)] \quad (4.46)$$

$$\chi_\nu^{-1}(q) = \chi_\nu^{-1} + c_\nu q^2 + \dots \quad (4.47)$$

$$\Gamma_\nu(q) = \gamma_\nu q \chi_\nu^{-1}(q) \quad (4.48)$$

Where the subscript ν accounts for the fluctuations transverse \perp and longitudinal \parallel to the magnetisation. For small magnetisation and fluctuations, the parameters c_ν and γ_ν are presumed to be independent of ν and to merge with the ones of the paramagnetic phase.

At long wavelengths, the spin-waves are expected to occur at finite energy transfer with a dispersion proportional to the magnetisation M :

$$E_q = g\mu_B M \chi_\perp^{-1}(q) = g\mu_B M (\chi_\perp^{-1} + c_\perp q^2 + \dots). \quad (4.49)$$

No scaling theory is explicitly mentioned in the theory of itinerant magnets. However, the ratio $\Gamma(T)/\Gamma(T_C)$ from Eq. 4.48 and Eq. 4.45 for $T=T_C$ provides the scaling function

$$f_{SRC} = \frac{q(\chi^{-1} + q^2)}{q^3}. \quad (4.50)$$

that can be considered as the itinerant version of Eq. 4.18.

Chapter 5

Itinerant Spin Systems

The great tragedy of science, the slaying of a beautiful theory by an ugly fact.
Thomas Henry Huxley

5.1 Ni₃Al

5.1.1 Introduction

Many materials showing interesting physical behaviour like heavy fermion, non-Fermi liquid and lamellar CuO systems, are metals close to a magnetic instability. Magnetic excitations are therefore believed to play an important role in the physics of such materials. Recently, Moriya and Takimoto developed a phenomenological theory for modeling the spin fluctuations in strongly correlated electron systems [40]. They have shown that the dynamical susceptibility takes a form similar to the one of weak itinerant magnets. These latter systems can therefore be used as model systems for understanding the magnetism in heavy electron systems.

Ni₃Al is known as the paradigm of a weak itinerant ferromagnet. The saturation moment per magnetic atom p_s is $0.07 \mu_B$ and the Curie temperature $T_C = 41\text{K}$. In contrast, the effective moment $p_{\text{eff}} = 0.63 \mu_B$, as obtained from paramagnetic susceptibility data, is much larger. The theory presented in Section 4.4 for itinerant spin systems is able to predict values for T_C and for the ratio p_{eff}/p_s of the moments above and below T_C that are in good agreement with experiments on this compound, as well as for MnSi, another well-known itinerant system. In addition, the predicted quadratic q -dependence of the spin wave dispersion has been confirmed in experiments [29, 30, 31].

As shown in Chapter 4, the prediction for the q -dependence of the linewidth of the magnetic fluctuations is markedly different for localised spin systems when compared with a localised ferromagnet. From the itinerant theory, the linewidth given by Eq. 4.48 can be rewritten as follows:

$$\Gamma_{wi} = A_{wi}q(q^2 + (\kappa^\pm)^2) = A_{wi}q^3(1 + (\kappa^\pm/q)^2) \quad (5.1)$$

whereas according to scaling theory, the linewidth for localised spins is given by:

$$\Gamma_{loc} = A_{loc} f_{\Gamma}(\kappa^{\pm}/q) q^{2.5}, \quad (5.2)$$

where f_{Γ} is a dynamical scaling function (see Eq. 4.18). The latter expression has been confirmed for $T \geq T_C$ by Ishikawa et al. in weak itinerant MnSi that exhibits below T_C a helical structure [29]. More recent experiments on polycrystalline Ni₃Al by Bernhoeft et al. [30, 31] also indicate the validity of Γ_{wi} .

The critical fluctuations are not taken into account in the theory for weak-itinerant magnets. Nevertheless, in contrast to a localised magnet, where the magnetic moments are confined to single atoms, the magnetic moments in itinerant magnets are defined over large assemblies of atoms that are correlated over a distance $\xi_c \gg a$, where a is the lattice parameter. As soon as the correlation length of the magnetic fluctuations ξ^{\pm} and the wavelength of the spin fluctuations $\Lambda = 2\pi/q$ exceed ξ_c one may argue that one should observe critical fluctuations similarly as in true local moment systems.

In order to test the existence of critical fluctuations we have determined the q -dependence of the quasielastic fluctuations at T_C in Ni₃Al. In addition, we have measured the temperature dependence of the linewidth of the spin waves below T_C and compared them with the predictions of a very recent mode-mode coupling theory [22, 24, 23]. We have also studied the temperature dependence of the paramagnetic excitations, which was found to be in agreement with the scaling function predicted for itinerant systems above T_C [28]. The results show that Ni₃Al is one of the most ideal and clean systems to prove the dynamical scaling behaviour in an isotropic ferromagnet below T_C .

5.1.2 Experimental procedure

The inelastic neutron scattering experiments have been performed on a cylindrical Ni_{0.75+x}Al_{0.25-x} single crystal with a diameter of 16 mm and a length of 60 mm, enriched with Ni ($x=1\%$) [32]. The enrichment has no influence on the fcc structure of the sample, however, it leads to an enhancement of the magnetic moment and to a larger T_C thus facilitating the experiment. Magnetisation measurements performed at pieces taken from the top and the bottom of the single crystal yielded consistent values $T_C = 72.5 \pm 0.5$ K in excellent agreement with values reported in Ref. [33] for a sample with 1% enrichment. More evidence for the high quality of the sample will be given below.

The experiments have been carried out on the cold neutron three-axis spectrometers FLEX at the HMI in Berlin, and TASP at the Swiss spallation source SINQ. The same experimental setup has been used for both experiments. The final energy was fixed at $E_f = 2.5, 3.0$ and 4.5 meV and tight collimations (guide-20'-20'-40') were used, leading to a resolution of 0.03, 0.04 and 0.09 meV, respectively. A cold Be-filter was placed in the incident beam to remove higher order neutrons. The background was measured at $T = 1.5$ K for all configurations and subtracted from the data. As in this work we were primarily interested in spin wave excitations,

the forward scattering technique was chosen for convenience, thus avoiding phonon contributions.

The data has been fitted with a scattering function for damped spin waves:

$$S(q, E) = \frac{E}{1 - e^{-\beta E}} \frac{N}{q^2} \frac{1}{2\pi} \left[\frac{\Gamma}{(E + E_q)^2 + \Gamma^2} + \frac{\Gamma}{(E - E_q)^2 + \Gamma^2} \right], \quad (5.3)$$

and the deconvolution with respect to the resolution of the spectrometer was performed. In Eq. (5.3) N is a normalisation constant, $E_q = D(T)q^2$ is the dispersion and Γ is the relaxation frequency (linewidth) of the magnetic excitations. The quantity N/q^2 is proportional to the static susceptibility $\chi_{\perp}(q)$. To fit the data at T_C , the spin wave energy E_q was set to zero.

We have used an iterative process to obtain the parameters N , D and Γ from the inelastic scans. In a first step all parameters were free. In a second step we fixed D for each T at an averaged value. Finally, the linewidth was fixed too and N was determined. This procedure reduced correlation effects between E_q , $\Gamma(q)$ and $\chi_{\perp}(0)$ considerably.

In order to determine which model best describes the collective excitations in Ni₃Al, we have systematically analysed the data using itinerant [28] and localised theory [24, 23], respectively, i.e. we assumed that the q -dependence of Γ is given by Eqs. 5.1 and 5.2, respectively.

5.1.3 Experimental results

Some typical results of inelastic scans after subtraction of the background measured at $T = 1.5$ K are shown in Fig. 5.1. The error bars around $E = 0$ meV are large due to the important incoherent scattering of Ni. The renormalisation of the spin waves with increasing temperature is clearly visible. The tails of the spectra cannot be measured because the scattering triangle does not close at high energy transfers anymore.

For each T the measured spin wave dispersion was fitted with the quadratic expression $E_q = \Delta + Dq^2$. The fits show that the energy gap Δ is vanishingly small at all T . The T -dependence of D is plotted in Fig. 5.2 and shows clearly the renormalisation of the spin waves close to T_C .

According to the itinerant model, the spin waves are expected to occur at finite energy transfer with a dispersion proportional to the magnetisation M :

$$E_q = g\mu_B M \chi_{\perp}^{-1}(q) = g\mu_B M (\chi_{\perp}^{-1} + c_{\perp} q^2 + \dots) \quad (5.4)$$

The spectroscopic splitting factor g is close to 2 in Ni₃Al. As shown in Section 4.4.3, M is predicted to behave according to:

$$M(T, 0)/M_0 = (1 - (T/T_c)^{\epsilon})^{1/2}, \quad (5.5)$$

where ϵ is equal to 2 in the Stoner model and 4/3 in the SCR theory [28].

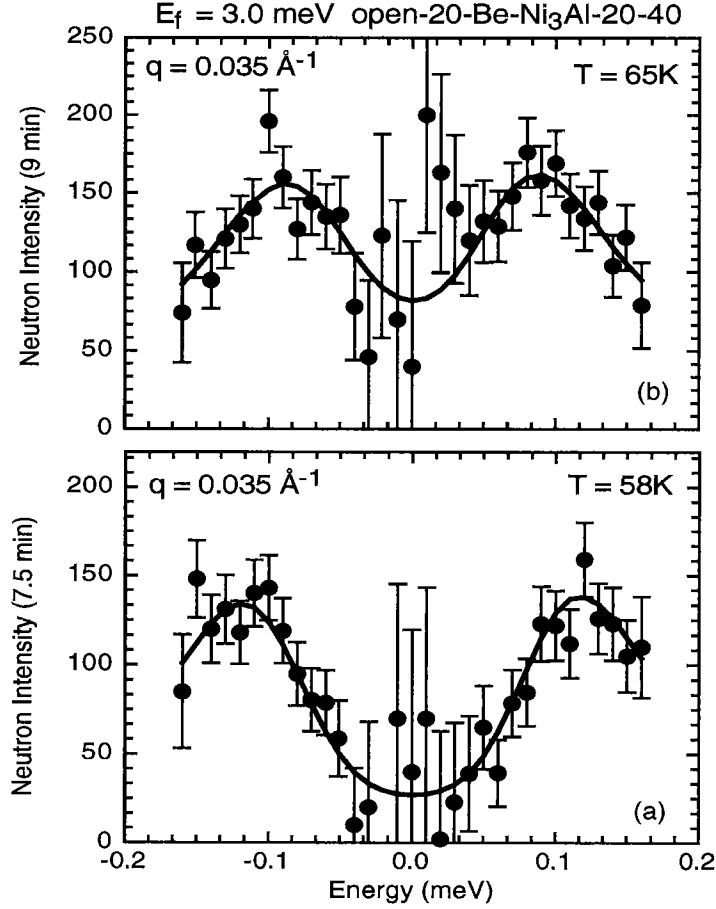


Figure 5.1: Inelastic scans at $q=0.035 \text{ \AA}^{-1}$ for $T=0.8$ and $0.9 T_C$. The solid lines are fits to the model given by Eq. (5.3) convoluted with the experimental resolution function.

In contrast, the spin wave dispersion for a Heisenberg ferromagnet is given for $T \rightarrow T_C$ by:

$$E_q = D(T)q^2 = D_0|\tau|^{0.36}q^2, \quad (5.6)$$

where $\tau = 1 - T/T_C$.

The temperature dependence of the spin-wave stiffness D has been fitted using the itinerant (see Eq. (5.5)) and the localised model (see Eq. (5.6)). If the ordering temperature is fixed at $T_C = 72.5 \text{ K}$, as obtained from the magnetisation measurements, the exponent ϵ of the itinerant model differs from the $\epsilon = 4/3$ value (see dashed curve in Fig. 5.2). On the contrary, fixing ϵ at the predicted value gives a slightly higher value for the transition temperature ($74 \pm 0.4 \text{ K}$). This discrepancy between the experimental and the theoretical T_C is of the same order of the one observed for polycrystalline samples [34]. On the other hand, the fit with the Heisenberg model gives an exponent of 0.34 ± 0.03 , close to the theoretically expected $0.36(5)$ value, and is much less sensitive to T_C (solid curve in Fig. 5.2). As a comparison, the ratio of $D(0.8T_C)$ for our sample and D_p for the polycrystalline reference of pure Ni₃Al [31]

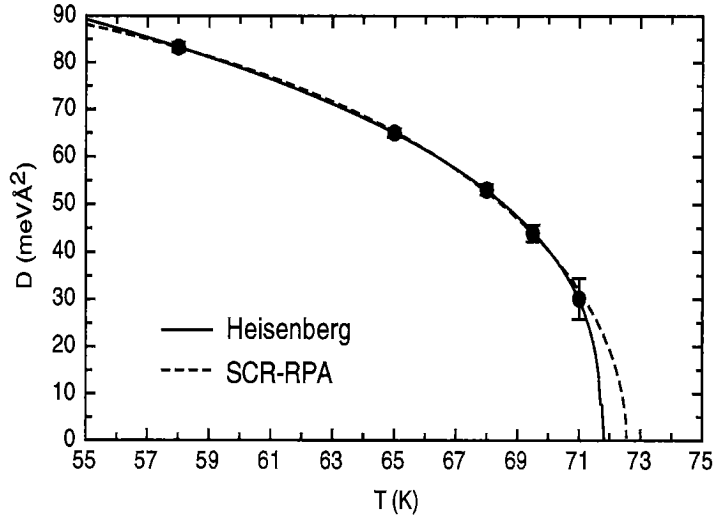


Figure 5.2: Spin-wave stiffness as a function of temperature, the solid line is related to the Heisenberg model, and the dashed line to the itinerant model.

gives $D/D_p = 1.38 \pm 0.08$, a value that shows reasonable agreement with the ratio of the magnetic moments measured in both kind of samples [33] ($D/D_p = 1.65$).

In Eq. 5.4 $\chi_{\perp} = \chi_{\perp}(q = 0)$ is the static transverse susceptibility that is infinite if there is no anisotropy. Our results show that $\chi_{\perp}(q = 0) = \infty$ within the accuracy of the neutron measurements. This behaviour is actually expected, since the spin waves are Goldstone modes, irrespective of the degree of localisation of the spins.

The static susceptibility $\chi_{\perp}(q)$ resulting from the integration of the inelastic signal over energy was extracted from the data. Fig. 5.3 shows $\chi_{\perp}^{-1}(q)$ versus q^2 . The linear relationship is in agreement with the expected $1/q^2$ divergence for spin waves. Within the experimental accuracy the inverse correlation length for the spin waves $\kappa_{\perp} = 0.016 \pm 0.017 \text{ \AA}^{-1}$ (not to be confused with κ_0^-) is zero, in agreement with the observation that the spin waves have no gap. In addition, the slope of $\chi_{\perp}(q)$ shows a slight T -dependence, which is connected to the fact that $\chi(T)_{q=0}$ increases by approaching T_C .

The linewidth of the spin waves is plotted in Fig. 5.4 and compared with SCR theory (a) (fit parameters A_{wi} and κ^-) and scaling theory based on the Heisenberg model (b) (fit parameters A_{loc} and z). The comparison shows that both models provide good parametrisations of the data. The inset shows that the critical exponent z is close to the value 2.5 that has been predicted theoretically and measured in many ferromagnetic systems (see Ref. [23] for a summary). We point out that this behaviour occurs over a large T -range.

In order to provide a direct comparison of the spin fluctuations in Ni₃Al with scaling theory we have measured the linewidth of the paramagnetic fluctuations at T_C (see Fig. 5.5). The solid line is a fit to the data using the expression $\Gamma = Aq^z$ yielding $z = 2.47 \pm 0.16$ that is compatible with the dynamical scaling prediction $z = 2.5$ at $T = T_C$. In contrast, the RPA expression $\Gamma = A_{wi}q^3$ does not reproduce the data

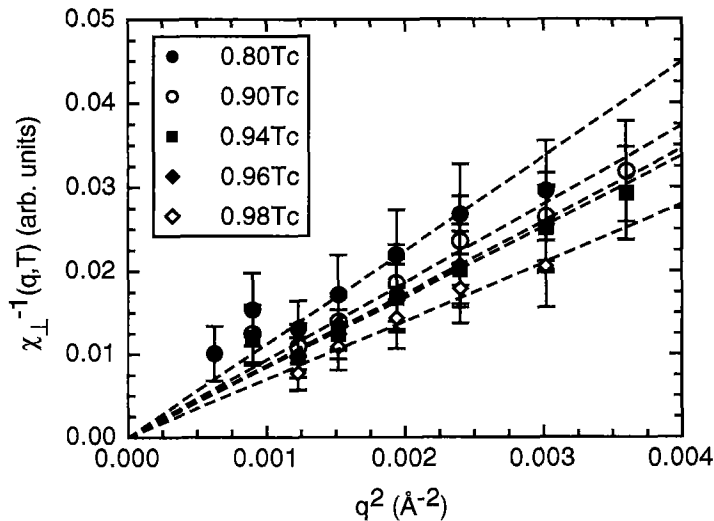


Figure 5.3: The inverse of the static susceptibility of the spin waves, $\chi_{\perp}^{-1}(q)$, as a function of q^2 . The dashed lines are fits to the data using a Lorentzian q -dependence: $\chi(q)_{\perp}^{-1} \propto (\kappa_{\perp}^2 + q^2)$, where the parameter κ_{\perp} is set to zero.

well.

In a second step we divided for each temperature the resolution corrected linewidth $\Gamma(T)$ by $\Gamma(T = T_C)$ (measured values) in order to determine $f_{\Gamma}(\kappa^-/q)$ (see Eq. 5.2). The scaling function is plotted in Fig. 5.6 versus the scaling variable $x = \kappa^-/q$. As the inverse correlation length κ^- is not known below T_C we have adjusted the scale of the x -axis such that the data points agree with the theoretical curve of mode-mode coupling theory (MMT) of Ref. [24]. The comparison yields $\kappa_0^- = 0.10 \pm 0.04 \text{ \AA}^{-1}$.

Finally, we have analysed the scaling behaviour of the magnetic excitations above T_C , as shown in Fig. 5.7. The scaling variable $x = \kappa^+/q$ has been determined as follows. According to scaling laws from mode-coupling theory in the critical regime, the ratio for the inverse correlation length below and above T_C is given by $\kappa^-/\kappa^+ = 2.02$. We have therefore used the experimental value κ_0^- determined with the scaling of the spin waves, that yielded $\kappa_0^+ = 0.049 \pm 0.019 \text{ \AA}^{-1}$. Since the paramagnetic signal has to be recovered by background subtraction from the top of a large incoherent signal, more experimental time is required for obtaining the same statistics as in the ordered phase, where the magnetic excitations are dispersive. Therefore we could not gather so many datapoints as for the ferromagnetic case in a reasonable time. Nevertheless, the experimental scaling function above T_C provides sufficient information for allowing us to compare it with theoretical predictions. We have plotted in Fig. 5.7 the Résibois-Piette function [20], which results from MMT calculations for a Heisenberg system, as well as the “ $1+x^2$ ” scaling law from SCR theory [4] (see Eq. 5.1). In the case of paramagnetic scattering, we observe that Ni₃Al shows better agreement with the predictions of the theory for itinerant systems.

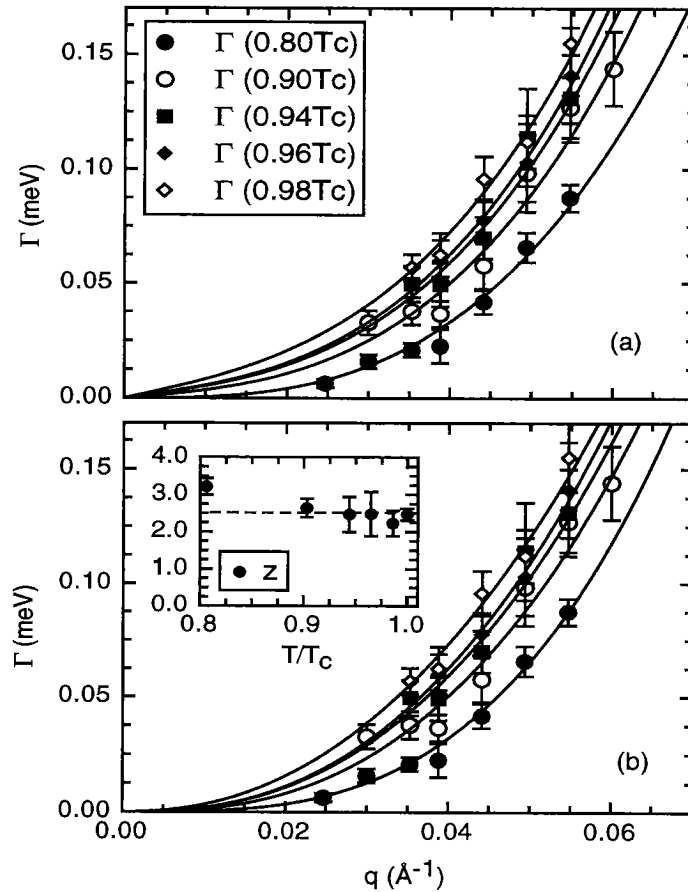


Figure 5.4: Resolution corrected spin wave linewidth $\Gamma(q)$, plotted as a function of q , for several temperatures. The plot (a) shows a fit with the itinerant model, whereas in (b), a fit with the Heisenberg model has been used. The inset displays the experimental critical exponent z as a function of temperature. The exponents are close to the 2.5 Heisenberg value (dashed line).

5.1.4 Discussion

The analysis of the magnetisation and the q -dependence of the spin-waves does not allow an unambiguous distinction between MMT and SCR. In order to obtain a more detailed comparison, we have inspected the scaling behaviour of the linewidth of the spin-waves, $f_\Gamma(x)$, near T_C , in the light of MMT that includes critical fluctuations and dipolar interactions (see Fig. 5.6). As the magnetic moments in Ni₃Al are small, we considered the special case of the isotropic limit [24].

It is seen that below T_C the data as well as MMT yield a monotonic decrease of $\Gamma(q, T)$ with decreasing T . This behaviour is in contradiction to the RPA result that predicts an increase of $\Gamma(q, T)$ with decreasing T (Ref. [28] and Eq. 4.48). We argue that the q -range probed by the experiment corresponds to wavelengths of spin waves Λ that are much larger than the correlation distance ξ_c that defines the magnetic moments. Therefore, the moments can be considered to be localised with respect to the spin excitations thus masking itinerant effects.

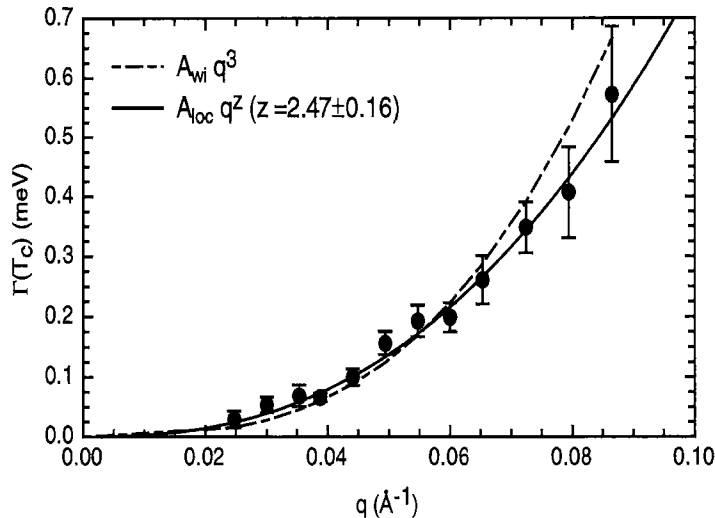


Figure 5.5: Quasielastic linewidth measured at T_C . The solid line is a fit to the Aq^z model, whereas for the dashed line the exponent has been fixed at 3, as expected from itinerant theory.

The universality of the spin-wave frequency for ferromagnets has been highlighted by Schinz *et al.* [23] within the framework of MMT. In the critical regime, the scaling amplitude W_- connects the spin-wave frequency and the damping at T_C :

$$W_- = \frac{D_0}{A\sqrt{\kappa_0^-}}, \quad (5.7)$$

where D_0 is the spin-wave stiffness at $T = 0$, A is related to the spin-wave linewidth at T_C , $\Gamma(T_c)$, and κ_0^- refers the inverse correlation length at $T = 0$. For Ni₃Al, we obtain $W_- = 1.88 \pm 0.56$. This value lies within the range of the parameters for other ferromagnets like Fe, Ni, Co, EuO, and EuS, where $1.24(14) \leq W_- \leq 2.07(9)$ (see Ref. [23]). Moreover, inelastic neutron scattering experiments performed in these ferromagnets have shown that $\Gamma(T_c)$ can be well parametrised by $Aq^{2.5}$, leading to the conclusion that the spin dynamics in localised and weak itinerant ferromagnets show a universal behaviour at T_C .

The q -dependence of the linewidth at T_C and the experimental scaling function below T_C indicate that the critical scattering cannot be neglected for describing the spin dynamics of Ni₃Al in the ordered phase.

Above T_C the interpretation of the results is less clear. Our results from single-crystal Ni₃Al agree well with previous results obtained from polycrystalline Ni₃Al [30, 34]. In fact, $\Gamma(q, T)$ shows a similar behaviour as in other well-known itinerant systems like MnSi [35] and CoS₂ [36], and the results seem to be in agreement with predictions of SCR and RPA theory, i.e. $\Gamma(q)$ is given by Eq. 5.1 in the paramagnetic phase.

The question arises why we observe dynamical scaling behaviour below T_C on the one hand and "itinerant" behaviour above T_C on the other hand. We interpret the discrepancy between the scaling functions in Fig.5.7 to be caused by the additional

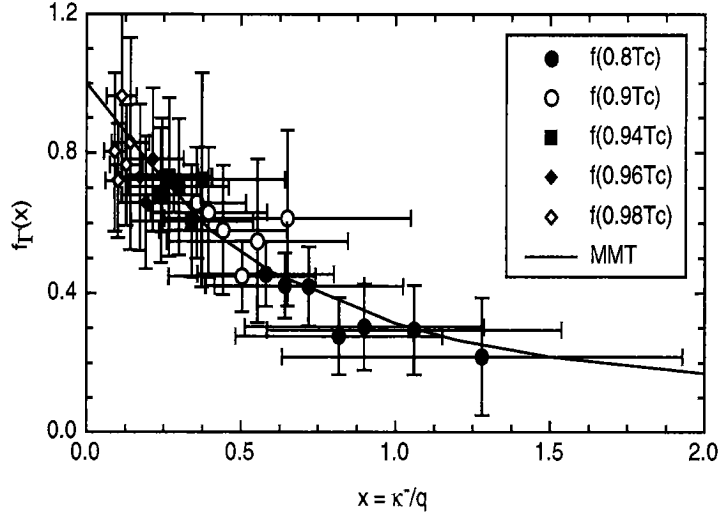


Figure 5.6: Dynamical scaling function $f_\Gamma(x)$ for the linewidth of the spin waves as a function of the scaling parameter $x = \kappa^-/q$. The solid line is given by mode-mode-coupling theory for an isotropic ferromagnet [24].

damping of the spin fluctuations by the conduction electrons. In weak itinerant ferromagnets, the mean-square local amplitude of the magnetic moments $\langle S_L^2 \rangle$ is known to be temperature dependent [4]. The variations are particularly important in the paramagnetic phase where $\langle S_L^2 \rangle$ increases linearly with T . The associated damping compensates for the initial decrease of the Réibois-Piette function at small x . Similar deviations from MMT have been observed in the metallic Heisenberg ferromagnet Pd_2MnSn and interpreted in terms of damping by the conduction electrons that provide the RKKY-interaction between the local moments [37]. As a second example we mention Ni, where $\Gamma(T_c) = Aq^{2.5}$ (Ref. [38]) although its scaling behaviour above T_C disagrees with mode-mode coupling theory [39].

In the light of the above discussion on the dynamical scaling function $f_\Gamma(x)$, we cannot exclude that damping effects also affect the spin dynamics below T_C . However, in contrast to $T > T_C$, one may argue that the combined effects of conduction electrons and critical scattering can lead to a scaling function that starts with a negative slope, if one assumes that the additional damping caused by the spin-flip excitations in the conduction band is reduced with decreasing temperature. Therefore, the latter effects merely lead to a re-scaling of the scaling variable x in $f_\Gamma(x)$. The distinction between different contributions can be done by determining the inverse correlation length below T_C , κ^- . In order to access this information, it is necessary to study the longitudinal spin fluctuations using polarised neutrons.

Finally, the determination of the fluctuation spectrum in the ordered phase allows to make a link with heavy fermion systems. A generalised formula was developed by Moriya [40] for the electronic specific heat coefficient γ in terms of the characteristic frequency $\Gamma(\mathbf{q})$ of the spin fluctuations

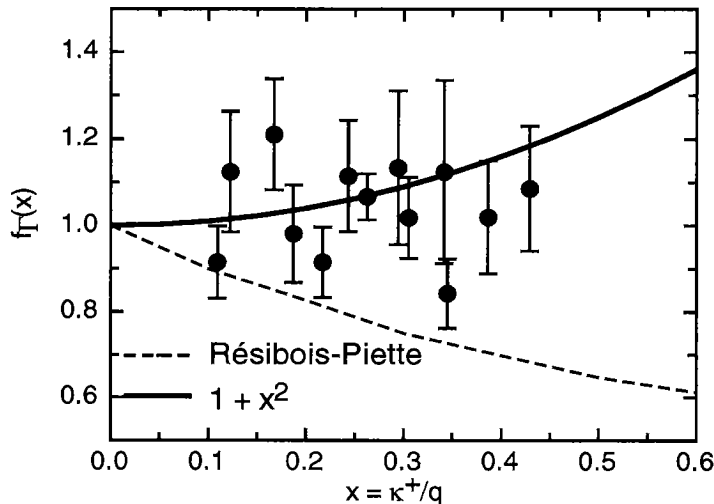


Figure 5.7: Dynamical scaling function $f_{\Gamma}(x)$ for the paramagnetic fluctuations, as a function of the scaling parameter $x = \kappa^+/q$. The dashed line represents the Résibois-Piette scaling function [20], whereas the solid line ($1+x^2$) is provided by SCR [4].

$$\gamma = \pi k_B^2 \frac{1}{\Gamma_{ave}} = \pi k_B^2 \left\langle \frac{1}{\Gamma(\mathbf{q})} \right\rangle_{BZ}, \quad (5.8)$$

where $\langle \rangle$ accounts for the average over the Brillouin zone. Figure 5.8 shows the coefficient γ plotted versus Γ_{ave} for several compounds. The data are taken from Ref. [41], except the point for Ni₃Al, that as estimated from our experimental line-width at T_C .

The value of Γ_{ave} that we obtain for Ni₃Al is in reasonable agreement with the prediction of Moriya. In this vein, the hypothesis is confirmed that only the long-wavelength part of the fluctuation spectrum contributes to the bulk properties of this compound.

5.1.5 Intermediate conclusion

The spin dynamics of weakly itinerant Ni₃Al has been studied in detail by means of inelastic neutron scattering below and above the Curie temperature T_C . The experimental data was interpreted within the framework of both itinerant (SCR-RPA) and mode-mode coupling (MMT) theories for an isotropic ferromagnet. We have determined experimentally the dynamical scaling function of the magnetic fluctuations in the ordered phase as well as in the paramagnetic phase. The temperature dependence of the damping of the magnetic fluctuations could be satisfactorily explained in the ferromagnetic phase as well as at T_C by MMT. On the other hand, the scaling behaviour above T_C matches with the theoretical predictions for an itinerant spin system.

According to the observed q -dependence of the damping at T_C , we were tempted to analyse the dynamical scaling behaviour of the spin fluctuations in the light of

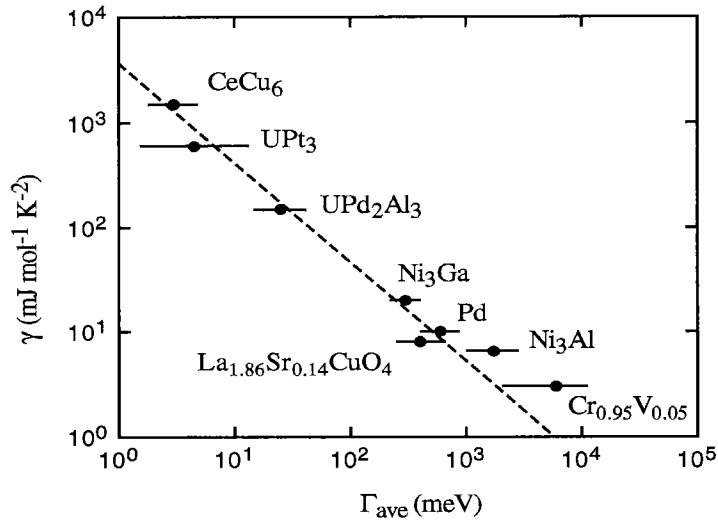


Figure 5.8: The coefficient γ of the low-temperature specific heat plotted as versus the spin relaxation rate Γ_{ave} that is averaged over the Brillouin zone. The data are taken from Ref. [41]. The dashed line is the theoretical formula proposed by Moriya [40] (see Eq. 5.8).

MMT that includes critical scattering. Nevertheless, this latter model does not take into account the itinerant character of Ni_3Al , namely the fact that the mean-square local amplitude of the magnetic moments $\langle S_L^2 \rangle$ is not constant. This feature leads to a modification of the mode-mode coupling dynamical scaling functions. The additional damping caused by the conduction electrons requires corrections for $f_\Gamma(x)$ in both magnetic phases that are qualitatively consistent with the overall behaviour of our experimental curves.

On the basis of the results obtained with Ni_3Al , we propose that it would be of interest to include critical fluctuations in the magnetic equation of state of SCR, in order to explain the dynamical scaling behaviour observed in weak itinerant magnets, within the framework of an itinerant model.

5.2 Ni

5.2.1 Introduction

For an isotropic ferromagnet, the work of Mazenko based on mode coupling theory [19] predicts a crossover for the longitudinal susceptibility χ_{\parallel} from a non diverging behaviour in the critical regime to a diverging behaviour in the hydrodynamic regime. Additionally, Schinz and Schwabl have shown that this crossover is also valid for a dipolar ferromagnet (see Eq. 4.27 in Section 4.3.2). However, in the dipolar regime the symmetry of the equations of motion is reduced, and a tensorial description is required for the dynamical susceptibility $\chi(\mathbf{Q}, \omega)$ [22, 42].

The aim of the present investigation is to measure the longitudinal mode of the spin fluctuations in the regime where χ_{\parallel} diverges, in order to confirm the theoretical predictions. We have chosen Ni, as it is a simple material the basic magnetic properties of which are already well-known.

The condition for the hydrodynamic regime is given by $\kappa_-/Q = x \gg 4.5$ (see Section 4.2). This criterion can be achieved by two means: the increase of κ_- for a given Q -range, or the decrease of Q for a selected temperature range. The first solution is not desirable as a large value of κ_- leads to a strong loss in the intensity. The second solution requires experimental Q that are too small for conventional three-axis spectrometers. The idea is therefore to use small angle neutron scattering (SANS). With this technique, the static susceptibility can be directly accessed and the available Q -range allows to achieve easily the hydrodynamic regime within a reasonable temperature range for κ_- . However, various features due to experimental conditions as well as to the physics of the sample itself make the data analysis a difficult task. First of all, the experiments are performed in the dipolar regime, where the tensorial character of the susceptibility must be taken into account. In addition, the current status of neutron optics equipment on the SANS devices does not allow a full polarisation analysis. The measured signal is hence a superposition of three modes contributing to the fluctuation spectrum (see Section 4.2). Finally, the divergence of one of the transverse modes in $1/Q^2$ constitutes an intensity problem, as it dominates the other magnetic signals.

5.2.2 Magnetic scattering with SANS

We present the scattering configuration as well as the various conventions that are used in this work. A detailed outline is shown in Fig. 5.9, and we briefly discuss the various elements of the scattering scheme.

In a SANS experiment, the sample is illuminated by a monochromatic neutron beam, with a wavevector \mathbf{k}_i that we take as y -axis. By applying an external magnetic field perpendicular to \mathbf{k}_i , the direction of the magnetisation \mathbf{M} is defined, and taken as z -axis. Subsequently the x -axis is perpendicular to the plane defined by \mathbf{k}_i and \mathbf{M} . A given final wavevector \mathbf{k}_f defines a particular scattering vector \mathbf{Q} as well as a scattering angle Θ . The unit vector $\hat{\mathbf{p}}$ is the projection of \mathbf{Q} onto the plane perpendicular to \mathbf{M} . The eigenvectors of the static susceptibility tensor, \mathbf{v}_i ($i=1,2,3$)

are defined with respect to \mathbf{Q} and \mathbf{M} . In the case of isotropic interactions, \mathbf{v}_2 is aligned along $\hat{\mathbf{p}}$, \mathbf{v}_3 along \mathbf{M} and \mathbf{v}_1 perpendicular to the (\mathbf{M}, \mathbf{Q}) -plane. The effect of dipolar forces introduces an angle φ_3 which accounts for the rotation of the vectors \mathbf{v}_2 and \mathbf{v}_3 relative to \mathbf{M} and \mathbf{Q} . The dipolar angle φ_3 is defined within the range $[0, \pi/2]$, where $\varphi_3 = \pi/2$ denotes the isotropic limit.

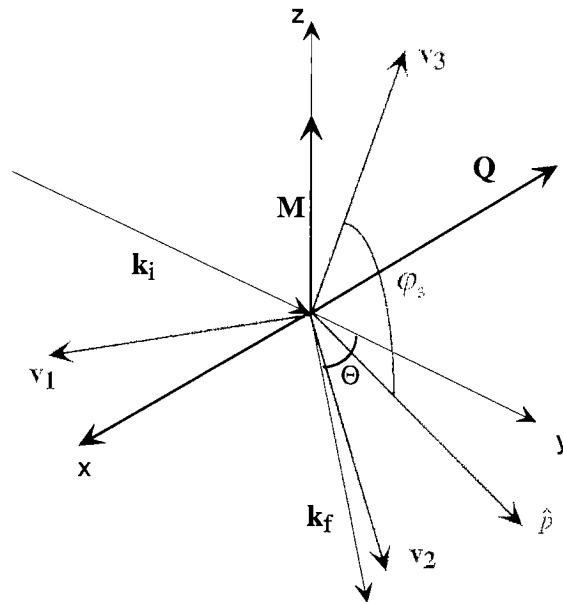


Figure 5.9: Scattering scheme used for analysing the SANS measurements (see text for details). \mathbf{k}_i and \mathbf{k}_f are the initial and final neutron wavevector; \mathbf{Q} is the scattering vector and \mathbf{M} the magnetisation vector of the sample. $\hat{\mathbf{p}}$ is the projection of \mathbf{Q} onto the plane perpendicular to \mathbf{M} . The \mathbf{v}_i are the eigenvectors of the susceptibility tensor. Θ is the scattering angle, φ_3 the rotation angle due to dipolar effects. \mathbf{v}_1 is perpendicular to the plane, all other vectors lie in the plane defined by \mathbf{M} and \mathbf{Q} .

When the dynamical susceptibility is considered, an additional rotation angle is introduced in the dipolar regime, which makes the model more complicated. We refer to the publication of Schinz and Schwabl [23] for a comprehensive description of the problem.

The theoretical neutron cross-section is obtained in several steps. The $\chi^{ij}(\mathbf{Q}, \omega)$ matrix elements are taken from the analytical formulae given by the mode-coupling theory, in the coordinate system where $\chi(\mathbf{Q}, \omega)$ is diagonal [42]. In order to take into account the finite linewidth of the spin fluctuations, we have used a quasielastic spectral weight functions for the longitudinal mode and a dispersive one, according to Eq. 4.30 of Section 4.3.3, for the transverse modes. As a second step, the dynamical susceptibility is transformed by matrix rotation into $\tilde{\chi}(\mathbf{Q}, \omega)$ in the SANS coordinate system defined by \mathbf{k}_i and \mathbf{M} (see Fig. 5.9), where the neutron polarisation factor as well as the temperature factor are added. As there is no analysis of the neutron final energy in SANS, the scattering intensity for a given \mathbf{Q}_0 is obtained by performing an integration along a constant scattering angle curve:

$$I(\mathbf{Q}_0) = N \int_{\omega_{min}}^{\omega_{max}} d\omega \frac{\omega}{1 - \exp(-\beta\omega)} \sum_{\alpha,\beta} (\delta_{\alpha\beta} - \hat{Q}_\alpha \hat{Q}_\beta) \tilde{\chi}^{\alpha\beta}(\mathbf{Q}(\theta, \omega), \omega). \quad (5.9)$$

α, β are the cartesian coordinates, and the integration limits are selected according to the rules of kinematics for a given initial neutron wavevector \mathbf{k}_i .

5.2.3 Experiment and data analysis

The experiments have been performed on several Ni plates of dimension 20 x 20 x 1 mm³. We have used single crystals for avoiding the nuclear scattering that arises from the grains of a polycrystalline sample. The background from incoherent scattering as well as from the sample environment has been determined by the application of a sufficiently large magnetic field that quenched all the magnetic signal. The sample was polished in order to reduce scattering arising from the surface roughness. Figure 5.10 shows an example of measurements on a non-polished sample for a fixed temperature of 612K (0.97T_C) and various strengths of the applied magnetic field. The low magnetic field data shows a hump that is due to magnetic scattering. At the maximal field H_{ext} = 7kG, the magnetic signal is quenched but the intensity at low Q (≤ 0.05 nm⁻¹) is still considerable. The shape of the magnetic signal can be explained as follows: for a given temperature, the dispersion of the spin-waves does not fulfill the kinematical scattering conditions beyond a cutoff wave vector Q*(T, H). By increasing the external field, the Zeeman gap shifts the cutoff to lower Q-values. In contrast, an increase of T would renormalise the spin-wave and the hump would be shifted towards higher Q-values.

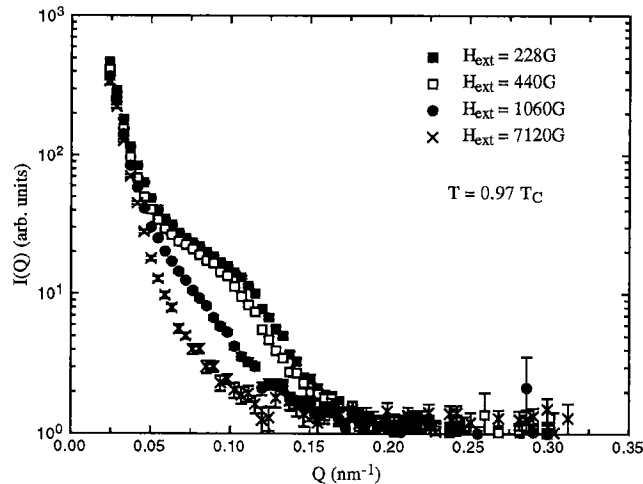


Figure 5.10: Scattered intensity integrated over the azimuthal angle of the detector for a Ni sample where the surface was not polished. For low applied magnetic fields, the magnetic scattering is visible as a hump in the curve. The drop of the intensity at large Q is due to the kinematical limitations for the spin-wave dispersion in small angle scattering. The non magnetic background shows the residual intensity arising from scattering at the surface roughness.

The Curie temperature T_C of the sample was determined by measuring the critical

scattering as a function of temperature in zero field. The obtained value is $T_C = 631 \pm 0.5\text{K}$, in agreement with the literature value [44].

A further characterisation of the sample consists of determining the demagnetisation factor N_z , which depends on the shape of the sample. N_z is obtained from the relation $H_{eff} = H_{ext} - 4\pi M(T)N_z$, that relates the internal magnetic field H_{eff} to the applied field H_{ext} and the magnetisation $M(T)$. A variation of the applied magnetic field is shown in Fig. 5.11, for a fixed temperature of $T=0.99T_C$. At the lowest field value, additional scattering from magnetic domains is visible at low Q ($\leq 0.05 \text{ nm}^{-1}$). For intermediate applied fields, this additional intensity disappears, and the spin-wave hump begins to be shifted towards lower Q . The value of H_{ext} for which $Q^*(T, H)$ starts to move defines the situation where H_{eff} is zero, i.e. where the Zeeman gap opens in the spin-wave dispersion. Using the literature value for $M(T)$, we obtain $N_z = 0.135 \pm 0.005$. This value is reasonable for a sample with a plate-like shape and a finite width.

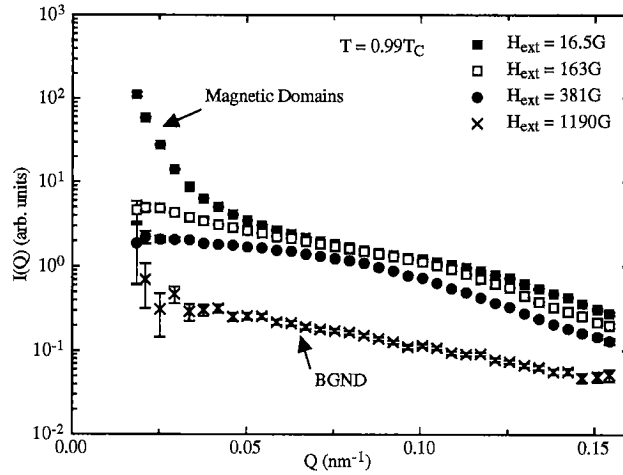


Figure 5.11: Magnetic scattering in Ni at $T=0.99T_C$, for several applied fields. The value of $H_{ext}=16.5\text{G}$ is not sufficient to align the magnetic domains, that adds to the magnetic intensity (indicated in the plot) at low Q -values. The increase of H_{ext} is observed to reduce drastically this latter effect. The background at $H_{ext} = 1.2\text{kG}$ shows the intensity arising from the nuclear background and the sample environment.

Below T_C , the magnetic scattering is clearly anisotropic (see Fig. 5.12). According to the polarisation factor, the signal corresponding to the case $\mathbf{M} \parallel \mathbf{Q}$ contains the two transverse modes, whereas the case $\mathbf{M} \perp \mathbf{Q}$ includes one transverse mode and the longitudinal mode. On a qualitative point of view, the signal arising from the two spin-wave modes is larger than the other one, if one considers the corresponding static susceptibilities. This disparity is indeed observed experimentally. Furthermore, the dipolar forces modify the spin-wave dispersion for $\mathbf{M} \perp \mathbf{Q}$. As a consequence, the cutoff wavevector exhibits an angular dependence that is approximately proportional to the azimuthal angle of the SANS detector. Above T_C , the scattering is paramagnetic and the anisotropy has disappeared (see Fig 5.12 (d)). The discrepancies at T_C (Fig 5.12 (c)) are explained by the cumulative uncertainty

of the determination of the ordering temperature and the stability of the furnace. Notice that an external field of $\approx 250\text{G}$ was applied for aligning the magnetic domains. This low field value does not modify the paramagnetic scattering intensity significantly.

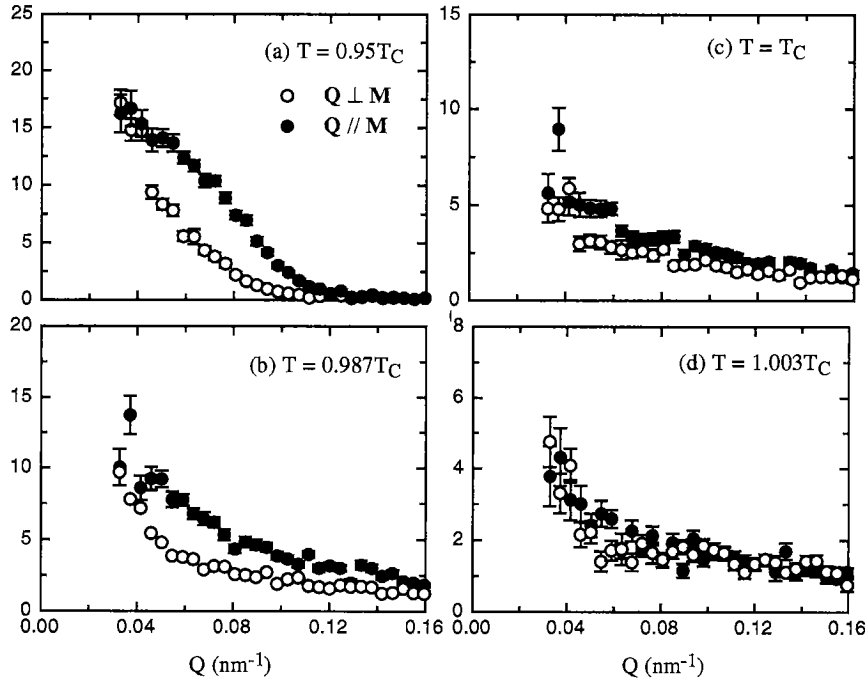


Figure 5.12: Azimuthal anisotropy in the magnetic intensity (in arbitrary units). The plots represent two sectors of the detector taken parallel and perpendicular to the magnetisation \mathbf{M} , the direction of which is selected by the applied field $H_{ext} = 250\text{G}$. The data below T_C , (a) and (b), indicate that the signal is larger for the sector corresponding to $\mathbf{M} \parallel \mathbf{Q}$. This anisotropy is reduced by increasing the temperature. Eventually the signal becomes isotropic for $T \geq T_C$, (c) and (d).

A fit of the magnetic intensity at $H_{ext} = 400\text{G}$ and $T = 0.95T_C$ is presented in Fig. 5.13. The intensity was integrated over the azimuthal angle for improving the statistics. For this temperature and Q -range, the dipolar angle ϕ_3 does not deviate significantly from $\pi/2$. Hence, the rotation of the eigenvectors of $\chi(\mathbf{Q}, \omega)$ does not play a major role in the experiment. Moreover, the estimation of the scaling variable y yields $q_D/Q \in [0.8, 8.5]$, if one assumes that the dipolar wavenumbers above and below T_C are identical ($q_d \approx 0.13 \text{ nm}^{-1}$). The system is hence investigated in a regime that is near the boundary of the dipolar region. On the other hand, the hydrodynamic regime is satisfactorily covered, as the variable x is in the range $[4.0, 50.0]$. The physical parameters that are obtained from the fit are shown in the inset of Fig. 5.13. The dipolar wavenumber does not differ much from the literature value that was obtained by SANS measurements above T_C [43]. The value of the demagnetisation factor N_z is also consistent with the one that was estimated by the study of the field dependence of the magnetic scattering (Fig. 5.11). However, the contribution of the parallel fluctuations is still negligible for $T=0.95T_C$. A calculation of the static susceptibilities within the framework of mode-coupling

theory predicts that χ_{\parallel} is more than 100 times larger than χ_{\perp} .

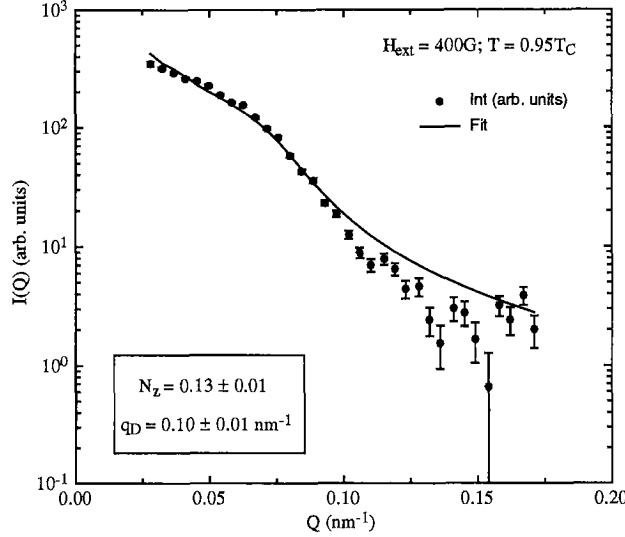


Figure 5.13: Neutron intensity at $T = 0.95 T_C$, with $H_{ext} = 400$ G. The measurements have been fitted with the mode-coupling model. The inset gives the obtained fit parameters. M_o , N_z and q_D are the saturation magnetisation, the demagnetisation factor and dipolar wave-number, respectively.

Finally, we present a computer simulation of the magnetic scattering that is expected very close to the ordering temperature ($T = 0.99 T_C$), i.e. where the intensity of the longitudinal fluctuations is becoming significant (see Fig. 5.14). The calculations were performed assuming the values for N_z and q_D that were obtained at a lower temperature (see Fig. 5.13). The plot shows the magnetic intensity at $T=0.99 T_C$ for the case $\mathbf{Q} \perp \mathbf{M}$, where the longitudinal fluctuations and one spin-wave mode contribute to the total intensity. As T_C is approached, the interval of the scaling variable x is inevitably shifted to lower values: [1.5, 20]. However, for the smaller Q -values the hydrodynamic conditions are still fulfilled. Indeed, the calculation of χ_{\perp} in the case of a Lorentzian approximation (see Eq. 4.13) shows that the calculated points deviate from the mode coupling curve below $Q = 0.05 \text{ nm}^{-1}$.

To summarise, the simulation indicates that the Q -range in which the $1/Q$ divergence should be observed is unfortunately dominated by the spin-wave channel, and the intensities of the two modes become comparable only for higher Q -values, where the critical regime is achieved.

5.2.4 Intermediate conclusion

In this work, we have tried to measure by means of the SANS technique the predicted $1/Q$ divergence of the longitudinal magnetic susceptibility χ_{\parallel} . In parallel, computer simulations based on mode-coupling theory were done in order to interpret the data. The predicted anisotropy that should occur below T_C was observed and two physical parameters, the demagnetisation factor N_z and the dipolar wavenumber q_D , could be

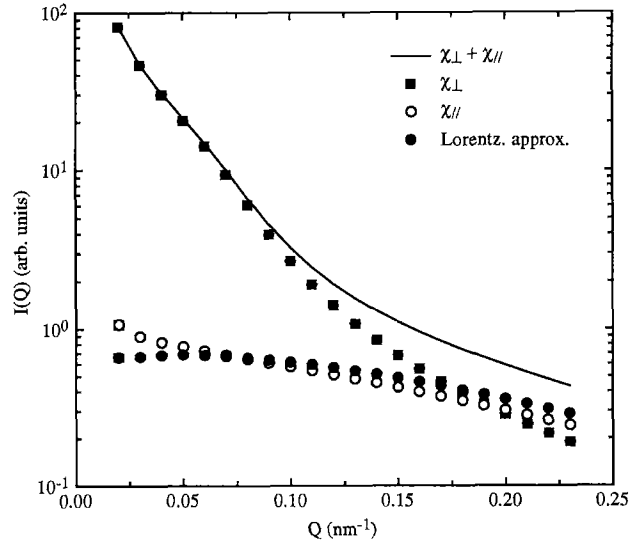


Figure 5.14: Magnetic scattering calculated on the basis of the mode coupling model, for the case $\mathbf{Q} \perp \mathbf{M}$ and for $T=0.99T_C$. The solid line represents the total intensity which is composed of one spin-wave mode (squares) and the longitudinal mode (open circles). The solid circles represent the intensity of χ_{\parallel} in the Lorentzian approximation.

extracted from the measurements. Unfortunately, both experiments and calculations have shown that the search of the $1/Q$ divergence is obscured by a serious problem: The simultaneous requirement to be in the hydrodynamic regime and to achieve a reasonable signal for χ_{\parallel} .

SANS seems however to be a promising technique, as it allows to achieve an experimental geometry that is required for studying the longitudinal susceptibility. Further investigations should be however performed on SANS with full polarisation analysis. The various magnetic contributions can be indeed separated by this technique, as the spin-wave are spin-flip and the longitudinal fluctuations are non spin-flip.

Chapter 6

Localised Spin Systems

*Chacun sait que la ligne droite ne peut être
le plus court chemin d'un point à un autre.
Sauf, évidemment, si les deux points
sont bien en face l'un de l'autre.*

Pierre Desproges

6.1 Paramagnetic scattering in EuS at very high temperature

6.1.1 Introduction

The magnetic properties of the insulating ferromagnets EuS and EuO are governed by the localised 4f electrons of the Eu^{2+} ions that form a fcc lattice. These compounds are therefore an almost ideal realisation of the isotropic cubic Heisenberg ferromagnet, the model which has been so far the most completely explored theoretically.

In this work, we focus on the paramagnetic scattering of the EuS compound, where the magnetic excitations of the ordered phase were extensively studied in the past decades [45, 46, 47, 48]. In this system, the magnetic Eu^{2+} ions form a ground state $^8S_{7/2}$, with a saturated moment of $7\mu_B$. The lattice constant is $a=5.95\text{\AA}$ and the moments order below the Curie temperature $T_C = 16.6\text{K}$.

Below T_C , the linear spin wave theory based upon the Heisenberg model predicts the existence of propagating modes that extend over the whole Brillouin zone. The spin wave dispersion measured with neutron scattering by Bohn et al. [49] can be well reproduced by taking into account nearest and next nearest neighbour exchange interactions, $J_1 = 0.038\text{ meV}$ and $J_2 = -0.017\text{ meV}$, respectively.

In the paramagnetic state, two limiting cases have to be considered, depending on the value of the scattering vector q with respect to the zone boundary wavevector q_{ZB} . Near the zone center ($q \ll q_{ZB}$), a model provided by asymptotic renormalisation theory [50] predicts a quasielastic spectrum that describes a spin diffusion process. The magnetic scattering function is given by a double Lorentzian function

$$S(\mathbf{q}, \omega) = 2k_B T \chi(\mathbf{q}) \frac{\beta \omega}{1 - e^{-\beta \omega}} \frac{1}{\pi} \frac{\Gamma}{\Gamma^2 + \omega^2}, \quad (6.1)$$

where $\beta = 1/k_B T$. In the molecular field approximation, the static susceptibility $\chi(\mathbf{q})$ is in the small q limit [8]:

$$\chi(\mathbf{q}) = \chi(0) \frac{\kappa_+^2}{q^2 + \kappa_+^2}. \quad (6.2)$$

$\kappa_+(T)$ is the inverse of the correlation length above T_C , and $\chi(0)$ is the bulk susceptibility. The inverse correlation length was measured in EuS by Als-Nielsen et al. [46] who obtained $\kappa_+ = 0.55((T - T_C)/T_C)^{0.702} \text{ \AA}^{-1}$.

Near the zone boundary ($q \simeq q_{ZB}$), the theory based on an effective Heisenberg model does not predict diffusive modes but rather damped modes associated with short range magnetic correlations [51, 52]. In this case, the scattering function is given by

$$S(\mathbf{q}, \omega) = 2k_B T \chi(\mathbf{q}) \frac{\beta \omega}{1 - e^{-\beta \omega}} F(\mathbf{q}, \omega). \quad (6.3)$$

For large q values $\chi(\mathbf{q})$ is expressed in terms of Fourier components of the exchange interaction $J(\mathbf{q})$. In the spherical approximation [8] one obtains

$$\chi(\mathbf{q}) = \frac{1}{J(0) - J(\mathbf{q}) + \chi(0)^{-1}}. \quad (6.4)$$

The normalised spectral weight function $F(\mathbf{q}, \omega)$ is derived from the equation of motion of the spin system by assuming the three-pole approximation [5, 52]

$$F(\mathbf{q}, \omega) = \frac{1}{\pi} \frac{\tau \delta_1 \delta_2}{[\omega \tau (\omega^2 - \delta_1 - \delta_2)]^2 + (\omega^2 - \delta_1)^2}. \quad (6.5)$$

δ_1 , δ_2 and τ are quantities related to the first $\langle \omega^2 \rangle_{\mathbf{q}}$ and second moment $\langle (\omega^2 - \langle \omega^2 \rangle_{\mathbf{q}}) \rangle_{\mathbf{q}}$ of $F(\mathbf{q}, \omega)$:

$$\delta_1 = \langle \omega^2 \rangle_{\mathbf{q}} \quad (6.6)$$

$$\delta_1 \delta_2 = \langle (\omega^2 - \langle \omega^2 \rangle_{\mathbf{q}}) \rangle_{\mathbf{q}} \quad (6.7)$$

$$\tau = (\pi \delta_2 / 2)^{-1/2}. \quad (6.8)$$

If $\delta_2 > 2\delta_1$ the shape of $F(\mathbf{q}, \omega)$ exhibits one peak centered at $\omega = 0$. In the opposite situation, $F(\mathbf{q}, \omega)$ has three peaks centered at $\omega = 0$ and $\omega = \pm \omega_{sw}$, where ω_{sw} is a complicated function of δ_1 and δ_2 .

The two models have been proven to be valid up to $T = 3T_C$ with neutron scattering experiments on EuS [48] and EuO [53], over the whole Brillouin zone in the [100] and [111] symmetry directions.

According to the theory, for q near q_{ZB} , the linewidth of $F(\mathbf{q}, \omega)$ is predicted to remain finite in the infinite temperature limit [5, 52, 54]. In order to prove this interesting result, we extended the measurements on EuS to the high temperature regime (up to $\approx 18T_C$).

6.1.2 Results

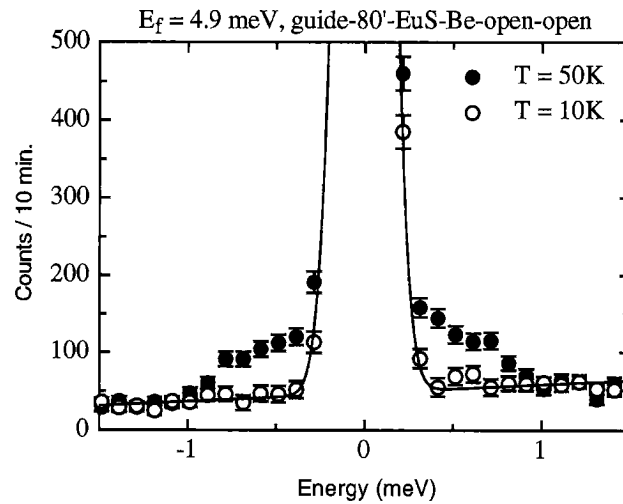


Figure 6.1: Paramagnetic spectrum at $T=50\text{K}$ ($\approx 3T_C$) for $q = 0.84 \text{ \AA}^{-1}$ (solid circles). The background (open circles) was determined at $T=10\text{K}$ (i.e. below T_C) and is mainly due to the large incoherent elastic contribution. The solid line is a Gaussian fit to the low temperature scan.

Experimental details

For the experiment, we have used a sample consisting of about 100 small pieces of single crystal ($\approx 2 \times 2 \times 1 \text{ mm}^3$), which are fixed on a aluminum plate and oriented with the $[100]$ symmetry direction perpendicular to the plate.

The measurements have been performed on the three-axis spectrometer TASP, with fixed final neutron energies $E_f = 4.9$ and 3.6 meV. The higher-order neutrons were removed by a Be filter. The sample was mounted on the cold finger of a closed cycle cryostat, allowing an experimental temperature range between 10K and 293K . The inelastic scans have been conducted in the constant- q mode of operation, in the $[100]$ direction, near the zone boundary of the (200) Bragg peak. The background from the sample environment and from incoherent scattering was determined by measurements below the ordering temperature $T_C = 16.6\text{K}$.

Data analysis

Figure 6.1 shows an example of an inelastic scan performed at $T=50\text{K}$ and $q = 0.84 \text{ \AA}^{-1}$ ($q = 0.8 q_{ZB}$). The determination of the background was done by repeating

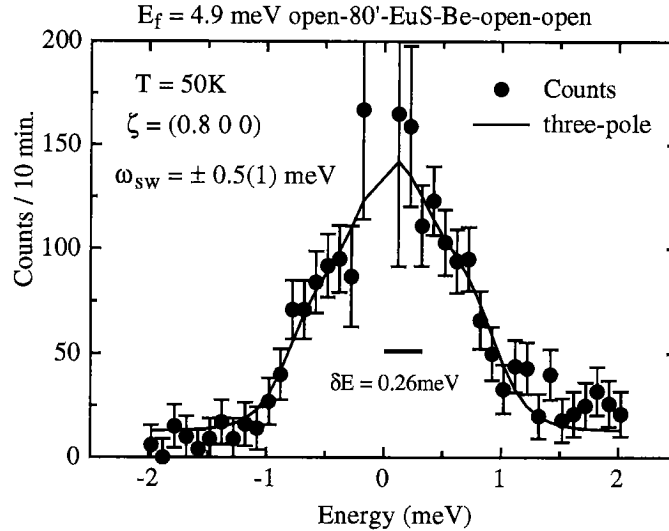


Figure 6.2: Inelastic scan of Fig. 6.1 after removing the background. The solid line is a fit to the data according to the three-pole approximation (see Eq.6.3) taking into account the experimental resolution of the spectrometer. The values obtained for the two poles ω_{sw} are mentioned in the graph. The energy resolution (FWHM), $\delta E = 0.26 \text{ meV}$, is also displayed.

the measurement at $T=10\text{K}$, where the magnetic scattering is known to be outside the experimental energy window [46]. The elastic linewidth of the background that arises from incoherent scattering of the sample provides an indication of the experimental resolution of the spectrometer.

After background subtraction, the scans have been fitted with the scattering function given by Eq. 6.3, taking into account the experimental resolution of the spectrometer. As an example, the background-corrected scan from Fig. 6.1 is shown in Fig. 6.2 on an expanded scale. The large error bars near the elastic position account for the fact that large intensities have been subtracted. The lineshape is in good agreement with the theoretical predictions [52] as it has been demonstrated by earlier experiments [48, 53, 55]. Further measurements have been performed up to room temperature ($\approx 18 T_C$), where the paramagnetic signal was still visible (see Fig. 6.3).

The parameters δ_1 and δ_2 obtained from the fit have been compared with theoretical values provided by the model of the three-pole approximation [5, 52]. The calculations were made numerically by using a *FORTRAN* code [56] based upon a formula derived in Ref. [52]. We present in Fig. 6.4 a comparison between calculated (open circles) and measured (solid circles) values. For clarity we have separated the data obtained for $q = 0.84 \text{ \AA}^{-1}$ and $q = 1.06 \text{ \AA}^{-1}$. The general trend for both parameters is to decrease with increasing temperature as expected from the theoretical predictions.

Although the scattering intensity is strongly reduced due to the decrease of the susceptibility, the lineshapes are still visible in the high temperature limit, and the δ 's are in agreement with the calculated values. The deviation for $T=18\text{K}$ ($\approx 1.08 T_C$) can be explained by the fact that the three-pole approximation becomes not appropriate near the transition temperature. In contrast, both experimental

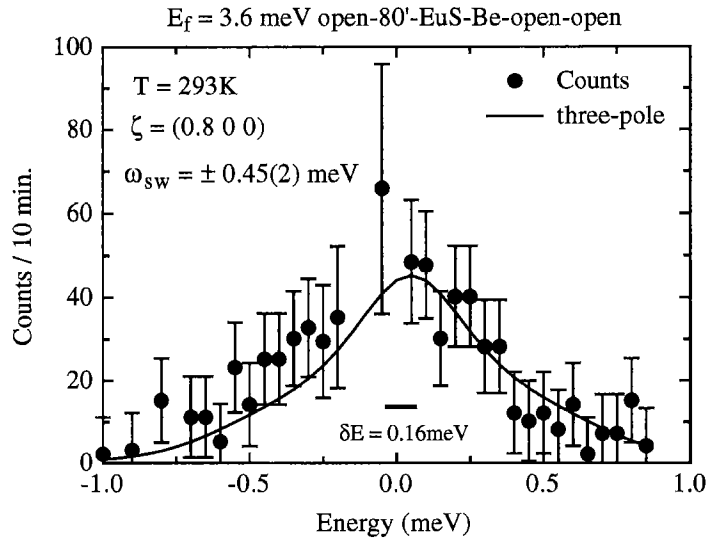


Figure 6.3: Paramagnetic spectrum at room temperature for $q = 0.84 \text{ \AA}^{-1}$. The background has already been subtracted. The solid line is a fit similar to that of Fig. 6.2. Again, the values obtained for $\pm\omega_{sw}$ are indicated in the graph. The energy resolution was improved by lowering the final energy of the neutrons ($E_f = 3.6 \text{ meV}$).

and calculated values indicate that the second and fourth moment of the spectral function $F(\mathbf{q}, \omega)$ tend to a constant in the high temperature limit, as indicated by the dashed lines in Fig. 6.4.

The fit of the neutron spectra with Eq. 6.3 have also provided experimental values for the static susceptibility $\chi(\mathbf{q})$. Figure 6.5 shows the experimental data as well as the values that have been calculated assuming the spherical model (see Eq. 6.4) and the exchange interaction parameters J_1 and J_2 found in the literature [49]. The measured susceptibility has been adjusted to the theoretical value by using a unique scaling factor, a normalisation constant that accounts for the neutron counting time and the efficiency of the various devices composing the three-axis spectrometer. The agreement between both datasets is a confirmation of the consistency of the model that was used for analysing the neutron data.

Finally, a careful inspection of the high temperature behaviour of the scattering function at the zone boundary can explain why the signal is still visible one order of magnitude above T_C . Equation 6.3 can be indeed decomposed into three terms. According to the theory, the spectral function $F(\mathbf{q}, \omega)$ does not vary much at high temperature and the temperature factor $\beta\omega/(1 - \exp(-\beta\omega))$ tends towards 1. The decrease of the static susceptibility $\chi(\mathbf{q})$ is hence compensated by the prefactor $k_B T$.

6.1.3 Intermediate conclusion

The paramagnetic scattering of the Heisenberg ferromagnet EuS was investigated by means of neutron scattering, and magnetic excitations have been observed up to room temperature near the zone boundary. The theoretical prediction that spin fluctuations are still present at high temperatures is confirmed up to $\approx 18T_C$. It is

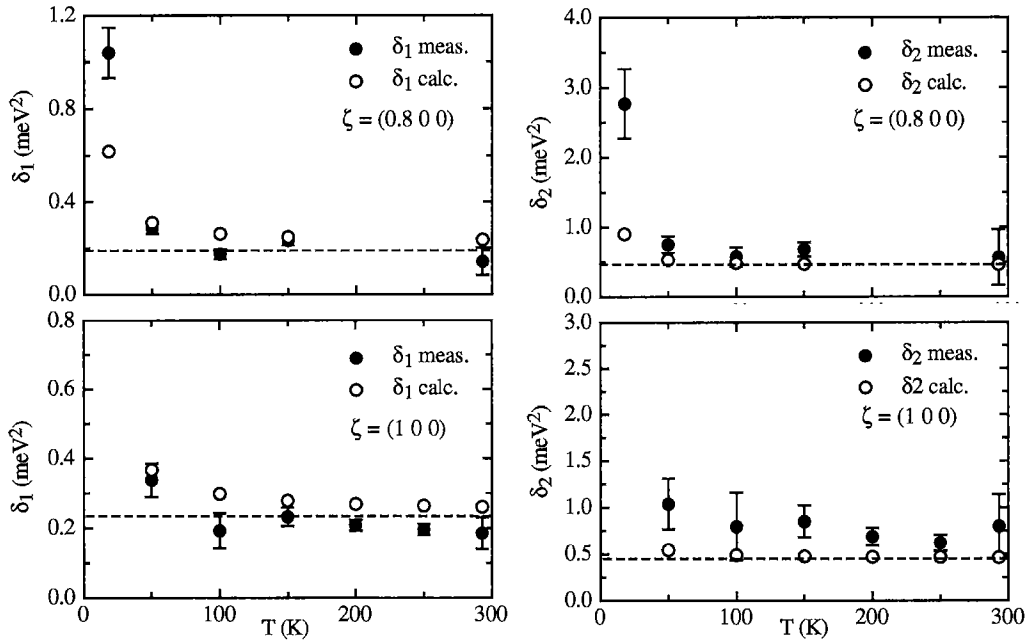


Figure 6.4: The parameters δ_1 and δ_2 as a function of temperature for the two experimental scattering vectors $q = 0.84\text{\AA}^{-1}$ and $q = 1.06\text{\AA}^{-1}$. The open circles result from numerical calculations according to the three-pole approximation model. The solid circles represent the experimental parameters obtained by the analysis of the neutron spectra with the scattering function of Eq. 6.3. The dashed lines are guides to the eyes that indicate the threshold for δ_1 and δ_2 at infinite temperature.

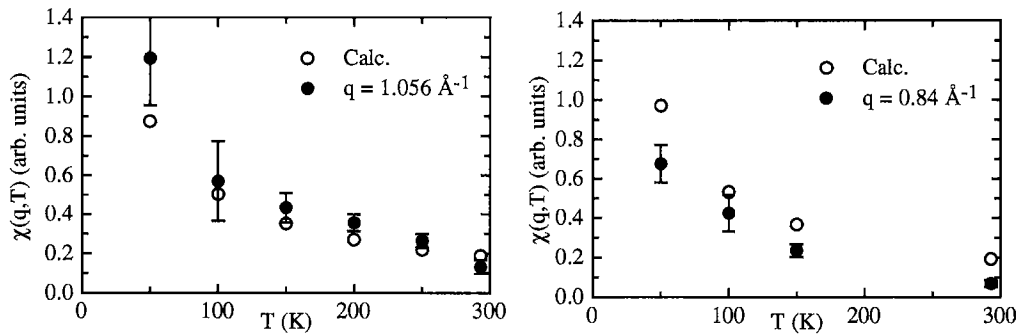


Figure 6.5: Static susceptibility $\chi(\mathbf{q})$ as a function of T . The open circles are calculated via the spherical model approximation, using Eq. 6.4 as well as the exchange interaction parameters J_1 and J_2 from the literature [49]. The experimental values (solid circles) have been obtained from fit according to Eq. 6.3.

remarkable to observe paramagnetic scattering at these very high temperatures, as one would expect the lifetime of the fluctuations to be zero and the spin correlation to vanish, because of the high kinetic energy when compared with the exchange interaction between neighbouring spins.

6.2 The inorganic spin-Peierls compound CuGeO_3

Remark: In this part of the Chapter, we shall use the symbol μ_{eff} for the effective moment below the ordering temperature, instead of p_s that was introduced in Chapter 1.

6.2.1 Introduction

Among low dimensional magnetic systems with AF interactions, the spin-Peierls compounds have attracted a renewed interest since the discovery of a similar transition in the inorganic compound CuGeO_3 by Hase et al. [57]. At high temperature, CuGeO_3 is considered to be made of magnetic chains consisting of magnetic moments with a period of c (lattice parameter) and one exchange parameter J_c for nearest neighbour spin coupling (see Fig. 6.6 (a)). Below the spin-Peierls temperature $T_{SP} = 14$ K, the system undergoes a structural phase transition and the lattice becomes dimerised, with an alternating intrachain exchange interaction, $J_{1,2} = J_c \cdot (1 \pm \delta(T))$ (see Fig. 6.6 (b)), where $\delta(T)$ denotes the temperature dependent lattice distortion. The first systems exhibiting a SP transition were organic compounds where spin substitution was not easy to perform [7, 58, 59]. In contrast, CuGeO_3 is believed to be an ideal system to study doping effects on the SP ground state, as the only magnetic elements (Cu^{2+} ions) can be easily replaced.

The first study on a Zn-doped compound [60] has revealed the presence of a new phase transition below the SP ordering temperature T_{SP} . This has been the starting point of an extensive investigation of the effect of doping on CuGeO_3 that has shown two main effects. The lattice dimerisation is progressively suppressed upon increasing doping. Moreover an antiferromagnetic ordering sets in, that coexists with the SP state, and persists for high doping concentration where the lattice dimerisation does not occur anymore.

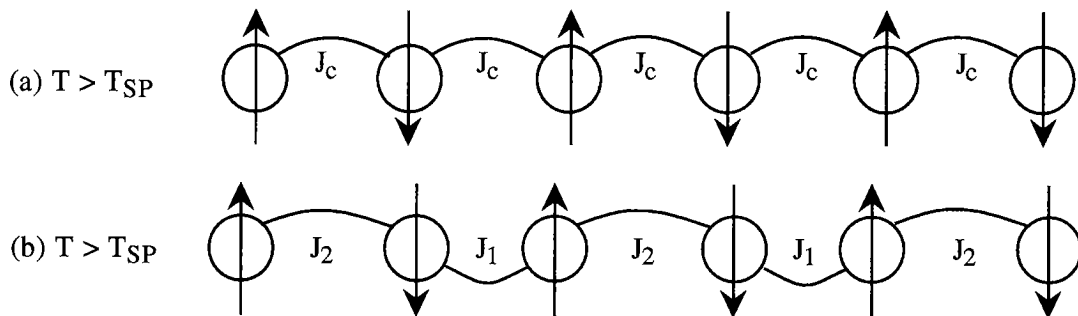


Figure 6.6: (a) Antiferromagnetic spin chain in CuGeO_3 , above T_{SP} , characterised by an exchange interaction J_c between nearest neighbours magnetic ions. (b) Below T_{SP} , a lattice dimerisation occurs and the exchange becomes alternate.

In this Chapter we present a detailed study of the temperature-concentration (T - x) phase diagram of Si-doped CuGeO_3 single crystals by means of neutron diffraction as well as zero-field and transverse field muon spin rotation (μSR). In addition, the

magnetic excitation spectrum for selected single crystals is investigated by means of inelastic neutron scattering.

6.2.2 Overview on pure and doped CuGeO₃

CuGeO₃ crystallises within an orthorhombic structure of space group Pbmm. The lattice parameters at room temperature are $a = 4.81 \text{ \AA}$, $b = 8.43 \text{ \AA}$ and $c = 2.95 \text{ \AA}$. Below T_{SP} , the Cu²⁺ ions form a non-magnetic singlet ground state that is separated from the first excited triplet [61] by an energy gap proportional to T_{SP} , $\Delta(T = 0) \approx 1.77k_B T_{SP}$ [62]. The gap is observed to scale directly with the lattice distortion $\delta(T)$. The exchange coupling between Cu²⁺ ions was determined by measuring the dispersion of the magnetic excitations along the three principal crystallographic directions, and were found to be $J_c = 10.4 \text{ meV}$, $J_b \approx 0.1 \cdot J_c$ and $J_a \approx -0.01 \cdot J_c$ [62]. CuGeO₃ is therefore considered as a quasi one-dimensional spin system.

In CuGeO₃, there are essentially two possibilities of element substitution: site (Cu_{1-x}M_xGeO₃) [63, 64, 65] and bond (CuGe_{1-x}Si_xO₃) doping [66, 67]. For site doping the Cu²⁺ ions are randomly replaced by another ion (Zn²⁺ (S=0), Ni²⁺ (S=1), Mg²⁺ (S=0)) leading to a break in the dimerised chains. In contrast, the bond doping induces a local distortion of the lattice that also affects the long range order of the chains.

Grenier et al. [68] have shown that the temperature-concentration(T-x) phase diagram for site and bond doping in CuGeO₃ exhibit a similar behaviour. The main features are the reduction of T_{SP} with increasing doping concentration, the suppression of the SP transition at a critical concentration x_c , the onset of an AF phase characterised by an ordering temperature T_N increasing with x , and decreasing for concentrations larger than x_c . The critical concentration x_c is of the order of 3% for site doping and about three times smaller for the bond doping scenario.

An inspection of Mg-doped compounds near x_c by means of magnetic susceptibility [69] and neutron scattering measurements [70] provided a more detailed description of the phase diagram for the site-doped SP. The ordering temperature T_N and the order parameter μ_{eff} of the antiferromagnetic phase exhibit a discontinuity at $x_c \approx 2.7\%$. The proposed interpretation is that doped CuGeO₃ undergoes a first order phase transition at the critical concentration x_c that constitutes a compositional phase boundary. A distinction is therefore introduced between a dimerised AF phase (D-AF) below x_c , and a uniform AF phase for higher concentration (U-AF). Susceptibility measurements near x_c performed by Masuda et al. [71] revealed the presence of a double peak region, which was interpreted as a coexistence of both D-AF and U-AF phases. In addition they have performed high-resolution synchrotron diffraction on the (3/2 1 3/2) superlattice reflection. For low doping, the X-ray peak profile is resolution limited, indicating the presence of long range order in the lattice dimerisation. In the region where doping induces a double peak in the susceptibility, the superlattice X-ray peak broadens, thus indicating the onset of short range order in the SP phase.

On the other hand, an extensive study of Si-doped compounds with susceptibility

measurements was performed by Grenier et al. [72]. They have shown that the introduction of Si ions reduces the intensity of the signal attributed to the dimerised phase. Moreover an additional peak appears below T_{SP} , which is interpreted as the onset of an antiferromagnetic ordering at a temperature T_N . Above T_N , they observe an additional intensity in the susceptibility which is attributed to the freeing of $S=1/2$ spins near the doping centers. The proportion of the SP signal linearly decreases with increasing doping, whereas the proportion of free spins increases. However, no double peak feature is observed in the susceptibility measurements in the vicinity of the critical doping concentration where the SP phase collapses.

Chemical cell of CuGeO_3

The chemical structure of pure CuGeO_3 was determined by means of single-crystal X-ray and neutron diffraction measurements [73, 74]. The projection of the structure onto the ab - and bc -planes is shown in Fig. 6.7.

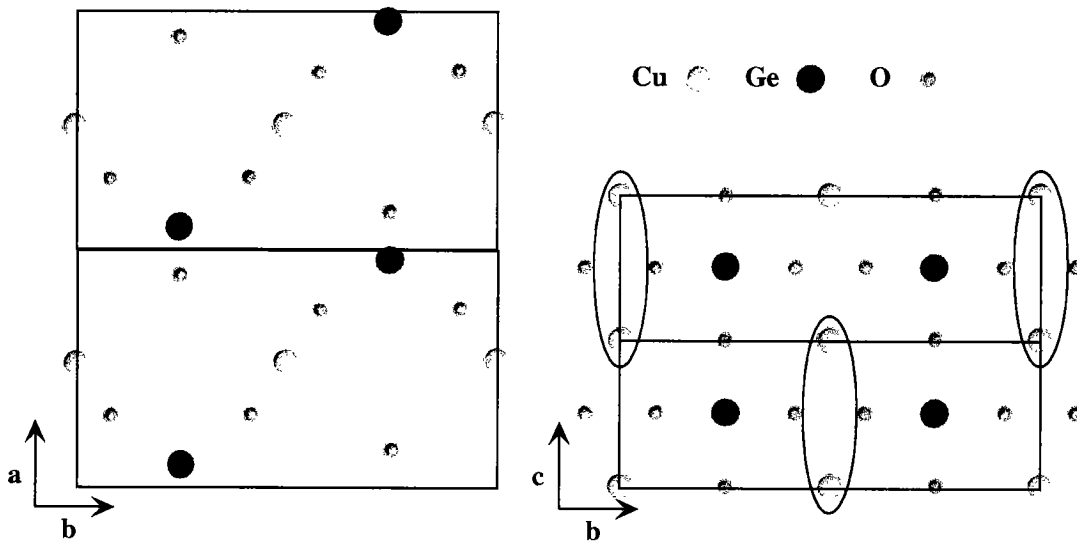


Figure 6.7: Low-temperature structure of pure CuGeO_3 . The rectangles show the unit cell for the high-temperature structure. Below T_{SP} , the cell becomes doubled along the a and c directions. The ellipses symbolise the Cu^{2+} dimers that are formed in the spin-Peierls state.

The spin chains are aligned along the c -axis, and the unit cell contains two unit formula. The lattice dimerisation leads to a doubling of the unit cell in the a and c direction. The Cu^{2+} dimers that are formed along the spin chain below T_{SP} are symbolised by ellipses in Fig. 6.7.

Theoretical background

The magnetic susceptibility $\chi(T)$ of a linear antiferromagnetic chain was calculated by Bonner and Fisher [75] and provided a good description of $\chi(T)$ for the organic SP compounds. However, the Bonner-Fisher model is not satisfactory for CuGeO_3 .

A significant improvement can be achieved in the analysis of the low temperature susceptibility [57, 63] if one uses the model proposed by Bulaevskii [76], where the 1D AF chains are coupled with the 3D phonon field. On the other hand, the high temperature susceptibility can be well reproduced by introducing temperature dependent alternating coupling and extending the spin interaction to next nearest neighbours in the model of Bulaevskii [77]. Nevertheless, this new model predicts the presence of a spin gap even above T_{SP} , which was never observed.

The coexistence of lattice dimerisation with antiferromagnetism in the doped CuGeO₃ compounds has been investigated theoretically with a model similar to the one of Bulaevskii. At $T=0$, the problem of a 1D-AF Heisenberg chain coupled to the lattice distortion, $u(x)$, is studied by using a **phase Hamiltonian** [78]:

$$\mathcal{H} = \int dx \left[\frac{1}{8} J c (\nabla\theta(x))^2 + \frac{\pi^2}{2} J c p(x)^2 - J\lambda \frac{u(x)}{c^2} \sin \theta(x) + \frac{2K}{c} u(x)^2 \right], \quad (6.9)$$

where J , c , λ and K are the exchange interaction, the lattice parameter, the spin-lattice coupling constant and the elastic constant, respectively. The position of the spins, $x = lc$ is treated as a continuous variable. The **quantum phase variable** $\theta(x)$ is divided into a classical component $\theta_{cl}(x)$ and a quantum fluctuating part $\hat{\theta}(x)$. The magnetisation at the site l , $\langle S_l^z \rangle$, is related to $\theta(x)$ via the relation:

$$\langle S_l^z \rangle = (-1)^l S(x) = (-1)^l e^{-\langle \hat{\theta}^2 \rangle / 2} \cos \theta_{cl}(x) \quad (6.10)$$

The observation of both SP and AF signatures can be consequently explained by considering a ground state where two long range order parameters, the lattice dimerisation $u(x)$ and the staggered magnetisation $S(x)$, coexist with a spatial variation: $u(x)$ is minimal near the doping centers where $S(x)$ takes its maximal value. A first experimental evidence of the spatial inhomogeneity for the magnetic moments was seen with muon spin rotation experiments on Si- and Zn-doped CuGeO₃ compounds [79].

The magnetic excitation spectrum has also been calculated assuming a periodic system with a unit cell containing $2n$ spins (i.e. an even number of spins) that are spatially varying [80]. The SP excitations are predicted to persist under low doping conditions, although they are broader than in the pure compound. Moreover, the SP gap ($\Delta_{SP} = 2.1\text{meV}$ in CuGeO₃) is shifted to lower values for the doped systems. For the AF spectrum, the spatial inhomogeneity of the magnetisation leads to the opening of an additional spin gap [80], in contrast to a 3D Néel state where the AF excitations are expected to be gapless. In the long wavelength limit the spin wave velocity is predicted to increase with doping, and the relaxation frequency Γ is proportional to γq^2 . γ is expected to decrease with increasing doping, as the AF ordering is stabilised by the introduction of impurities.

Inelastic neutron scattering experiments performed on Si-doped [67, 66] and Zn-doped [65] compounds near the magnetic zone center (0 1 1/2) have confirmed the above mentioned theoretical predictions for the low doping regime, where both order parameters coexist.

Magnetic intensity in absolute units

The determination of μ_{eff} for a given magnetic reflection can be performed by normalising the magnetic intensity with a selected Bragg reflection.

The elastic magnetic cross-section for a simple antiferromagnet is given by the following relation

$$\left(\frac{d\sigma}{d\Omega}\right)_{el} = (\gamma r_o)^2 N_m \frac{(2\pi)^3}{v_{om}} \sum_{\tau_m} |F_M(\tau_m)|^2 [1 - (\hat{\mathbf{Q}} \cdot \hat{\boldsymbol{\eta}})^2] \cdot \delta(\mathbf{Q} - \tau_m). \quad (6.11)$$

N_m and v_{om} are the number of magnetic unit cells and its volume, respectively; τ_m is a vector of the reciprocal magnetic lattice; $\hat{\mathbf{Q}}$ is the normalised scattering vector; $\hat{\boldsymbol{\eta}}$ is the unit vector along the spin direction. $F_M(\tau_m)$ is the magnetic structure factor:

$$F_M(\tau_m) = \frac{1}{2} g \langle S^n \rangle \sum_d \sigma_d F_d(\tau_m) e^{i\tau_m \cdot \mathbf{d}} e^{-W_d} \quad (6.12)$$

where $\langle S^n \rangle$ is the mean value of the spin component along $\hat{\boldsymbol{\eta}}$ and $F_d(\tau_m)$ is the magnetic form factor, and \sum_d extends over the ions in the magnetic unit cell. In the case of doped CuGeO₃, we have a doubling of the unit cell in the c direction, therefore $N_m = N/2$ and $v_{om} = 2 \cdot v_o$.

The experimental method consists of measuring rocking curves for the magnetic reflection as well as for a selected nuclear reference. The ratio of the integrated neutron intensities is related to the structure factors via the following formula:

$$\frac{P_M}{P_N} = \frac{[1 - (\hat{\boldsymbol{\tau}}_m \cdot \hat{\boldsymbol{\eta}})^2] \cdot |F_M(\tau_m)|^2 / \sin \theta_M}{|F_N(\tau_N)|^2 / \sin \theta_N}. \quad (6.13)$$

θ_N and θ_M are the nuclear and the magnetic scattering angles, respectively.

Spin-wave dispersion in Si-doped CuGeO₃

The starting point we use for modeling the AF spin excitations in CuGe_{1-x}Si_xO₃ is a Heisenberg Hamiltonian including two spin sublattices. According to the exchange parameters that have been determined for the pure CuGeO₃ compound, we assume that the nearest neighbours are oriented antiferromagnetically along the \mathbf{b} and \mathbf{c} directions, and ferromagnetically along \mathbf{a} . Within linear spin-wave theory, the dispersion relation for the magnetic excitations can be expressed as follows [8]:

$$\hbar\omega(\mathbf{q}) = S[(\mathcal{I}(\mathbf{q}) + \mathcal{J}(0) - \mathcal{I}(0) + D)^2 - (\mathcal{J}(\mathbf{q}))^2]^{1/2} \quad (6.14)$$

where $S = 1/2$, D accounts for the uniaxial anisotropy, $\mathcal{J}(\mathbf{q})$ and $\mathcal{I}(\mathbf{q})$ are the Fourier transforms of the exchange interaction between sublattices and within a sublattice, respectively:

$$\mathcal{J}(\mathbf{q}) = \sum_{\mathbf{r}} J(\mathbf{r})e^{-i\mathbf{q}\cdot\mathbf{r}} \quad (6.15)$$

$$\mathcal{I}(\mathbf{q}) = \sum_{\mathbf{R}} I(\mathbf{R})e^{-i\mathbf{q}\cdot\mathbf{R}} \quad (6.16)$$

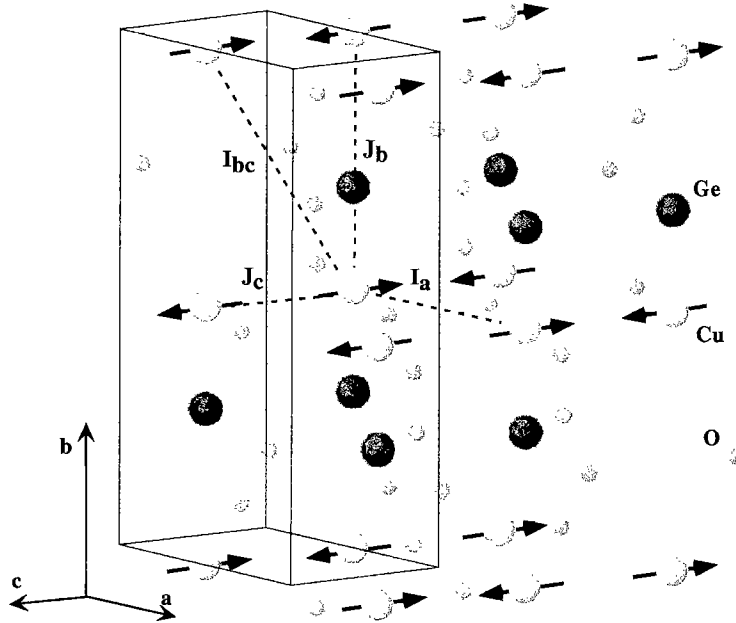


Figure 6.8: Chemical structure of CuGeO₃. The magnetic cell involves 4 Cu²⁺ ions. The arrows indicate the direction of the magnetic moments in the ordered phase.

Figure 6.8 shows the magnetic cell of CuGeO₃. According to the propagation vector $k_{AF} = (0 \ 1 \ 1/2)$ the spins are antiparallel along the $[0 \ 1 \ 0]$ and $[0 \ 0 \ 1]$ directions and parallel along $[1 \ 0 \ 0]$. For the analysis of the spin-wave dispersion of the doped compounds, we have assumed nearest neighbour interactions along the three principal crystallographic directions. The spin-wave dispersion is consequently given by

$$\begin{aligned} (\hbar\omega(q))^2 &= S^2 \left[(2I_a \cos(2\pi q_h) + 2J_b + 2J_c - 2I_a + D)^2 \right. \\ &\quad \left. - 4(J_b \cos(\pi q_k) + J_c \cos(2\pi q_l))^2 \right] \end{aligned} \quad (6.17)$$

where I_a , J_b and J_c are the nearest neighbours exchange interaction along a , b and c respectively.

6.2.3 Experimental details

The Si-doped CuGeO₃ single crystals have been grown using the floating zone method [81]. The impurity concentration was determined by means of inductively

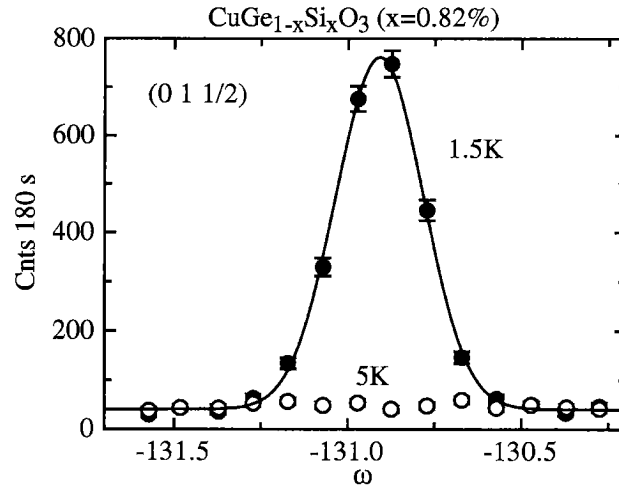


Figure 6.9: Profile for the magnetic superlattice peak (0 1 1/2) of the $x=0.82\%$ doped sample, at 1.5K. A similar measurement at 5K shows the absence of higher order contamination.

coupled plasma atomic emission spectroscopy (ICP-AES), with an accuracy of about 0.1%. The samples have been characterised by bulk susceptibility measurements which have been published elsewhere [82].

The neutron scattering experiments have been performed on the three-axis spectrometer for cold neutrons TASP, on a series of doped $\text{CuGe}_{1-x}\text{Si}_x\text{O}_3$ crystals ($0.7\% \leq x \leq 3.8\%$). For the diffraction experiments, the incident neutron wavevector was kept fixed at $k_i = 2.662 \text{ \AA}^{-1}$. The q -resolution was controlled by using $40' \text{--} 40' \text{--} 80'$ horizontal collimations, and higher-order neutrons have been suppressed by using a pyrolytic graphite filter (PG002). The samples have been oriented with the $(0kl)$ zone in the scattering plane, and mounted in an ILL-type cryostat, which achieves a base temperature of 1.5K.

For the inelastic neutron scattering experiments the three-axis spectrometer was operated in the constant k_f mode, with $k_f = 1.64 \text{ \AA}^{-1}$. The same PG002 filter was used. The measurements near the zone center were performed with flat analyser and $40' \text{--} 40' \text{--} 80'$ horizontal collimations. For higher scattering vectors, the collimations have been removed and the analyser was curved. The dispersions were measured along the principal symmetry axis of the crystal (a , b and c directions) near the (0 1 1/2) magnetic zone center, with $T=1.5\text{K}$.

The zero field and transverse field μSR measurements have been performed on the spectrometers GPS and LTF. The polarisation of the incident muon beam was parallel to the a -axis of the sample. In transverse field experiments, the external field ($H_{ext} = 50\text{G}$) was applied perpendicular to the initial muon polarisation.

6.2.4 Results

Neutron diffraction

A typical profile of an antiferromagnetic superlattice peak is shown in Fig. 6.9 for the 0.82% sample. The temperature dependence of the maximum intensity is presented in Fig. 6.10. In order to confirm the onset of the SP dimerisation in the low doping regime, the reflection $(1/2 \ 3 \ 1/2)$ was also measured. The magnetic intensity has been fitted with the following equation [64]:

$$I(T) = N \int_T^\infty \left(\frac{T'_N - T}{T'_N}\right)^{2\beta} \exp\left[-\frac{(T'_N - T_N)^2}{2\Delta T_N^2}\right] dT'_N + BG \quad (6.18)$$

which describes the critical behaviour of the magnetic intensity near the AF transition, weighted with a Gaussian distribution for T_N that accounts for inhomogeneities in the sample. N is a normalisation constant, β the critical exponent and BG the nonmagnetic background contribution. The parameters that characterise the AF phase in the doped compounds are listed in Table 6.1. The critical exponent β remains almost constant over the whole diagram, with an average value of about 0.20 ± 0.04 , similar to that observed in Zn-doped crystals [64]. The inhomogeneity in the concentration provides a ΔT_N of about $0.3 \pm 0.05\text{K}$. The temperature dependence of the SP peak shown in Fig. 6.9 was fitted with a function similar to the one of Eq. 6.18 (see Ref. [70] for details).

Table 6.1: Physical parameters characterising the AF transition in $\text{CuGe}_{1-x}\text{Si}_x\text{O}_3$ as a function of x . The ordering temperature T_N , its distribution ΔT_N and the critical exponents β have been obtained using Eq. 6.18 for fitting the temperature dependence of the superlattice peaks.

x (%)	$T_N(\text{K})$	$\Delta T_N(\text{K})$	β
0.7 ± 0.02	2.02 ± 0.07	0.28 ± 0.07	0.14 ± 0.04
0.82 ± 0.01	3.90 ± 0.12	0.59 ± 0.06	0.14 ± 0.03
1.11 ± 0.03	4.13 ± 0.06	0.45 ± 0.01	0.22 ± 0.02
1.23 ± 0.02	4.31 ± 0.09	0.42 ± 0.06	0.20 ± 0.03
1.71 ± 0.03	4.80 ± 0.03	0.23 ± 0.02	0.20 ± 0.01
2.15 ± 0.1	4.84 ± 0.01	0.183 ± 0.011	0.218 ± 0.005
2.38 ± 0.07	4.55 ± 0.03	0.21 ± 0.03	0.21 ± 0.02
2.54 ± 0.08	4.72 ± 0.08	0.27 ± 0.03	0.20 ± 0.02
3.8 ± 0.1	4.38 ± 0.02	0.34 ± 0.01	0.19 ± 0.01

The effective magnetic moments μ_{eff} have been calculated by normalising the magnetic intensity at the saturation value with the nuclear structure factor of the $(0 \ 2 \ 1)$ reflection, and corrected for the magnetic form factor of the free Cu^{2+} ion [83]. We emphasise that the neutron diffraction technique is a non local probe, and hence does provide a macroscopic order parameter that is averaged over the whole volume of the sample.

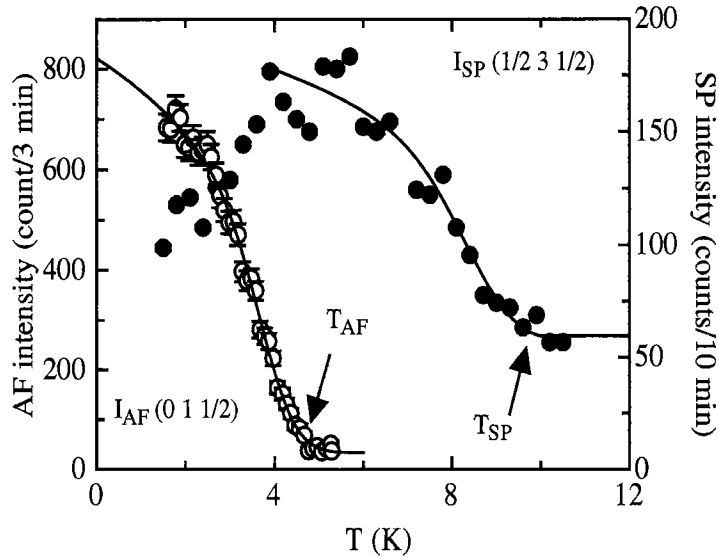


Figure 6.10: Temperature dependence of the $(0\ 1\ 1/2)$ antiferromagnetic and $(1/2\ 3\ 1/2)$ spin-Peierls superlattice peaks in the 0.82% Si-doped CuGeO_3 single crystal. The solid line for $(0\ 1\ 1/2)$ results from a fit according to Eq. 6.18. A similar function was used for the SP peak.

As a next step, selected samples (0.82%, 1.7%, 2.38% and 3.8%) belonging to the series of single crystals measured with neutrons have been investigated by muon spin rotation spectroscopy in the three temperature regions that have been determined with neutron and susceptibility measurements, according to the experimental T - x diagram presented in Fig. 6.11. The values obtained from the various techniques are found to be in good agreement with each other, indicating that the muon and the neutrons observe a magnetic ordering at the same transition temperature. The observation of the SP dimerisation in susceptibility data for the samples in the low doping regime is also confirmed by neutrons. The discrepancy between both methods is due to the fact that the SP superlattice peak that is measured with neutrons becomes extremely small while approaching the critical concentration. Furthermore, we emphasise that T_{SP} is not observed above $x=1.2\%$.

μSR results

In the paramagnetic phase, the zero-field muon spectra have been fitted with the Kubo-Toyabe function which accounts for the muon depolarisation originating from the nuclear moments (the depolarisation rate is of the order of 0.08 MHz). By lowering the temperature, in the low doping regime, the muon spectrum can still be explained by the same relaxation function [see Fig. 6.12 (a)], as it was observed for pure CuGeO_3 [84]. In the magnetically ordered phase, below T_N , the muon depolarisation $P_\mu(t)$ in zero field was analysed over the whole doping regime with the following function [79] [see Fig. 6.12 (b)]:

$$P_\mu(t) = A_{rix} \exp(-\Delta t) + A_{osc} \exp(-\Gamma t) \cdot \cos(2\pi\nu t + \phi). \quad (6.19)$$

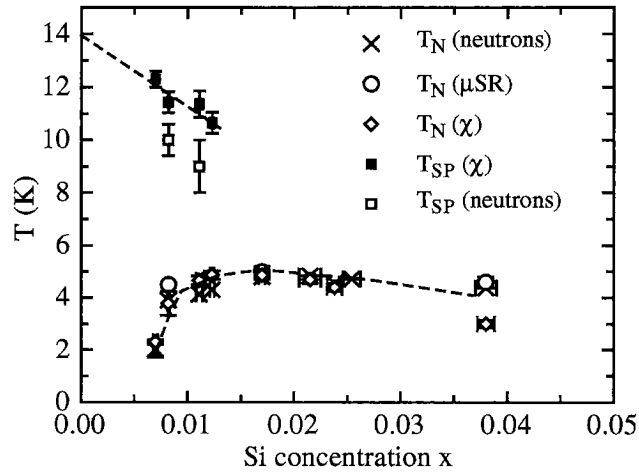


Figure 6.11: Temperature-concentration phase diagram of the Si-doped CuGeO_3 . The AF ordering temperature T_N and the spin-Peierls transition temperature T_{SP} have been determined by bulk susceptibility [82] and neutron diffraction experiments. The T_N determined by μSR measurements are also reported. The dashed lines are a guide to the eye.

The first term in Eq. 6.19 describes a non-precessing part of the muon signal, which relaxes at a rate Δ , whereas the second term reflects a precessing part of the muon polarisation, where Γ is the depolarisation rate and ϕ the initial phase shift. The total observed amplitude ($A_{rlx} + A_{osc}$) is significantly lower than the total amplitude observed above T_N , indicating that part of the muon ensemble is depolarised within the dead time of the spectrometer (*i.e.* a depolarisation rate higher than ca. 150 MHz).

According to the T-x diagram shown in Fig. 6.11, the emergence at low temperature of the precessing signal (A_{osc}) in zero-field is attributed to the ordering of the Cu^{2+} moments near the doping centers. In this vein, the frequency ν , which is proportional to the magnetic field B_μ at the muon site, mirrors the static ordering of the moments. The relaxing component in Eq. 6.19 is ascribed to sample regions where no coherent static magnetism is present. However, the similar temperature dependence of Δ and ν (see Fig. 6.14 and the inset of Fig. 6.15) indicates that these regions have reduced dimensions, leading to a detectable influence of the ordered neighbouring regions on the field distribution Δ/γ_μ (where γ_μ is the gyromagnetic ratio of the muon) at the muon sites. This supports the idea that there is no *macroscopic* phase separation in the samples over the whole doping range, similarly to what was observed by Kojima et al. for Si- and Zn-doped CuGeO_3 compounds in the low doping regime [79]. Therefore, and similarly to the parameter ν , the parameter Δ can be taken as a measure of the static ordered moments. Since $A_{rlx} \gg A_{osc}$ the parameter Δ appears to be better determined than ν and consequently Δ will be utilised in the following discussion as a measure of the static moment.

The transverse field measurements could be analysed with a function similar to the one for zero field experiments (see Eq. 6.19). For a sample containing a non-magnetic phase, one would expect the spin of the muon to precess according to the

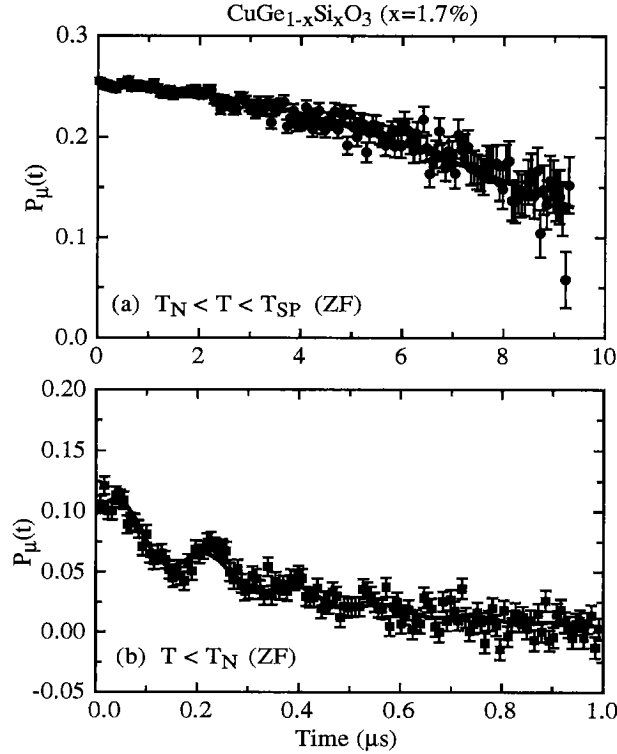


Figure 6.12: Muon depolarisation spectra taken in the zero-field mode at $T=8\text{K}$ (a) and $T=2\text{K}$ (b) for the $x=1.7\%$ sample. The data above T_N (4.8K) are fitted with the Kubo-Toyabe function. Below T_N , the muon depolarisation $P_\mu(t)$ is analysed with Eq. 6.19.

external applied field, and the depolarisation rate to be small [see Fig. 6.13 (a)]. However the transverse field data do show a significant depolarisation as presented in Fig. 6.13 (b). This is an indication that below T_N the muon implanted in the region where the dimerisation is maximal is influenced by the dipolar field arising from the magnetically ordered regions.

The doping dependence of the relaxation rate Δ , extrapolated at the saturation value ($T=0$) is shown in Fig. 6.15. The dependence upon Si-doping is almost constant within the precision of the experimental values. Δ exhibits however an increase above $x \approx 2.4\%$. According to the direct relation between Δ and ν , this behaviour indicates that within the doping range that has been investigated the local magnetic field at the muon sites increases slightly with increasing doping.

Figure 6.16 shows the evolution of the normalised amplitudes \hat{A}_{rlx} (dark grey area) and \hat{A}_{osc} (white area), as a function of Si concentration. The amplitudes have been normalised with respect to the total muon asymmetry A_{tot} , that was determined in the paramagnetic phase [see Fig. 6.13 (a)]. We obtain that the amplitude corresponding to the magnetically ordered phase, \hat{A}_{osc} , represents about 10% of A_{tot} . The relaxing part \hat{A}_{rlx} lies on the other hand between 40% and 60%. The part of A_{tot} (light grey area in Fig. 6.16) that could not be detected ($\approx 40\%$) will be discussed below.

In order to compare the local magnetic properties of the doped samples, as provided

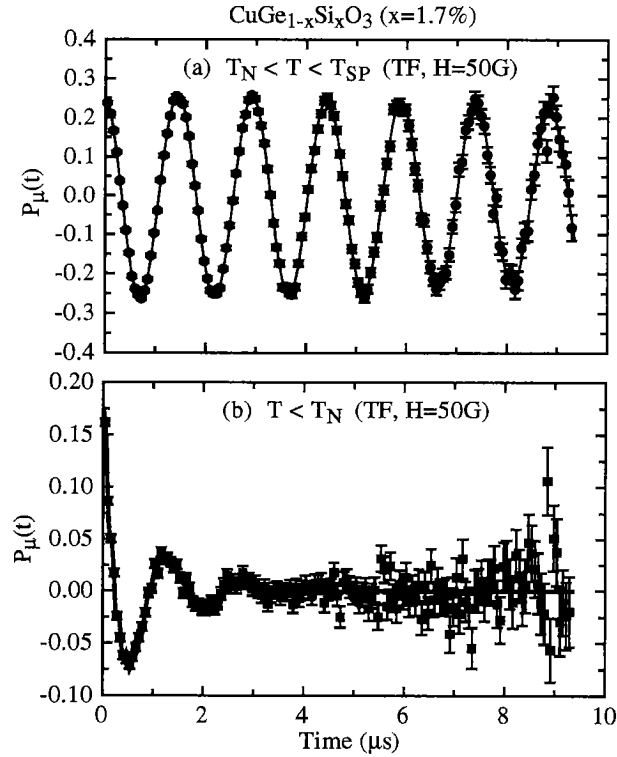


Figure 6.13: Transverse field muon depolarisation spectra in the $x=1.7\%$ sample. Figure (a) shows the paramagnetic case ($T=8\text{K} > T_N$), where the spin of the muon oscillates with the external field and do not depolarise significantly. The total asymmetry A_{tot} of the muon signal is determined in these experimental conditions. Below T_N (b), the signal is strongly depolarised ($T=2\text{K}$).

by the muons, with the macroscopic order parameter measured with neutrons, we use the quantity $\Delta \cdot \hat{A}_{osc}$. In this product, the local magnetic moment (proportional to Δ) is hence weighted with the volume fraction (\hat{A}_{osc}) of magnetised regions present in the sample.

The dependence of the AF order parameter μ_{eff} as a function of concentration is shown in Fig. 6.17, as obtained by both neutron diffraction and zero-field μSR methods. μ_{eff} is seen to increase with the doping concentration, reaches a maximum at $x_c=1.7\%$, where the SP signal is not observed anymore (see Fig. 6.11).

Inelastic neutron experiments

The magnetic excitations have been measured on the three samples ($x=2.15\%$, $x=2.54\%$ and $x=3.8\%$) that have a reasonable size (about $2 \times 5 \times 10 \text{ mm}^3$) for inelastic neutron experiments.

As a first step, the measurements have been performed near the magnetic zone center $(0 \ 1 \ 1/2)$ in the $[0 \ 1 \ 0]$ direction, in order to observe the doping evolution of the AF spin gap. As an example, typical scans are shown in Fig. 6.18 for the $x=2.54\%$ sample. The gap is visible in Fig. 6.18 (a), at about 0.16 meV . A second

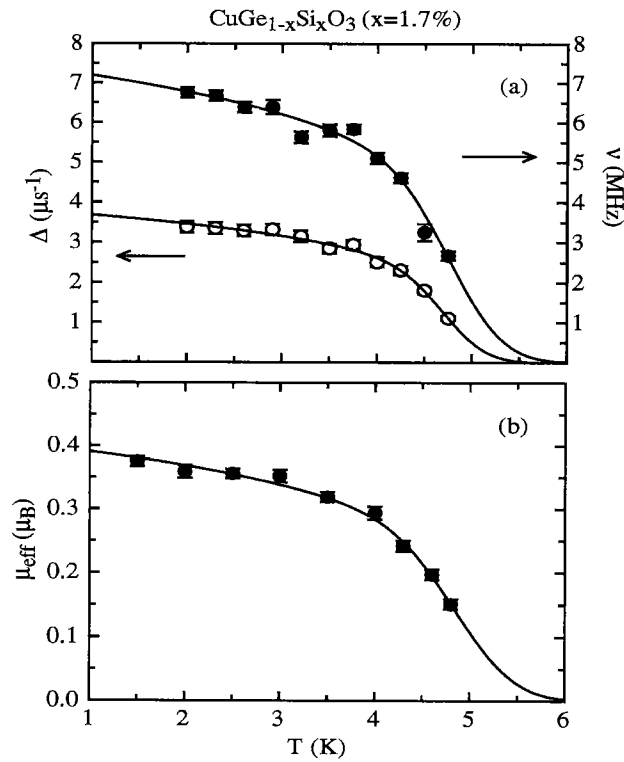


Figure 6.14: Temperature dependence of the relaxation rate Δ and the precessing frequency ν for the 1.7% doped single crystal measured in zero-field μSR (a). The magnetic moment measured by means of neutron diffraction for the same sample is shown in (b). The solid lines are fits according to Eq. 6.18.

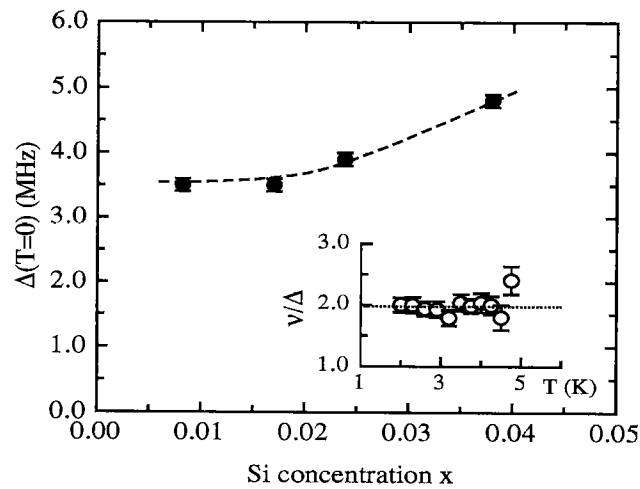


Figure 6.15: Muon relaxation rate Δ extrapolated to $T=0$, plotted as a function of doping. The value is proportional to the local magnetic moment at the muon site (see inset). The dashed line is a guide to the eyes. The inset shows the ratio ν/Δ for the $x=1.7\%$ sample, confirming the proportionality between both parameters ($\nu/\Delta \approx 2$, as indicated by the dotted line).

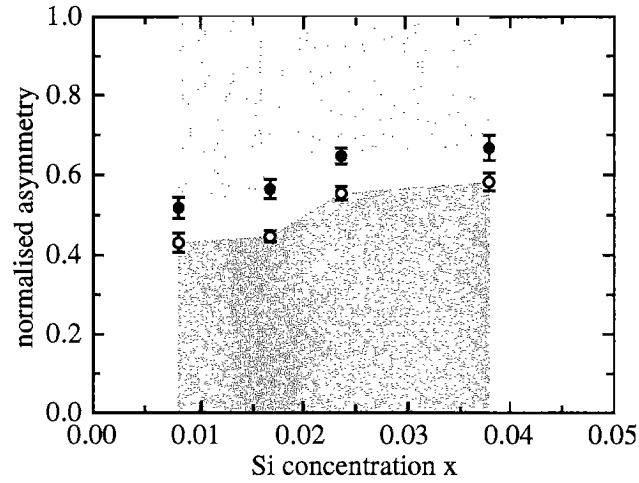


Figure 6.16: The normalised amplitudes of the muon depolarisation \hat{A}_{rlx} (dark grey area) and \hat{A}_{osc} (white area), obtained from Eq. 6.19, as a function of Si doping. The quantities have been normalised to the total muon asymmetry A_{tot} . The light grey region refers to lost part of the muon signal (i.e. $1 - \hat{A}_{rlx} - \hat{A}_{osc}$).

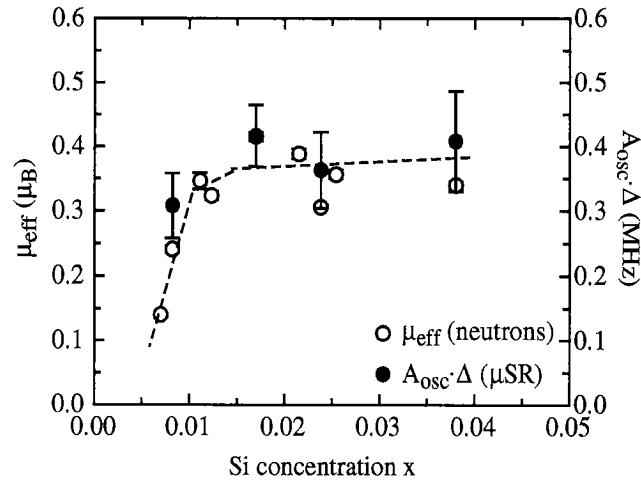


Figure 6.17: The order parameter μ_{eff} as a function of Si doping x measured with the neutron diffraction method (open circles). The effective magnetic moment determined by μSR (explained in the text) is also shown (solid circles). The dashed line is a guide to the eyes.

peak is seen at 0.5 meV, albeit weak, due to the geometrical anisotropy because of the orthorhombic symmetry. This double peak feature was already observed in other experiments [67, 85] and is visible only at small q -values. The large intensity of the elastic line is due to the $[0\ 1\ 1/2]$ magnetic Bragg reflection. Figure 6.18 (b) shows a magnetic excitation along the $[0\ 1\ 0]$ direction. The elastic line consists only of incoherent scattering and indicates the experimental energy resolution.

The spin-wave dispersions measured in the $[0\ 1\ 0]$ direction near the zone center are gathered in Fig. 6.19. We observe that within the accuracy of the measurements the curves do not depend on the doping concentration. The dispersion can be

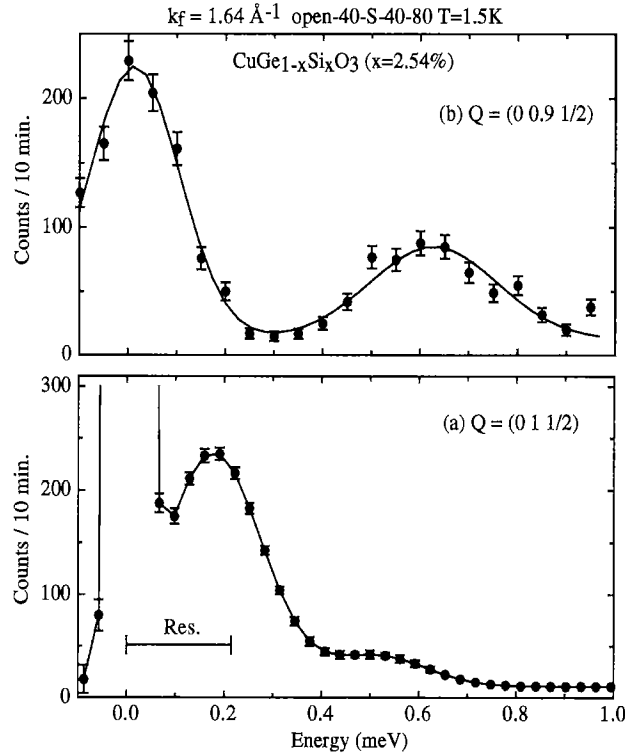


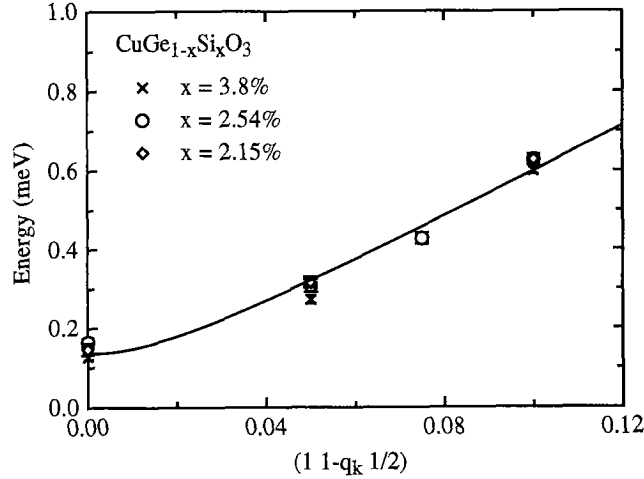
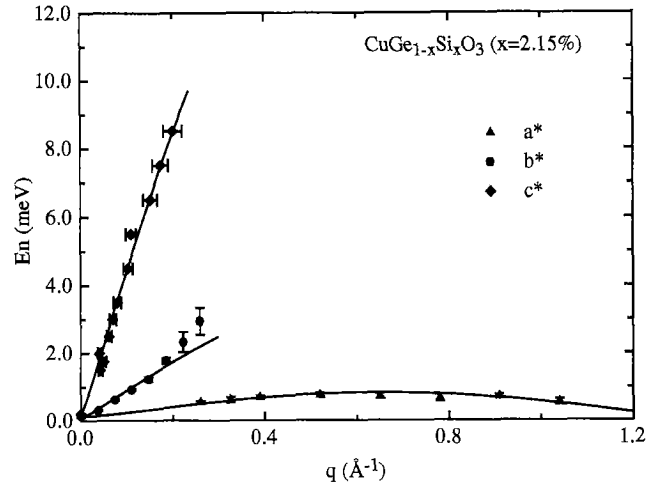
Figure 6.18: Constant- q scans at the magnetic zone center $(0\ 1\ 1/2)$ (a). The intensity at the elastic line arises from the magnetic Bragg reflection. The linewidth is smaller than the actual resolution (indicated in the graph) because of coherence effects. An inelastic scan in the $[0\ 1\ 0]$ direction is shown in (b).

reproduced by the expression $E(q) = \sqrt{\Delta^2 + (cq)^2}$. The fit yields an average gap of 0.14 ± 0.02 meV and an average spin-wave velocity of 7.8 ± 0.1 meV \AA^{-1} . These values are comparable with those observed in a 3.0% Si-doped sample [67].

Furthermore, a similar value for the gap was measured in a low doped compound [66], where the lattice dimerisation is present. These results indicate that the small gap, which reflects the magnitude of the axial anisotropy, does not change while going from the D-AF to the U-AF phase.

In a second step, the spin-wave dispersion of two doped single crystals ($x=2.15\%$ and $x=3.8\%$) was measured along the three principal crystallographic axis. Figure 6.20 summarises the dispersion curves that were measured on the $x=2.15\%$ sample.

The model that was used is given in Section 6.2.2, where the nearest neighbour exchange interactions are taken into account. The fit has yielded $J_c = 15.0 \pm 0.2$ meV, $J_b = 0.28 \pm 0.02$ meV and $I_a = -0.012 \pm 0.003$ meV. For the anisotropy parameter we have obtained $D = 1.2 \pm 0.5$ μeV . This latter value is small but necessary for the opening of the gap that is shown in Fig. 6.19. Finally, we show in Fig 6.21 a comparison of the spin-wave dispersion along the b^* and the c^* symmetry axis for the two samples. In the wavevector range that is experimentally investigated, no significant discrepancy is observed between the two different concentrations.

Figure 6.19: Spin-wave dispersion along the $[0\ 1\ 0]$ direction.Figure 6.20: Dispersion of the magnetic excitations in the doped $\text{CuGe}_{1-x}\text{Si}_x\text{O}_3$ ($x=2.15\%$) along the principal crystallographic axis at $T=1.5\text{K}$. The measurements were performed near the magnetic zone center $(0\ 1\ 1/2)$. The solid line is a fit using Eq. 6.17 based on a Heisenberg model.

6.2.5 Discussion

Static properties

The agreement between neutron and μSR results (see Figs. 6.11 and 6.17) allows to associate the precessing signal, referred to A_{osc} , with the D-AF phase in the low doping regime, and with the U-AF phase in the high doping regime.

The purely relaxing signal, A_{rlx} , is attributed, for $x \leq 1.23\%$, to the regions where the lattice dimerisation is maximal. However, for higher doping concentrations, this amplitude does not disappear. It is thought to arise from an increase of the static magnetic disorder that is induced by high doping.

As the sum of \hat{A}_{rlx} and \hat{A}_{osc} constitutes not more than 60% of the total muon asym-

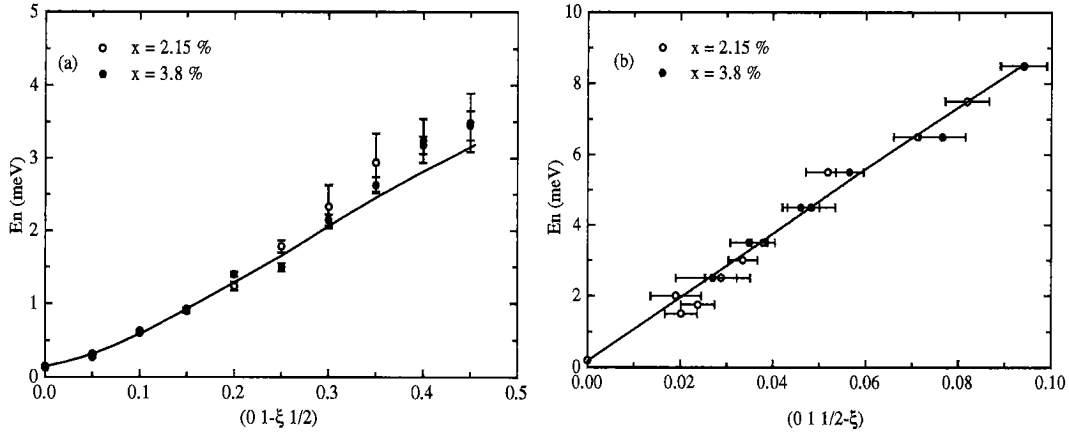


Figure 6.21: Spin-wave dispersion along b^* (a) and c^* (b) for two single crystals with different doping. The solid line is a fit using Eq. 6.17, similar to the case of Fig. 6.20, but taking into account the experimental values for both samples simultaneously.

metry in the whole investigated doping regime, we may attribute the loss of signal to the boundary between the AF regions and the dimerised regions where a rapid spatial variation of the magnetisation gives rise to large field gradient and therefore leads to a depolarisation rate too fast to be observed by the μSR spectrometer. However, the neutrons are sensitive to these boundary regions that contribute to the intensity of the AF peaks.

The μSR measurements have shown on the other hand that the muon signal described by $A_{r|x}$ is influenced by the dipolar fields of the magnetically ordered regions and still undergoes a depolarisation. This is a clear sign that the domains contributing to the purely relaxing muon signal have a limited size. Considering the magnitude of the magnetic moments that are determined by neutron diffraction, 0.1 to 0.4 μ_B , the maximal distance over which the muon still sees a dipolar field is estimated to be $\approx 15 \text{ \AA}$. By considering an homogeneous distribution of impurities along the spin chains, this distance corresponds to ≈ 5 lattice units in both directions on each side of the muon site. The present measurements confirm the spatial inhomogeneity of the magnetic moments that was predicted theoretically [80, 86]. The maximum in the order parameter μ_{eff} that was observed by neutron diffraction at $x_c=1.7\%$ refers to a macroscopic value. In other words, the magnetic moment determined by this technique is averaged over the whole volume of the sample. The results provided by μSR indicate that the volume fraction of the magnetically ordered regions as well as the boundary regions varies upon doping. On the other hand, no anomaly is seen in the local magnetic moment near the critical value x_c . We suggest therefore that the variation of the macroscopic AF order parameter upon doping is controlled by a variation in the volume fraction of magnetic domains rather than by a drastic change of the magnetic moments.

Dynamical properties

The exchange parameters that have been extracted from the experimental spin-wave dispersions in doped CuGeO₃ do not differ much from the coupling constants determined in pure CuGeO₃. Indeed, the intrachain coupling $J_c \approx 15$ meV remains close to the value $\pi J_c/2 = 16.3$ meV, as obtained by Nishi et al. [62]. The ratio $J_b/J_c \approx 0.02$, which is an indication of the dimensionality of the system, is thus approximately reduced by a factor 5, when compared with the pure compound. However, the measurements along the b^* direction could not be extended to reasonably high q -values, due to experimental restrictions in the neutron intensity.

The similarities in the dispersion for both samples seem to indicate that the exchange parameters are independent on the doping concentration, at least in the doping regime where the lattice dimerisation does not take place anymore. It would be of interest to check this hypothesis below the critical concentration. However, on the basis of the information provided by the neutron diffraction and μ SR results, one may argue that only the magnetically ordered regions contribute to the inelastic signal. The variation of the doping concentration is presumed to modify the volume fraction and not the intrinsic properties of this latter phase.

6.2.6 Intermediate conclusion

The origin of the various magnetic contributions observed in the Si-doped CuGeO₃ by means of susceptibility measurements and neutron diffraction have been clarified via complementary investigation performed with μ SR spectroscopy. Indeed, the μ SR results have revealed that the regions which contribute to the antiferromagnetic and lattice dimerisation peaks observed by neutron and susceptibility in the Si-doped CuGeO₃ have a typical size of 5 lattice units along the spin chains. Furthermore, the doping variation of the magnetic moment measured with neutrons could be explained via the evolution of the volume fraction attributed to magnetically ordered regions near the impurity centers.

The spin dynamics of the Si-doped CuGeO₃ was investigated by means of inelastic neutron scattering experiments. The analysis of the spectrum near the zone center has revealed that the AF spin gap and the long wavelength spin fluctuations do not depend on the doping concentration, in the range that was investigated. Moreover this behaviour is common in the excitation spectrum of both dimerised and uniform antiferromagnetic phases.

The dispersion of the magnetic fluctuations was measured along the three main symmetry directions for selected samples. The interchain exchange parameters is comparable with the one of CuGeO₃. The coupling constants J_a and J_b are found to be smaller than in the undoped compound. The ratio between interchain and intrachain coupling is one order of magnitude larger than or the standard quasi one-dimensional antiferromagnets KCuF₃, Sr₂CuO₃ and Ca₂CuO₃. The AF phase which is induced by doping is therefore not strictly speaking quasi one-dimensional. The anisotropy in the exchange parameters can however account for the spin gap associated with the AF phase in both doping regimes.

Chapter 7

Concluding Remarks

Le peu que je sais, c'est à mon ignorance que je le dois.
Sacha Guitry

The characteristics of the electrons that play a role in magnetism lead to a classification of the magnetically ordered systems into mutually non-exclusive categories: itinerant or localised spin systems; weak or strong magnets; isotropic or anisotropic systems. In this thesis, we have focused our attention on the static and dynamical properties of several compounds, each belonging to a specific category. The aim was to emphasise the similarities and the differences that may arise among the various classes of magnets.

Chapter 5 is devoted to the critical dynamics of itinerant magnets. As a first step, we have performed an extensive investigation of the spin dynamics of the weakly itinerant magnet Ni_3Al . **The results have revealed that the critical fluctuations must be taken into account in an itinerant model of magnetism, similarly to what occurs in a model based on localised spins [87].** Furthermore the calculation of the scaling parameter W_- has evidenced that **the dynamics of weak itinerant ferromagnets near the phase transition is similar to the one of itinerant magnets (Co, Fe and Ni) as well as localised magnets (EuS and EuO).**

In the second part of Chapter 5 we have studied the critical scattering of Ni, which is an itinerant magnet. The predicted crossover to a $1/Q$ divergence of the longitudinal magnetic susceptibility χ_{\parallel} could not be observed. The underlying reasons are connected with the physics of the system as well as the current status of polarisation analysis in small angle neutron scattering. However, the experimental conditions that are required for the investigation of χ_{\parallel} have allowed to reach a Q -range where the effect of the dipolar forces could be demonstrated. The analysis of the data has shown that **the dipolar wavevector q_D in the ordered phase is comparable to q_d which characterises the dipolar regime in the paramagnetic phase.**

Chapter 6 was devoted to the investigation of magnetism in systems with localised spins.

In the Heisenberg ferromagnet EuS, we have shown that **local spin fluctuations can persist at temperatures that are extremely high when compared with the exchange parameters**. However, the intensity of the excitations is reduced by increasing temperature and limited to wavevectors near to the zone boundary, in contrast to the itinerant magnets where the long wavelength spin fluctuations are thermally enhanced.

Finally, we have investigated bond doping effects on the spin-Peierls compound CuGeO_3 . The introduction of Si impurities was observed to progressively suppress the lattice dimerisation and to generate an antiferromagnetic ordering of the Cu^{2+} ions. As a first step, the antiferromagnetic phase was characterised by neutron diffraction. The local properties of the doped compound were investigated by means of muon spin rotation spectroscopy. The complementary information of both techniques have provided a detailed insight in the distribution of the two phases present in the samples. Furthermore, **the spatial inhomogeneities that are revealed by μSR could explain the variation upon doping of the order parameter μ_{eff} that is measured with neutrons**.

Secondly, the spin dynamics of the Si-doped CuGeO_3 was investigated by means of inelastic neutron scattering. As a major result, **the AF spin gap and the exchange interaction J_α do not depend upon the doping concentration**, as far as the AF ordering is observed. Moreover **the values of the J_α are similar to the exchange integrals measured in the pure spin-Peierls compound**. On the basis of the information we obtained from the static properties of the doped compound, this result can be interpreted as follows: the magnetic properties of the AF phase are not modified intrinsically by the variation of the doping concentration. This latter has only an effect on the volume fraction of the AF and dimerised phases. Therefore the suppression of the lattice dimerisation does not play a significant role in the spin dynamics of AF phase that appears in the Si-doped CuGeO_3 compound.

Bibliography

- [1] E.P. Wohlfarth, *J. Magn. and Magn. Mat.* **7**, 113 (1978).
- [2] P. Fazekas in *Lecture Notes on Electron Correlation and Magnetism*, Series in Modern Condensed Matter Physics. Vol. 5 (1999).
- [3] Spin waves and magnetic excitations, A.S. Borovik-Romanov and S.K. Sinha, Elsevier Science Publishers B.V. 1988.
- [4] T. Moriya, *Spin Fluctuations in Itinerant Electron Magnetism*, Springer, Berlin, 1985: and references therein.
- [5] S. W. Lovesey and R. A. Meserve, *J. Phys. C* **6**, 79 (1973).
- [6] F.D.M. Haldane, *Phys. Rev. Lett.* **93**, 464 (1983).
- [7] J.W. Bray et al., *Phys. Rev. Lett.* **35**, 744 (1975).
- [8] S.W. Lovesey, *Theory of neutron scattering from condensed matter*, Oxford Science Publications 1984.
- [9] G.L. Squires, *Introduction to the theory of Thermal neutron scattering*, Cambridge University Press 1978.
- [10] Callen and Welton, *Phys. Rev.* **83**, 34 (1951).
- [11] A. Schenck, *Muon Spin Rotation Spectroscopy*, 1985.
- [12] R. Kubo and T. Toyabe, *Magnetic Resonance and Relaxation*, ed. R. Blinc, 1967.
- [13] S.-K. Ma, *Modern Theory of Critical Phenomena*, Frontiers in Physics, 1982.
- [14] L.P. Kadanoff, *Physics* **2**, 263 (1966).
- [15] B.I. Halperin and P.C. Hohenberg, *Phys. Rev.* **177**, 952 (1969).
- [16] D.S. Ritchie and M.E. Fisher, *Phys. Rev. B* **5**, 2668 (1972).
- [17] B.I. Halperin and P.C. Hohenberg, *Phys. Rev. Lett.* **19**, 700 (1967).
- [18] J. Goldstone, *Nuovo Cimento* **19**, 154 (1961).

- [19] G.F. Mazenko, *Phys. Rev. B* **14**, 3933 (1976).
- [20] P. Résibois, C. Piette, *Phys. Rev. Lett.* **24**, 514 (1970).
- [21] A. Aharony and M.E. Fisher, *Phys. Rev. B* **8**, 3323 (1973).
- [22] E. Frey, F. Schwabl, *Z. Phys. B* **71**, 355 (1988).
- [23] H. Schinz, F. Schwabl, *Phys. Rev. B* **57**, 8456 (1998).
- [24] H. Schinz, F. Schwabl, *Phys. Rev. B* **57**, 8438 (1998).
- [25] T. Holstein and H. Primakoff, *Phys. Rev.* **58**, 1098 (1940).
- [26] E.C. Stoner, *Proc. Roy. Soc. A* **165**, 372 (1938).
- [27] T. Moriya and A. Kawabata, *J. Phys. Soc. Jpn.* **34**, 639 (1973).
- [28] G.G. Lonzarich, L. Taillefer, *J. Phys. C* **18**, 4339 (1985).
- [29] Y. Ishikawa, G. Shirane, J.A. Tarvin, *Phys. Rev. B* **16**, 4956 (1977).
- [30] N.R. Bernhoeft, G.G. Lonzarich, P.W. Mitchell, D. McK. Paul, *Phys. Rev. B* **18**, 422 (1983).
- [31] N.R. Bernhoeft, G.G. Lonzarich, D. McK. Paul, P.W. Mitchell, *Physica B* **136**, 443 (1986).
- [32] Dr. T. Chatterji is gratefully acknowledged for the loan of the Ni₃Al single crystal.
- [33] F.R. de Boer, C.J. Schinkel, J. Biesterbos, S. Proost, *J. Appl. Phys.* **40**, 1049 (1969).
- [34] G.G. Lonzarich, *J. Magn. and Magn. Mat.* **54**, 612 (1986).
- [35] Y. Ishikawa, Y. Noda, C. Fincher and G. Shirane, *Phys. Rev. B* **31**, 5884 (1985).
- [36] H. Hiraka, Y. Endoh and K. Yamada, *J. Phys. Soc. Jpn.* **66**, 818 (1997).
- [37] M. Kohgi, Y. Endoh, Y. Ishikawa, H. Yoshizawa, and G. Shirane, *Phys. Rev. B* **34**, 1762 (1986).
- [38] P. Böni, J.L. Martinez and J.M. Tranquada, *Phys. Rev. B* **43**, 575 (1991).
- [39] P. Böni, H.A. Mook, J.L. Martinez and G. Shirane, *Phys. Rev. B* **47**, 3175 (1993).
- [40] T. Moriya and T. Takimoto, *J. Phys. Soc. Jpn.* **64**, 960 (1995).

- [41] S.M. Hayden et al., *Phys. Rev. Lett.* **84**, 999 (2000).
- [42] H. Schinz, F. Schwabl, *Phys. Rev. B* **57**, 8430 (1998).
- [43] R. Anders and K. Stierstadt, *Solid State Commun.* **39**, 185 (1981).
- [44] J. Cangle and G.M. Goddman, *Proc. R. Soc. London Ser. A* **321** 477 (1971).
- [45] L. Passel, O.W. Dietrich and J. Als-Nielsen, *Phys. Rev. B* **14**, 4897 (1976).
- [46] J. Als-Nielsen, O.W. Dietrich and L. Passel, *Phys. Rev. B* **14**, 4908 (1976).
- [47] O.W. Dietrich, J. Als-Nielsen and L. Passel, *Phys. Rev. B* **14**, 4923 (1976).
- [48] H.G. Bohn, A. Kollmar, W. Zinn, *Phys. Rev. B* **30**, 6504 (1984).
- [49] H.G. Bohn, W. Zinn, B. Dorner and A. Kollmar, *Phys. Rev. B* **22**, 5447 (1980).

- [50] R. Folk and H. Iro, *Phys. Rev. B* **34**, 6571 (1986).
- [51] B. S. Shastry, D.M. Edwards and A. P. Young, *J. Phys. C* **14**, L665 (1981).
- [52] A. P. Young and B. S. Shastry, *J. Phys. C* **15**, 4547 (1982).
- [53] P. Böni and G. Shirane, *Phys. Rev. B* **33**, 3012 (1986).
- [54] S. W. Lovesey and E. Balcar, *J. Phys. C* **6**, 1253 (1994).
- [55] P. Böni, G. Shirane, H.G. Bohn and W. Zinn, *J. Appl. Phys.* **61**, 3397 (1987).
- [56] Dr. H.A. Graf (HMI Berlin) is gratefully acknowledged for having provided the source code.
- [57] M. Hase, I. Terasaki and K. Uchinokura, *Phys. Rev. Lett.* **70**, 3651 (1993).
- [58] I.S. Jacobs et al., *Phys. Rev. B* **14**, 3036 (1976).
- [59] S. Huizinga et al., *Phys. Rev. B* **19**, 4723 (1979).
- [60] M. Hase, I. Terasaki, Y. Sasago, K. Uchinokura and H. Obara *Phys. Rev. Lett.* **71**, 4059 (1993).
- [61] O. Fujita, J. Akimitsu, M. Nishi and K. Kakurai, *Phys. Rev. Lett.* **74**, 1677 (1995).
- [62] M. Nishi, O. Fujita and J. Akimitsu, *Phys. Rev. B* **50**, 6508 (1994).
- [63] S. Coad et al., *J. Phys. Condens. Matter* **8**, 6251 (1996).
- [64] M. Hase et al., *J. Phys. Soc. Jpn.* **65**, 1392 (1996).

- [65] M.C. Martin et al., *Phys. Rev. B* **56**, 3173 (1997).
- [66] L. P. Regnault et al., *Europhys. Lett.* **32**, 579 (1995).
- [67] K. Hirota et al., *J. Phys. Soc. Jpn.* **67**, 645 (1998).
- [68] B. Grenier, J. P. Renard, P. Veillet, C. Paulsen, R. Calemczuk, G. Dhalenne and A. Revcolevschi, *Phys. Rev. B* **58**, 8202 (1998).
- [69] T. Masuda, A. Fujioka, Y. Uchiyama, I. Tsukada and K. Uchinokura, *Phys. Rev. Lett.* **80**, 4566 (1998).
- [70] H. Nakao et al., *J. Phys. Soc. Jpn.* **68**, 3662 (1999).
- [71] T. Masuda, I. Tsukada, K. Uchinokura, Y.J. Wang, V. Kiryukhin and R.J. Birgeneau, *Phys. Rev. B* **61**, 4103 (2000).
- [72] B. Grenier, J. P. Renard, P. Veillet, C. Paulsen, G. Dhalenne and A. Revcolevschi, *Phys. Rev. B* **57**, 3444 (1998).
- [73] K. Hirota et al., *Phys. Rev. Lett.* **73**, 736 (1994).
- [74] M. Braden et al., *Phys. Rev. B* **54**, 1105 (1996).
- [75] J.C. Bonner and M.E. Fischer, *Phys. Rev.* **135**, A640 (1964).
- [76] L. Bulaevskii, *Sov. Phys. Solid State*, **11**, 921 (1969).
- [77] J. Riera and A. Dobry, *Phys. Rev. B* **51**, 16098 (1995).
- [78] H. Fukuyama, T. Tanimoto and M. Saito, *J. Phys. Soc. Jpn.* **65**, 1182 (1996).
- [79] K.M. Kojima et al., *Phys. Rev. Lett.* **79**, 503 (1997).
- [80] M. Saito and H. Fukuyama, *J. Phys. Soc. Jpn.* **66**, 3259 (1997).
- [81] Professor K. Uchinokura and T. Masuda are gratefully acknowledged for the loan of the doped CuGeO_3 single crystals.
- [82] T. Masuda et al., *Physica B* **284**, 1637 (2000).
- [83] International Tables for Crystallography, ed. A.J.C. Wilson Vol. C, 391 (1992).
- [84] A. Lappas, K. Prassides, A. Amato, R. Feyerherm, F.N. Gygax and A. Schenck, *Z. Phys. B* **96**, 223 (1994).
- [85] P.M. Gehring et al., *J. Phys. Soc. Jpn.* **69**, 592 (2000).
- [86] M. Saito, *J. Phys. Soc. Jpn.* **68**, 2898 (1999).
- [87] F. Semadeni et al., *Phys. Rev. B* **62**, 1083 (2000).

Acknowledgments

My first acknowledgement goes to Prof. Dr. A. Furrer who gave me the possibility to perform this work in his laboratory and who accepted to referee my thesis.

I am grateful to my supervisor Prof. Dr. P. Böni for his scientific advises and support of great quality.

I thank Prof. Dr. G. Kostorz for accepting to co-referee my work.

Special thanks to Dr. B. Roessli who shared his deep knowledge on three-axis spectrometers, and provided an outstanding scientific support for the neutron experiments.

Dr. T. Chatterji, Dr. J. Kohlbrecher and Dr. P. Vorderwisch are gratefully acknowledged for fruitful collaboration in the neutron scattering projects.

The μ SR experiments could be successfully performed with the invaluable help of Dr. A. Amato and C. Baines.

I am grateful Dr. G. Shirane for having started the project on Si-doped CuGeO_3 in collaboration with Prof. K. Uchinokura and T. Masuda.

Dr. H.B. Braun and Dr. A. Bill have helped me to extend my knowledge in the theory of condensed matter.

During these three years I could benefit from the the wide experience of Dr. H. Heer, Dr. M. Koennecke, Dr. D. Maden and Dr. M. Zolliker for the computer science support.

The technical support and advises of P. Décarpentrie, M. Koch, R. Thut, S. Fischer and T. Halter was also of primary importance for the experimental part of the work. I would like to thank my 131 colleagues for many reasons that will be published elsewhere [131].

Many thanks also to all members of LNS who were not mentioned previously.

This work was made possible by the financial support of the ETH-Council, which is gratefully acknowledged.

Curriculum Vitae

Personal:

Name	Fabrizio Semadeni
Nationality	Swiss
Date of birth	October 24th, 1972

Studies:

1997-2000 PhD thesis at the Laboratory for Neutron Scattering, ETHZ & PSI.

1992-1997 Ecole Polytechnique Fédérale de Lausanne (EPFL), Graduate in Physics

1987-1992 Collège de l'Abbaye de St-Maurice (VS), maturité type Latin-Sciences